

Towards reproducible lithium-ion battery cycling using liquid-phase transmission electron microscopy

Présentée le 31 mars 2021

Faculté des sciences et techniques de l'ingénieur
Laboratoire pour la caractérisation in situ des nanomatériaux par des électrons
Programme doctoral en science et génie des matériaux

pour l'obtention du grade de Docteur ès Sciences

par

Jing HOU

Acceptée sur proposition du jury

Prof. D. Damjanovic, président du jury
Prof. V. Tileli, directrice de thèse
Prof. V. Wood, rapporteuse
Prof. W. Chueh, rapporteur
Prof. R. Buonsanti, rapporteuse

Acknowledgements

Through all these years of pursuing my PhD, I have experienced ups and downs, gains and losses, calm and panic, happy and sad moments. Luckily, I always feel supported and accompanied by my colleagues, friends, and family. I would like to thank everyone that shines in this remarkable journey.

First and foremost, I would like to express my deep and sincere gratitude to my supervisor, Professor Vasiliki Tileli, for offering me the opportunity to work in microscopic research on batteries and providing invaluable guidance and trust through all the time. “There are no problems, just solutions.” She always says. Being motivated by her passion and vision, I have learned to keep a strong and open mind in my research and life. Cease to struggle, and you cease to live.

Financial supports from BMW for this project and Zeno Karl Schindler Foundation for the exchange trip are appreciated. Thanks go out to EPFL and TUM for providing insights and expertise that greatly assisted the research. And I wish to express gratitude to time contribution and research suggestions from the Jury for my thesis, Prof. Dragan Damjanovic and Prof. Raffaella Buonsanti.

For all the collaborators that I have worked with. I would like to recognize the exceptional assistance that you all provided during my study—Dr. Marco Cantoni and his CIME crew, from whom I learned almost everything about microscopy. Prof. Dr. Hubert A. Gasteiger and his TEC group at TUM are the most efficient and supportive collaborators.

I would like to pay my special regards to the current and previous group members of INE. A tremendous amount of assistance has been offered by Tzu-Hsien and Robin to accomplish the projects and manuscripts. Valuable discussions with Jan, Nikos, Junjie, and Kavita have always inspired me. It is fortunate to have Reinis, Michele, My, Martina, and Morgan. You make the office a place not only for exchanging scientific opinions but also for sharing culture, cuisine tips, and wines. It is a great pleasure to have all your accompany and support.

To my dear friends, Xiaoxuan&Zhi, Xiaoyu, Huachuan&Chengyue, Suiyang, Xiangwei, Hui, Qianhui, Linlin, JuJu, and Yeli. It is your encouragement and support that help me reach the final goal. This work cannot be done without your input.

Last, my biggest thanks to my family, especially Mom and Dad, for all your love and continuous support through my endless study. Thanks for making everything possible. It is whole-heartedly appreciated that ChuaChua has shared all his precious time and great moments with me. You were my mind healing potion through all the difficult times, and you would always be my light in the darkness. I definitely need to thank my little fluffy body Fuffy. Every chapter I write here is a mark of your company.

Jing Hou

Lausanne, Switzerland, 2021

Résumé

Les véhicules électriques (VE) font l'objet d'une attention grandissante en tant que stratégie importante de réduction des émissions de CO₂ liées au transport. Sur le plan technologique, les batteries lithium-ion (Li-ion) dominent quasi-exclusivement le marché du stockage d'énergie des VE. La cathode de ces batteries est couramment constituée d'oxydes lamellaires riches en nickel, de formule $\text{LiNi}_x\text{Co}_y\text{Mn}_z\text{O}_2$ (NCM), intéressants pour leur haute capacité et bas coût. Leur haute teneur en nickel permet d'atteindre les densités énergétiques élevées que requiert l'industrie automobile pour les longs parcours en contrepartie d'une stabilité réduite impactant en retour la durée de vie des batteries. Il est ainsi crucial de comprendre les mécanismes de dégradation des oxydes NCM riches en nickel afin d'optimiser les performances de ces batteries. Cette thèse vise à développer une méthodologie robuste pour l'étude de systèmes électrochimiques, tels que les oxydes NCM, par microscopie électronique en transmission (MET) en phase liquide, afin de suivre à l'échelle nanométrique leur évolution lors de cycles de charge/décharge.

Cette thèse étudie dans un premier temps le transfert de techniques électrochimiques d'importance pour les batteries Li-ion à une micro-cellule adaptée à l'étude par MET in situ en phase liquide, tels que l'électrodéposition et le cyclage charge/décharge. En particulier, la configuration et la préparation des électrodes, ainsi que les conditions de cyclage, sont optimisés pour obtenir un système représentatif d'une batterie conventionnelle. Cette micro-cellule est ensuite utilisée pour examiner l'évolution de particules primaires NCM par microscopie électronique en transmission à balayage (METB), couplée à une analyse en spectroscopie de rayons X à dispersion d'énergie (EDS), en réponse à un cyclage électrochimique. Une gamme d'oxydes à teneur en nickel variée est étudiée sous différentes conditions de cyclage, révélant des mécanismes de dégradation divers. Ces résultats offrent une perspective sur le contrôle et le choix des paramètres électrochimiques pour l'étude de batteries en microscopie électronique in situ en phase liquide. Par ailleurs, les informations structurelles et chimiques obtenues sur les mécanismes de dégradations des oxydes NCM permettront de guider le développement de

matériaux de pointe pour les cathodes de batteries Li-ion, offrant à la fois une grande capacité et une stabilité accrue.

Mots-clés: les batteries lithium-ion; NCM riches en nickel, microscopie électronique en transmission en phase liquid, cellule électrochimique *in situ*, microscopie électronique en transmission à balayage, spectroscopie de rayons X à dispersion d'énergie.

Abstract

Electric vehicles (EVs) have gained widespread attention in recent years as the dominant strategy for curbing CO₂ emissions through transport electrification. Lithium-ion batteries (LIBs) are currently the most suitable and almost exclusively employed energy storage device for powering EVs. Nickel-rich layered oxides of the general formula LiNi_xCo_yMn_zO₂ (NCM) are widely used as the cathode in LIBs due to their high capacity and low cost. However, the increasing nickel content reduces the stability for the higher energy density that is particularly required for meeting the mileage demand. Hence, understanding the degradation mechanisms of Ni-rich NCM is of great importance for optimizing the performance of battery systems.

This thesis aims to develop methodologies for reproducible and reliable testing of battery systems using transmission electron microscopy (TEM) in the liquid phase in order to probe, at the nanoscale, the evolution of the cathode materials as they respond to the electrochemical charge/discharge cycling.

In detail, this thesis first establishes lithium-ion battery electrochemical processes in a microcell, such as electroplating and charge/discharge analysis. The setup is optimized through the electrode configuration and preparation, while the cycling conditions are adapted for achieving similar electrochemical performance as compared to the conventional bulk cell. With the optimized cell, primary NCM particles are probed using *in situ* electrochemical cells coupled with a scanning transmission electron microscopy-energy-dispersive X-ray spectroscopy (STEM-EDS). The electrochemically induced evolution of NCM that is analyzed using liquid cell TEM uncovers the various degradation mechanisms for the same material under different cycling conditions and for specimens with different Ni content that are cycled under the same conditions. The results offer insights for controlling the electrochemical parameters in the liquid cell for battery studies. Ultimately, the structural and chemical information on the degradation of NCM cathodes can guide our way for designing more advanced NCM cathodes with desirable capacity and enhanced stability simultaneously.

Keywords: lithium-ion battery, Ni-rich NCM cathode, liquid-phase transmission electron microscopy, *in situ* electrochemical cell, scanning transmission electron microscopy, energy-dispersive x-ray spectroscopy.

Table of contents

Acknowledgements	i
Résumé	iii
Abstract	v
Chapter 1: Introduction	1
Chapter 2: Literature review	6
2.1. Principle of operation of lithium-ion batteries	7
2.2. Cathodes in lithium-ion batteries	8
2.3. Degradation mechanisms of cathodes	10
2.4. Methodologies of evaluating the performance and microstructure of cathodes	14
2.5. <i>In situ</i> /operando characterization of cathodes	15
2.6. Liquid cell transmission electron microscopy for battery systems	19
Chapter 3: Methodology	21
3.1. Principles of conventional transmission electron microscopy (TEM)	22
3.2. Electrochemical liquid-phase TEM	25
3.3. Liquid-cell optimization for battery cycling	27
3.3.1. Chip configuration	28
3.3.2. Site-specific deposition of battery electrodes	30
3.3.3. Electrochemical configuration for battery study in liquid cell	32
3.4. Identical location studies	34
3.5. Analytical electron microscopy	35
3.5.1. Radiation impact	35
3.5.2. Errors in the EDS chemical mapping	35
Chapter 4: Li-Au alloy as micro-reference electrode	38
4.1. Introduction	39
4.2. Experimental	40
4.2.1. Electrochemical micro-chips for <i>in situ</i> TEM measurements	40
4.2.2. Site-specific deposition of LiFePO ₄ (LFP) particles	41
4.2.3. Reference electrode preparation in open-cell configuration.	41
4.2.4. Chemical stability assessment after lithiation	42
4.2.5. Reference electrode assessment in liquid-cell	43
4.2.6. Electron microscopy	43
4.3. Results and Discussion	44
4.3.1. Benchtop galvanostatic lithiation of gold reference electrode from various sources....	44
4.3.2. Benchtop evaluation of lithiated gold stability	47
4.3.3. Characterization of lithiated electrode	48

4.3.4.	Galvanostatic lithiation of gold reference electrode in liquid cell	49
4.3.5.	Electrochemical evaluation of lithiated gold as reference in liquid cell	51
4.3.6.	Chemical stability of the system	52
4.4.	Conclusion	53
Chapter 5:	Cycling of NCM622 in the micro-battery system.....	54
5.1.	Introduction.....	55
5.2.	Methods.....	55
5.2.1.	Particle size modification of NCM622	55
5.2.2.	Chip optimization for the chip-based micro-battery system	56
5.2.3.	Electrode preparation	57
5.2.4.	Micro-battery assembly within liquid cell	58
5.2.5.	Electrochemical measurements	58
5.2.6.	Post mortem electron microscopy	60
5.3.	Results and discussion	60
5.3.1.	Bulk electrochemical response of ball-milled primary particles.....	60
5.3.2.	Electrochemical response of ball-milled primary particles on the electrochemical chip 63	
5.3.3.	Cycling of ball-milled particles with varying electrochemical input in a liquid microcell TEM holder and post mortem TEM analysis	64
5.4.	Conclusion	67
Chapter 6:	Electrochemical and structural evolution of NCM622 and NCM811 in micro-batteries 68	
6.1.	Introduction.....	69
6.2.	Methods.....	70
6.2.1.	Material processing and electrode preparation	70
6.2.2.	Battery assembly	70
6.2.3.	Electrochemical measurements	71
6.2.4.	Post mortem electron microscopy	72
6.3.	Results and discussion	72
6.3.1.	Electrochemical measurements of the two Ni-rich cathodes on coin and micro open cell configurations	72
6.3.2.	Chemical evolution of particles cycled in the liquid cell	75
6.4.	Conclusion	79
Chapter 7:	Conclusions and perspectives	80
Bibliography	83
Curriculum vitae	104

Chapter 1: Introduction

Vehicle electrification has attracted enormous attention in recent years as it is the main decarbonization pathway for road-based transportation. The expectation is that by 2028 up to 200 million electric vehicles (EVs) will be on the road[1], [2]. Therefore, the corresponding requirements on the batteries used as the power suppliers in automotive applications are becoming stricter. Improving the battery performance consists of enhancing the energy density (Wh/l) and specific energy (Wh/kg) as well as their safety, cost, and charging speed.

Lithium-ion batteries (LIBs) possess great energy and power performance compared to other battery technologies[3]. Since being commercialized in the 1990s, the specific energy of LIBs has improved from approximately 90 Wh/kg to over 250 Wh/kg, which allows automobiles to drive satisfactory distances under typical driving patterns. Meanwhile, the dropping cost of battery packs at 250 USD/kWh, with the room of falling to 70 USD/kWh by 2030 or 2040, is pushing EV beyond niche applications while enlarging their acceptance and market share[4], [5]. The next decade's battery demand is estimated to be more than 10 times the existing condition[6].

However, a gap remains in the recent LIBs performance to the electric vehicles market's future requirements, according to the expectation summarized by the European Council for Automotive R & D (EUCAR), as presented in Table 1-1. The specific energy and energy density of batteries is expected to be at least double its current value. Faster charging is also requested for optimizing the refueling time without sacrificing their service life. One of the main obstacles is the energy density of the cell and the stability during service. In order to reach the given target value, adjustments on electrode materials, electrolyte, and their interfaces need to be made. Thus, understanding, controlling, and designing the function of electrodes, electrolyte, and their interfaces are the key to developing ultra-performing, smart, and sustainable batteries. One of the current trends on improving lithium-ion batteries is combining Ni-rich layered oxide cathodes with less flammable electrolytes and perhaps upgraded anodes[7].

Table 1-1: Battery requirements for future Battery Electric Vehicle (BEV) applications [8].

BEV parameters	Unit	Condition	State of the art-2019	Target 2030 Range >600km
Specific energy	Wh/kg	@ 1/3C charge and discharge at 25°C	~250	450
Energy density	Wh/l	@ 1/3C charge and discharge at 25°C	~500	1000
Specific power-discharge	W/kg	180s, SOC* 100%-10%, 25°C	750	1000
Power density-discharge	W/l	180s, SOC 100%-10%, 25°C	1500	2200
Charging rate	C (1/h)	SOC 0%-80%	3	3.5
Cost	€ / kWh		220	70
Lifetime	Years & km	DOD** 90%	Lifetime of a car 150.000 km	Lifetime of a car 150.000 km

* SOC: State of charge

**DOD: Depth of discharge

Fundamental studies of the degradation processes in LIBs, induced by the electrochemical stimuli, are mainly carried out by static and post-mortem methods. For example, concerning the degradation mechanisms of cathodes, many *ex situ* studies make use of electrode materials harvested from coin cells that have been cycled for days to months or even years[9], [10]. Despite the insights provided from such data, the real-time dynamic evolution during battery operation by techniques capable of resolving the structural and compositional modification corresponding to the electrochemical stimuli could provide unprecedented insights that could further help design and develop high performing LIBs[11]. Liquid-phase transmission electron microscopy (TEM) is a promising technique for such purposes. However, its implementation has certain challenges. For example, the electrochemical microcell/system has to be miniaturized in such a way that the electrochemistry can be reproduced and that it matches the conditions found in the bulk case. Therefore, in this PhD thesis, I attempt to develop a reliable and comprehensive micro-battery setup for liquid-phase TEM and we apply it to the understanding of the degradation mechanisms of Ni-rich layered oxides cathodes.

Specifically, **Chapter 2** provides a literature review where the basic working mechanism of lithium-ion batteries and the functionality of each component is introduced. The development of cathode materials from the structural and compositional aspects and the fundamental considerations regarding their degradation are discussed. Conventional electrochemical and microscopic techniques for electrode material analysis are reviewed. The different *in situ* characterization methods for studying cathodes are presented, especially in the liquid phase.

Chapter 3 is dedicated to establishing a background on the experimental instruments and the techniques used in the thesis. The electrochemical cell explicitly designed for the TEM study of samples in a liquid environment is described. System optimization through improving chip configuration, functionalization, and electrochemical connections is elucidated for obtaining the most comparable results with the corresponding ones at the micro-scale. The various electron microscopy imaging modes are also discussed.

Chapter 4 introduces procedures and reliable options for establishing a reproducible method for stabilizing the reference electrode in the liquid cell. The alloyed electrode holds a stable potential over the electrochemical measurements of the working electrode without self-damaging or disturbing the micro-battery cycling.

Chapter 5 demonstrates the progress towards electrode material loading on the electrochemical chip and cycling as a micro battery system. The reliability of the electrochemical performance of the system is evaluated. Cathode material evolution with respect to structural and compositional changes corresponding to the stimuli from *in situ* electrochemical cycling is investigated by post-mortem electron microscopy.

Chapter 6 presents elemental maps of the evolution of Ni-rich layered oxide cathodes within the electrochemical cell under accelerated cycling conditions. Various degradation mechanisms for cathodes with different compositional content under the same cycling conditions are reported. The

degradation was found to be caused either by intraparticle phase transformation or ionic isolation caused by interface reaction between the electrode and electrolyte.

Chapter 7 summarizes the advancements in designing a reproducible micro battery system in the liquid cell for TEM studies and concludes on the degradation mechanisms that have been discovered based on electrode material and cycling conditions. Additionally, future prospects of degradation studies of cathodes as well as their potential cycling within the electrochemical cell setup for liquid-phase TEM are suggested.

Chapter 2: Literature review

2.1. Principle of operation of lithium-ion batteries

A typical lithium-ion battery (LIB) is an electrochemical cell that consists of a positive (cathode) and a negative (anode) electrode that are separated by a solid separator and are immersed in a liquid electrolyte. The cathode composite consists of active materials as well as binder and conductive additives for improving the adhesion to the current collector and the interconnection between adjacent active particles[12], [13]. The conductive additives are typically carbon-based networks used to enhance electron transport in the electrode and, therefore, improve the electrode's conductivity[14]. An intercalation cathode behaves as a host network, which should be able to release Li-ions during the charging process and dope Li-ions during the discharging. As illustrated in Figure 2-1, during charging, lithium ions are deintercalated from the cathode and shuffle in the electrolyte through the separator towards the anode. At the same time, electrons generated by oxidization in the cathode pass through the external circuit in the same direction, performing the external work. Discharging reverses the direction, and the ions flow from the anode to the cathode. Consequently, developments to improve the overall performance include novel stable cathode materials[15]–[17], durable anode materials[18]–[21], new electrolytes[22], [23], and electrolyte additives that suppress side reactions between the electrode materials and the electrolytes[24]. Herein, the focus is placed on the cathode material and its degradation mechanisms during electrochemical cycling.

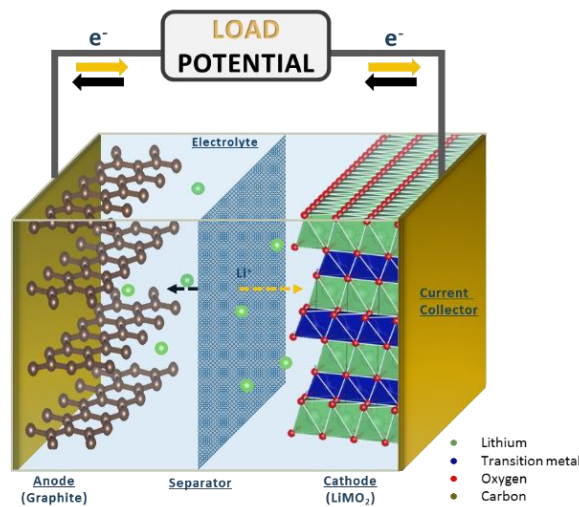


Figure 2-1: Schematic drawing of a lithium-ion battery.

2.2. Cathodes in lithium-ion batteries

Layered transition metal oxides are the most used cathodes in commercial Li-ion batteries. The success of this family of oxides for LIBs is due to their layered structure, which is isostructural to the α -NaFeO₂ structure belonging to $R\bar{3}m$ space group. More specifically, in this crystal structure, transition metal (TM) ions and lithium ions are located in octahedral sites and occupy alternating layers in a cubic close-packed array of oxygen ions[25], [26]. The unit cell of LiCoO₂ (LCO), for example, is formed by three slabs of edge-sharing CoO₆ octahedra separated by interstitial layers of Li-ions (Fig. 2-2a)[27]. The individual Li-ions and CoO₆ octahedra stacks provide a two-dimensional structure that facilitates high Li-ion mobility. Even though the LiCoO₂ can generate a theoretical specific capacity of 272 mAh/g at a potential of 4.2 V vs. Li/Li⁺, the reversible ability is limited to 140 mAh/g, with only 88% retention after 50 cycles. This poor resistant performance is reported to result from delithiation induced by bulk structure degradation (i.e., extracting more than 50% Li during charging transforms the structure from hexagonal to monoclinic) and the harmful side reaction on the surface[28]. The spinel oxides (Fig. 2-2b) with the chemical formula LiM₂O₄ is another category of LIBs[29]. It was proposed in the early 1980s aiming at cheaper and safer batteries. However, these spinel oxides have a low practical capacity (<150 mAh/g) that, upon cycling, it fades severely. Additionally, the high potential that is provided by Ni²⁺/Ni⁴⁺ redox couple facilitates the decomposition of the electrolyte, forming the solid electrolyte interface (SEI) on the cathode surface. Another much-studied cathode is the olivine phosphate oxide LiFePO₄ (LFP) (Fig. 2-2c), which is treated as a strong competitor to the layered oxide family owing to its low cost, low toxicity, high charge and discharge rate, low capacity fade, and increased safety[30]. For applications that require high-power operation and safety under over-charge conditions, LFP is the best candidate. However, its flat discharge plateau at 3.4 V and its low capacity of 170 mAh/g make LiFePO₄ insufficient for supporting electric vehicle operation[3].

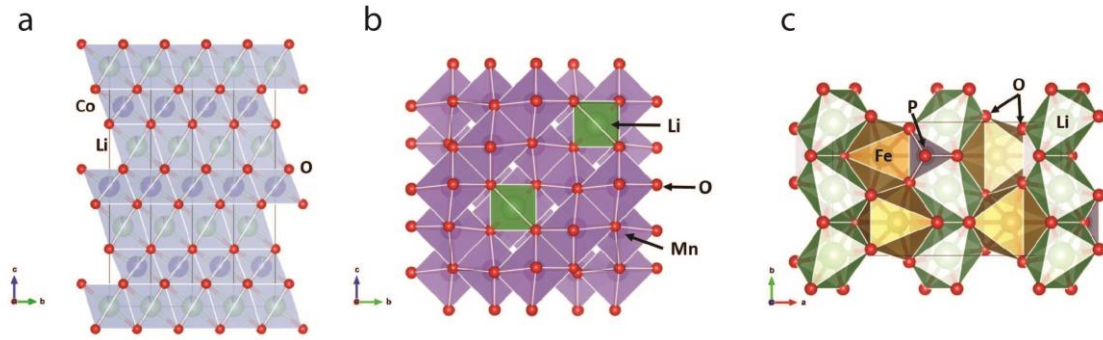


Figure 2-2: Crystal structures of three types of cathode materials. (a) layered structure, (b) spinel structure, and (c) olivine structure.

Specifically for the layered oxide cathodes, approaches for improving the stability of the LiCoO_2 have led to the implementation of alternative transition metals. Firstly, the more cost-efficient Li_xNiO_2 was investigated. However, it is not favorable as a proper cathode due to the tendency of Ni^{2+} (0.69 \AA) ions to migrate into the Li^+ (0.76 \AA) sites, blocking the diffusion path of Li during cycling and its weaker thermal stability as Ni^{3+} is more readily reduced than Co^{3+} [31], [32]. Therefore, rather than using single TM ions (LiCoO_2 or LiNiO_2), Ohzuku *et al.* in 2001 proposed binary ($\text{LiCo}_{1/2}\text{Ni}_{1/2}\text{O}_2$) and ternary ($\text{LiCo}_{1/3}\text{Ni}_{1/3}\text{Mn}_{1/3}\text{O}_2$) systems, containing more TM ions for optimizing stability and capacity [15]. A potential of 3 V - 4 V vs. Li/Li^+ can be generated from balancing the Li^+ charge through the redox reactions of transition metals. This assists in maximizing the energy density under the constraint of the stable electrolyte window[33]. More specifically, as summarized in Figure 2-3a, Mn has been introduced for stabilizing the structure, especially at a highly delithiated state, even at high temperatures. Ni has been added for improving the capacity since the $\text{Ni}^{2+}/\text{Ni}^{4+}$ redox couple has higher standard potential (1.59 V) than that of $\text{Co}^{2+}/\text{Co}^{3+}$ (1.42 V) and $\text{Mn}^{4+}/\text{Mn}^{3+}$ (0.95 V). In addition, the potential Li/Ni disorder can be mitigated by a reduction of the Co content from 8% to 4%[34]–[37]. As a result, Ni-rich layered transition metal oxide cathodes tend to be the most promising candidates for high capacity density LIBs for EVs. However, as presented in Figure 2-3b, it is generally understood that increasing the Ni content increases the energy density but incurs severe capacity fading during cycling[38]. The electrochemical performance degradation is due to the declining of the capacity and

working voltage, while safety issues arise from thermal runaway under harsh cycling conditions, including overcharging, overheating, and electric shorting. Therefore, the balance between the intrinsic capacity and voltage of the cathode is the main target that can lead to significant progress on the energy density. As presented in Figure 2-3c, $\text{Li}(\text{Ni}_{0.6}\text{Co}_{0.2}\text{Mn}_{0.2})\text{O}_2$ (NCM622) has been found to have the best combination of relatively high specific energy of 180 mAh/g and good tolerance to the high voltage cycling and thermal abuse condition [39]–[41]. However, under highly demanding cell configuration and operating conditions, NCM811 with higher area capacity/charge voltage (4.8 mAh/cm²/4.6 V) tends to be the promising choice serving as cathode for lithium-ion batteries with higher energy density[36].

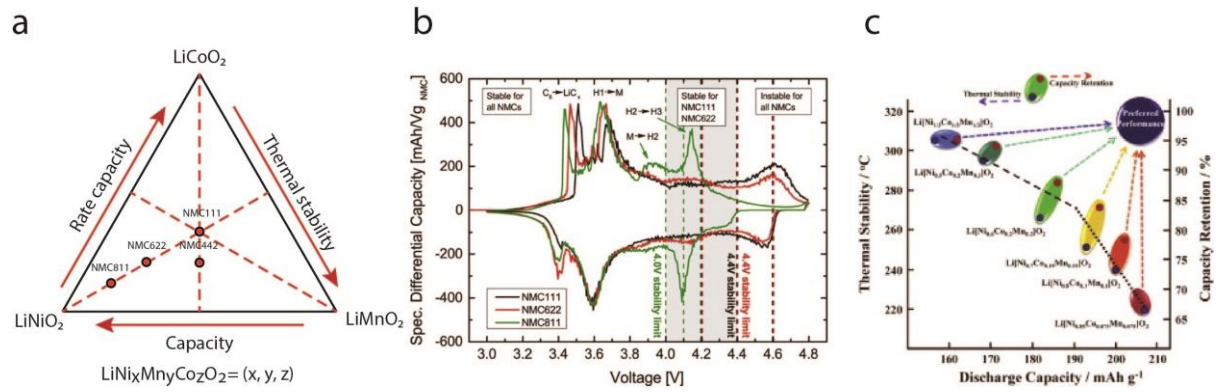


Figure 2-3: (a) Ternary diagram of transition metal ions contained in Li-ion batteries specified by their performance. (b) Profile of differential capacity vs. the potential for NCM with various Ni content. Reproduced with permission from [38]. (c) Schematic correlation of performance and safety with Ni content. Reproduced with permission from [39]. © 2013 Elsevier BV.

2.3. Degradation mechanisms of cathodes

Unfortunately, the capacity loss that comes with raising the intrinsic capacity by increasing the Ni content in NCM cathodes remains the main challenge for obtaining the favorable energy density requested by EVs applications. The capacity loss of the battery consists of two parts: reversible loss and irreversible loss. The disruption of the system equilibrium causes the reversible capacity loss due to the high current density charge/discharge condition that brings incompatible ionic motion within electrodes and across the electrolyte/electrode interface with the ionic current density on the system. In contrast,

irreversible capacity loss can be caused by component degradation and irreversible parasitic reactions. Understanding the degradation mechanisms of Ni-rich NCM cathodes is crucial for making a step forward for high capacity and high voltage LIBs for EVs. The origins of performance degradation were reported to include Ni/Li cation disorder[42]–[46], microcrack generation within particles[47]–[49], oxygen evolution[38], [50], irreversible phase transition[51]–[55], and transition metal dissolution[56], [57], as summarized in Figure 2-4. Particularly, the thermally induced phase transition of NCM particles from layered (MO_2) to spinel (M_3O_4) and rocksalt (MO) structures is accompanied by oxygen release. The released oxygen can, in reverse, lead to thermal runaway of the battery, especially at the overcharge state, when both the Ni and O redox couples contribute to the capacity[38], [52], [58], [59]. The higher the Ni content, the easier the degradation through various pathways, and this leads to a decrease of the upper cut-off potential for stable cycling of NCM cathodes[38]. Creating a controllable cathode-electrolyte interface has been proposed for preventing degradation [60]. For example, coatings can either change the surface chemistry or provide physical protection passivation films on the surface of the particles[61]. In addition, a progressive concentration gradient with decreasing Ni content from core to shell has been proposed[62].

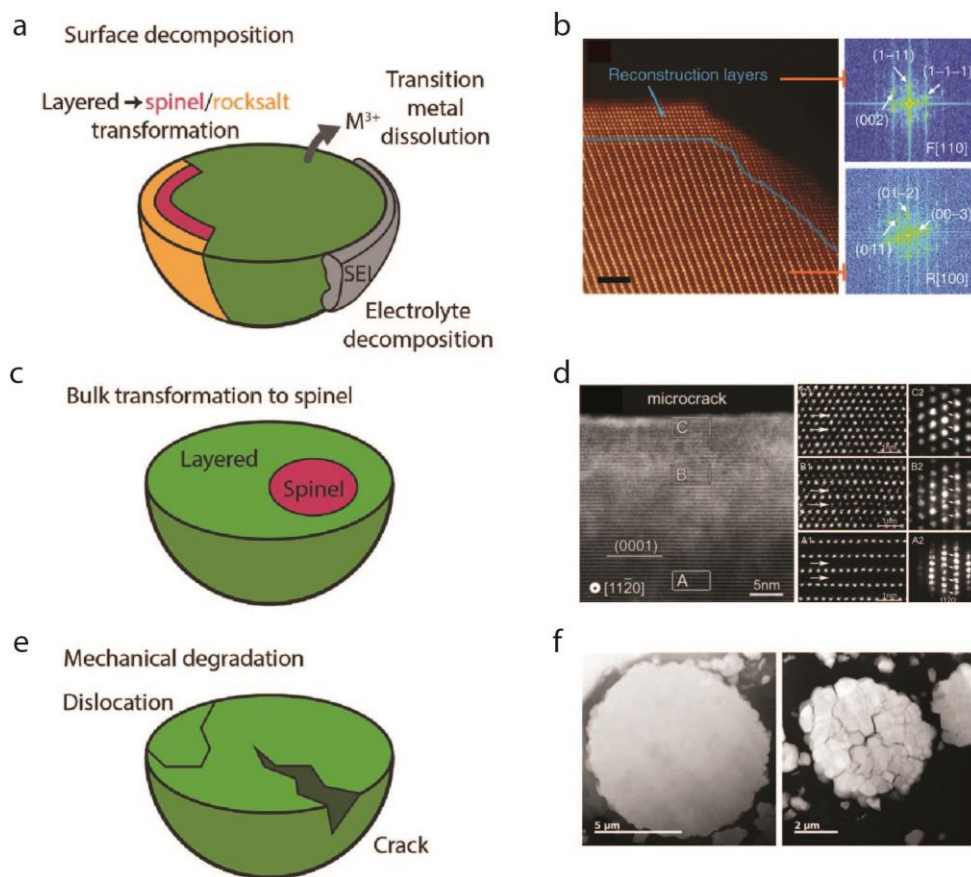


Figure 2-4: Degradation mechanisms in layered lithium oxides. (a) Schematic of degradation through surface decomposition and reconstruction. (b) NCM layered structure reconstruction from the surface and FFT results of the surface reconstruction layer ($Fm\bar{3}m[110]$ zone axis) and the NCM bulky layered structure ($R\bar{3}m[100]$ zone axis). Adapted from [52]. © 2014, Nature Publishing Group, a division of Macmillan Publishers Limited. (c) Schematic of degradation by bulk transformation into spinel. (d) STEM image of the grain boundary of the microcracks formed on a single cycled NCA particle. High-magnification STEM images (A1, B1, and C1) and diffraction patterns (A2, B2, and C2) illustrate the transformation from layered to rocksalt near the microcrack and correspond to the regions marked A, B, and C in the left panel. Adapted with permission from [63]. © 2011 The Electrochemical Society (e) Schematic degradation by microcrack formation. (f) Cross-sectional STEM images for NCM811 before (left) and after (right) 600 cycles. Reproduced with permission from [49]. Schematics are adapted from [64]. © 2017 WILEY-VCH Verlag GmbH & Co. KGaA, Weinheim.

The achievable discharge potential of the cell also constrains the battery energy density. Herein, the constant chemical potential difference between the anode (μ_A) and the cathode (μ_C) and the limited electrochemical window of the electrolyte are the main restrictions for the development of high voltage cathodes[65]. As illustrated in Figure 2-5, the electrochemical window of the electrolyte is determined by the energy gap from the highest occupied molecular orbital (HOMO) to the lowest unoccupied molecular orbital (LUMO). Ideally, the chemical energy of the electrode should be within the range set

by the electrolyte. Otherwise, the electrolyte will be reduced on the anode or oxidized on the cathode, forming a passivating solid electrolyte interface (SEI), which is called cathode electrolyte interface (CEI) specifically on the cathode[66]. On the one hand, the SEI film can reduce the overpotential and polarization on the electrode by facilitating the diffusion of Li-ions through the uniform electric field. While on the other hand, it may increase the internal resistance of the battery and consume the Li-ions from the cathode, leading to capacity loss[67]. Thus, the physically strong and flexible SEI layer should form under fast kinetics before the onset of intercalation reactions[68]. SEI stabilization has been addressed either by creating an artificial interphase coating to reduce the lithium trapping or introducing additives to the electrolyte [69], [70].

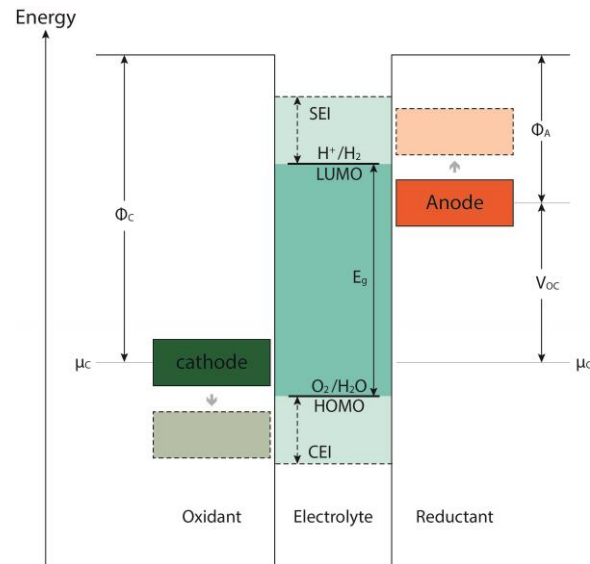


Figure 2-5: Schematic of the energy levels involved in a Li-ion electrochemical cell. The dashed orange and green rectangles correspond to the chemical potential of Li in the negative electrode and positive electrode, and the blue line gives the voltage window of the electrolyte.

Thereupon, the understanding of the chemical and structural evolution of electrode materials and the formation mechanism of the interphase between electrode and electrolyte under normal cycling conditions are of great importance to better understand the limitations of the current lithium-ion batteries. However, evaluating the complex path of cathode degradation in real-time remains challenging due to their sensitivity towards moisture and oxygen environments. Moreover,

electrochemical control over the potential dependent reactions on the specimens is agreed to be critical in order to prevent alterations of the measured electrochemical signal.

2.4. Methodologies of evaluating the performance and microstructure of cathodes

Several diagnostic tools for elucidating degradation mechanisms of cathodes in LIBs during operation have been applied[71]. Generally, the conventional electrochemical evaluation serves as an assessment of the battery working conditions. Instantaneous information is given as the state of charge (SOC), quantifying the usable energy at the present cycle, and state of health (SOH), indicating the remaining performance of the battery. These two parameters are often estimated using the open-circuit voltage (OCV)[72]. The dynamic performance of a battery in charge/discharge and the subsequent capacity decay can only be distinguished by measurements of voltage under constant charge/discharge current inputs, which is also called the galvanostatic charge/discharge test[72]. As aging is commonly evaluated in terms of not only capacity fade but also impedance rise under different conditions, electrochemical impedance spectroscopy (EIS) is used for evaluating the transport and electrochemical process involved during LIB cycling[73], [74]. The evolution of resistances, capacitances, and characteristic frequencies of the various effects can be tracked and the charge transfer effects within the electrode and across the interphase layer can be identified[75], [76]. The impedance of a cell is influenced by the contribution of both positive and negative electrodes, and its values at different SOC levels can be monitored from the half-cell system. Precise analysis of the evolution of electrodes can be obtained by separate measurements on positive and negative electrodes. The charge transfer at the positive electrodes and Li^+ transport across the SEI layer with increasing thickness is presumed as the reason for performance decay during cycling[76], [77].

In addition to the electrochemical analysis, the microstructural analysis can provide fundamental insights into the degradation mechanism of electrode materials. For example, the structural rearrangement has been discovered by crystallographic analysis of cycled cathodes at different lithiation

states in the same voltage range using X-ray diffraction (XRD)[78]. The combination of XRD with light microscopy and cross-section scanning electron microscopy (SEM) has helped to link the disintegration of secondary particles caused by an intergranular fracture with the mechanical stress at the interfaces between the primary crystallites[79]. The generation of such mechanical stress has been attributed to the Ni-Li anti-site defects and mismatch of grains with disparate crystal phases[80], [81]. Surface reconstruction by the phase transition from $R\bar{3}m$ to $Fm\bar{3}m$ and the formation of the surface reaction layer (SRL) that is identified as a complex amorphous organic matrix have been explored by X-ray absorption spectroscopy (XAS) coupled with atomic-scale scanning transmission electron microscope (STEM) and electron energy loss spectroscopy (EELS)[52]. Furthermore, the difficulty of phase mapping relevant to the Li distribution within cathode materials has been overcome by taking advantage of the improved sensitivity of low-loss signals from energy-filtered (EF)TEM[82], [83]. The oxidation state evolution of the transition metal ions can be obtained by electron paramagnetic resonance (EPR)[84], and quantitative species identification can be achieved through nuclear magnetic resonance (NMR) spectroscopy[85].

2.5. *In situ*/operando characterization of cathodes

Over the years, more and more sophisticated diagnostic tools have been developed that can be operated *in situ* and in operando during battery cycling[51], [86], [87]. Adjusting the cycling conditions of electrodes and monitoring the reactions are indispensable in sustaining the determining parameters for maximizing their potential performance and ensuring safe operation. A combination of diverse *in situ* electrochemical analysis can be used to observe detrimental phenomena, including charge transfer resistance increase, irreversibility of electrode phase transitions, and the SEI formations under different upper cut-off voltages[88].

As illustrated in Figure 2-6a, various *in situ* techniques covering multiple length scales from cells to electrodes and particles to interfaces and lattices have contributed to obtaining essential knowledge of

structure, morphology, composition, and state of metals in the electrodes (Fig. 2-6b). *In situ* neutron characterization provides a platform for tracking the material evolution while cycling at a bulk scale with a spatial resolution of millimeters. Neutron's high penetration power and relatively high sensitivity to Li isotopes enable the detection of electrode material under conditions for slow reaction kinetics or with a repeated data accumulation process. These measurements are representative of the bulk rather than from the surface region[89]–[91]. Distinctive pathways for lithiation and delithiation have been reported by Wang et al. using *in situ* neutron diffraction on a large format pouch battery cell[92]. As a commercial cathode material, the structural evolution of LiFePO_4 (LFP) has also been investigated in real-time with the aid of the *in situ* neutron powder-diffraction (NPD) by Sharma et al.[93], while the role of the kinetic transformation pathway was underscored by Malik et al.[93]. Taminato has discovered the inhomogeneous lithium distribution through the diffraction profiles of the electrode during discharging taken from *in situ* neutron diffraction, Figure. 2-6c[94].

In addition to quantifying the entire electrode, tracking ionic/electronic transport in single-crystalline particles by synchrotron X-ray methodologies has provided an assessment of battery materials at a more fundamental level. With this technique, the ultrafine variation caused by Li-ions in and out of the electrode materials during the charge/discharge cycle process has been evaluated[95]. Zhang et al. have employed microbeam XRD for direct observation on the phase evolution of LiFePO_4 nanoparticles during cycling[96]. Lim et al. have used operando synchrotron-based liquid phase scanning transmission x-ray microscopy (STXM) to reveal the coupling of lithium composition and surface reaction rates for the control of the kinetics and uniformity during electrochemical ion insertion in LiFePO_4 particles[97]. *In situ* time-resolved XRD and mass spectroscopy (TR-XRD/MS) has elucidated the oxidation state change of TM cations (i.e., Ni, Co, and Mn) and the subsequent migration that causes thermal decomposition of NCM cathodes[51]. The results suggested that the origin of the fading phenomenon is a bulk issue rather than only a surface degradation. Other techniques such as Raman spectroscopy, Fourier-transform infrared (FTIR) spectroscopy, X-ray absorption spectroscopy (XAS) have also been applied to probe the surface and interfacial evolution of electrodes[98]. It is noted that

one can benefit from more considerable penetration power, shorter measurement times, and better signal-to-noise ratios during *in situ*/operando studies from synchrotron-based X-ray spectroscopy[99]. For example, the Difference Fourier map presented in Figure 2-6d has revealed an irreversible transition-metal motion within the host structure after cycling by using long duration *in situ* synchrotron X-ray powder diffraction measurements[100].

Real-time observation of the SEI evolution has also been possible using electrochemical atomic force microscopy (EC-AFM). This technique is particularly useful for revealing the chemical and morphological differences of complex SEI formation from the various electrolytes and cycling rates. The observations revealed that the SEI is composed of two layers, a hard coating on the surface of the electrode and a loosely packed precipitate on top. The density of the top layer varies with the electrolyte, and the total thickness of SEI is inversely proportional to the scanning rate in cyclic voltammetry[87].

Finally, the observation of microscopic mechanisms in electrode materials and at their interfaces can be achieved by *in situ* electron microscopy[101]. Dendrite formation during lithium plating/stripping in ether-based electrolytes has been investigated by liquid electrochemical scanning electron microscopy (EC)-SEM. The results revealed that the energetically favorable sites for lithium atoms could prevent the accelerated dendrite formation, eventually leading to safer operation of batteries[102]. Requests for ultrahigh spatial resolution (nano- to atomic-scale) can be achieved only by using the higher-energy electron beam that can transmit through the thin sample. TEM, therefore, stands out for high spatial/temporal resolution, superior sensitivity to inhomogeneity, and versatile capabilities. TEM experiments are usually limited to batteries with solid electrolytes or nonvolatile liquid electrolytes in open-cell TEM, which are not conventionally used in commercial cells. Nevertheless, real-time atomic-scale imaging and simultaneous composition analysis can bring many valuable insights into the (de)lithiation mechanisms[103]–[105]. As presented in Figure 2-6e, the *in situ* environmental transmission electron microscopy (ETEM) has been used for revealing the reversible phase transition and understanding the lithiation mechanism in nanowires as a cathode [106].

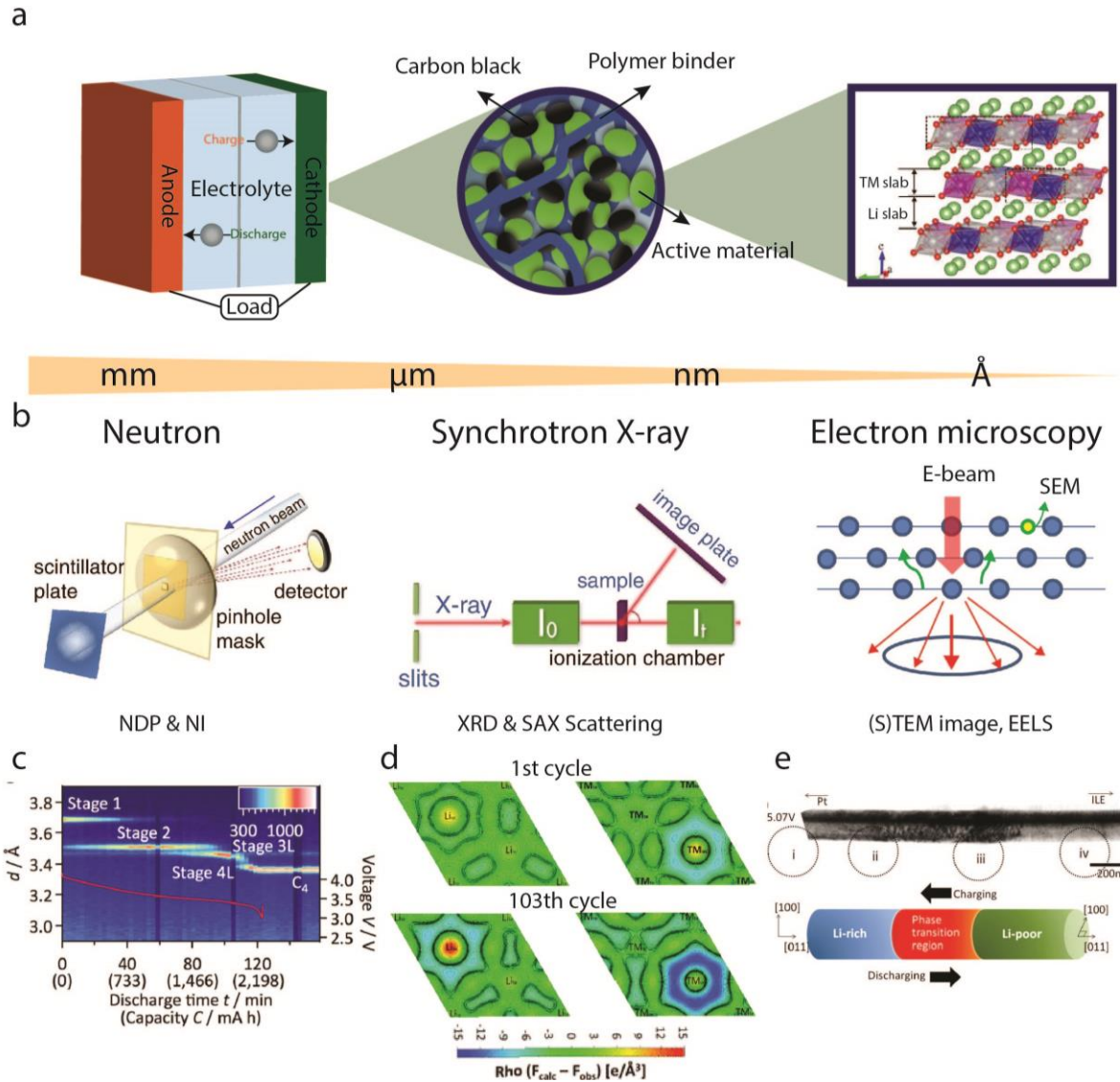


Figure 2-6: (a) Illustration of battery components at different scales. From left to right, layered stacks of cathode and anode separated by electrolyte, with a thickness of up to 100s μm ; composite electrode with the active material, carbon black, and a polymer binder, with particle sizes of 10s nm to microns; lattice structures of active material with the characteristic length of Angstroms. (b) Corresponding in operando measurement techniques for probing structures at different length scales, as exemplified (from left to right) by neutron activation and absorption imaging, x-ray scattering, and electron microscopy and spectroscopy. Reproduced with permission from [107]. © 2016 Elsevier Ltd. (c) Diffraction profiles taken from *in situ* neutron diffraction shows the graphite phase changes during cycling with NCM at 1C. Adapted with permission from [94]. © 2016, The Author(s). (d) Difference Fourier maps of the Li and TM plans of discharged HE-NCM taken with synchrotron XRD, a and b = 2.8791(1) \AA , c = 14.378(2) \AA after the first cycle and after 103 cycles, a and b = 2.8801(1) \AA , c = 14.375(2) \AA Adapted with permission from [100]. © 2018 American Chemical Society. (e) Reversible movement of a phase transition region (red) between Li-rich and Li-poor phases during the cycling of a single LiMn_2O_4 nanowire-based battery was captured. Adapted with permission from [106] © 2014 American Chemical.

2.6. Liquid cell transmission electron microscopy for battery systems

The electrical biasing technique combined with *in situ* TEM in liquids was first demonstrated by Frances Ross and coworkers in 2003[108]. Liquid cell TEM has been used to examine either electrode evolution (Fig. 2-7a&b) or the modification of the interface (Fig. 2-7c) during electrochemical cycling. Inhomogeneous (de)lithiation among LiFePO_4 particles in an electrochemical liquid cell (Figure 2-7a) was revealed by time-sequential energy-filtered TEM (EFTEM) within a full battery cell. The operando nanoscale imaging of electrochemically active ions in the electrode and electrolyte has aided in gaining information on various delithiation mechanisms simultaneously for different particles under the same conditions[109]. Precession electron diffraction with *in situ* electron diffraction tomography (EDT) experiments enabled the quantitative kinematical approximation for the structural changes occurring in cathode materials upon charging[110]. Variations in the unit cell parameters and changes in the occupancy of the Li positions and interatomic distances were attained from such *in situ* transmission electron microscopy experiments in the liquid environment (Fig. 2-7b). Additionally, Lutz et al. have reported on the mechanism of NaO_2 nucleation/growth, in real-time, during discharge and charge of Na– O_2 micro battery using a liquid aprotic electrolyte coupled with fast imaging[111]. The interfacial film formation on the surface of the electrode as a result of interacting with electrolyte has been monitored by *in situ* TEM within an electrochemical liquid cell. Direct observation of inhomogeneous lithiation, lithium dendrite growth, and interface formation have been reported by Zeng et al., as presented in Figure 2-7c [112]. Furthermore, microstructural changes and the induced stress have been monitored using *in situ* BF STEM for studying nanoscale phase evolution in cathodes[113]. Finally, the potential induced breakdown of electrolyte accompanied by the SEI formation on the surface of the electrode material has been observed by Unocic and coworkers[114].

As evidenced, most of the liquid phase TEM studies on cathodes have been carried out on LiFePO_4 due to the size restriction of the liquid chamber in the electrochemical cell. However, for the practical application of cathode materials in electric vehicles, NCM holds a more promising prospect. Therefore, this thesis focuses on investigating the more promising and challenging NCM cathodes and monitoring

their evolution during battery cycling using liquid-phase transmission electron microscopy techniques. Since more complex methods and system setup are requested for examining NCM particles in a liquid microcell, the following chapter introduces in detail the liquid phase TEM operating principles using electrochemical microcells

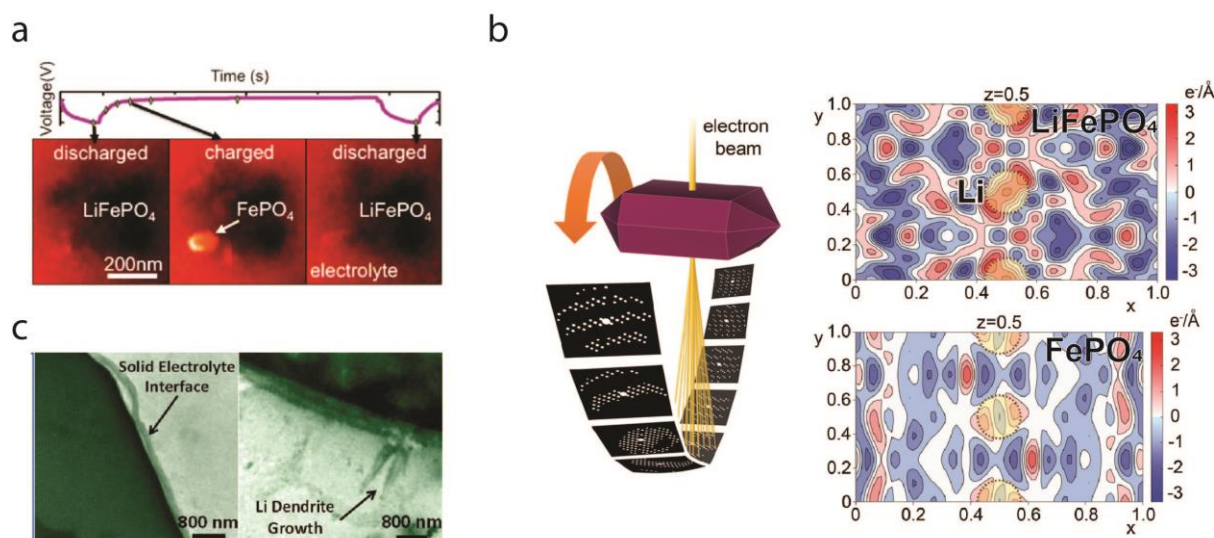


Figure 2-7: *In situ* liquid cell TEM for studying LIBs. (a) Cathode phase transformation investigation by imaging the nanoscale distribution of ions during cycling using EFTEM in a liquid flow cell. Reproduced with permission from [109]. © 2014, American Chemical Society. (b) Tracking the crystal structural modification at the unit cell scale using difference Fourier maps of scattering density for LiFePO₄ and FePO₄ from electron diffraction tomography. Adapted with permission from [110]. © 2018 American Chemical Society. (c) Direct visualization of the growth and dissolution of Li–Au alloy and lithium metal dendritic growth using liquid cell TEM. Adapted with permission from [112]. © 2014 American Chemical Society.

Chapter 3: Methodology

3.1. Principles of conventional transmission electron microscopy (TEM)

Typically, TEM is operated under a high vacuum to avoid scattering of the electron beam. As illustrated in Figure 3-1, the emission from the electron source requires a vacuum environment of 10^{-7} to 10^{-10} mbar, while the column and the area of the specimen are evacuated steadily to a vacuum of 10^{-5} to 10^{-7} mbar. As such, specimens that can be loaded for characterization in TEM are limited to dry materials that do not outgas significantly.

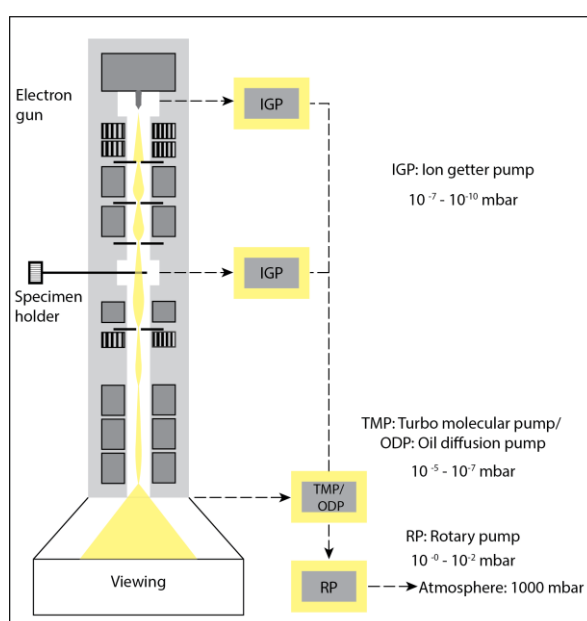


Figure 3-1: Schematic of a vacuum system for a TEM.

In TEM, a primary electron beam is accelerated at high voltage (typically between 60-300 kV). When the electron beam shines on the electron transparent specimen, electrons can pass through the specimen without interacting (transmitted beam) or can scatter by interacting with the atoms in the sample (Fig. 3-2). Thus, various information about the sample can be obtained depending on the signal that is used for imaging.

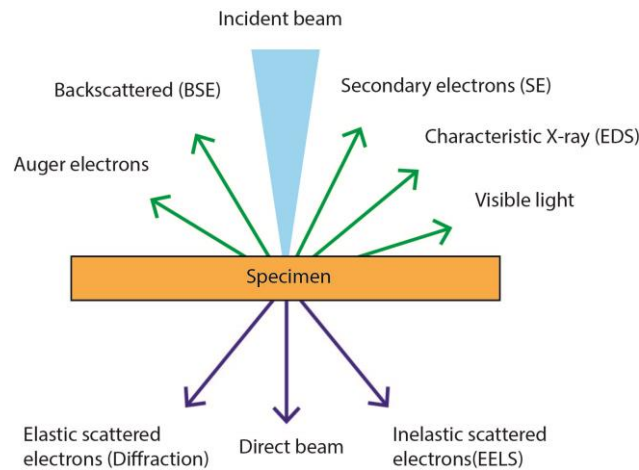


Figure 3-2: Signals generated from the interaction of electrons with the material atoms. EDS refers to energy-dispersive X-ray spectroscopy. EELS refers to electron energy loss spectroscopy.

The TEM imaging system has two basic operations: image mode and diffraction mode, which are controlled by electromagnetic lenses. In the bright field (BF) mode of the TEM, as illustrated in Figure 3-3, electrons scattered in the same direction focus on the back focal plane of the objective lens, forming a diffraction pattern. An aperture is placed in the back focal plane allowing only the direct beam to pass. The direct beam for forming the BF TEM image is weakened by its interaction with the sample.

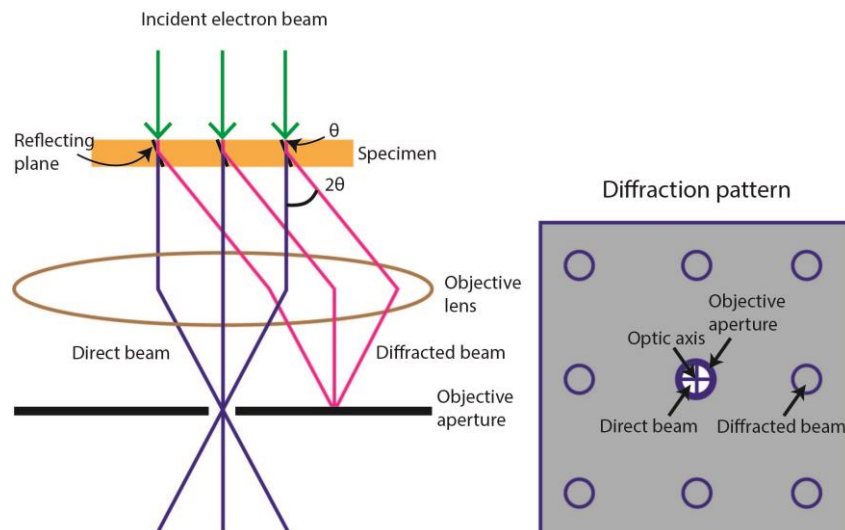


Figure 3-3: BF-TEM ray diagram. The object aperture catches scattered electrons while the direct beam passes through and contributes to a BF image.

Different from the parallel electron beam that is used in TEM, a probe formed by a convergent beam is scanned over the sample in scanning transmission electron microscopy (STEM). In STEM mode, the electron detector is used for selecting the signals that contributes to the image (Fig. 3-4). The high-angle annular dark field (HAADF) detector detects selectively the electrons that are scattered to higher angles, from which mass-thickness (Z)-contrast imaging can be achieved.

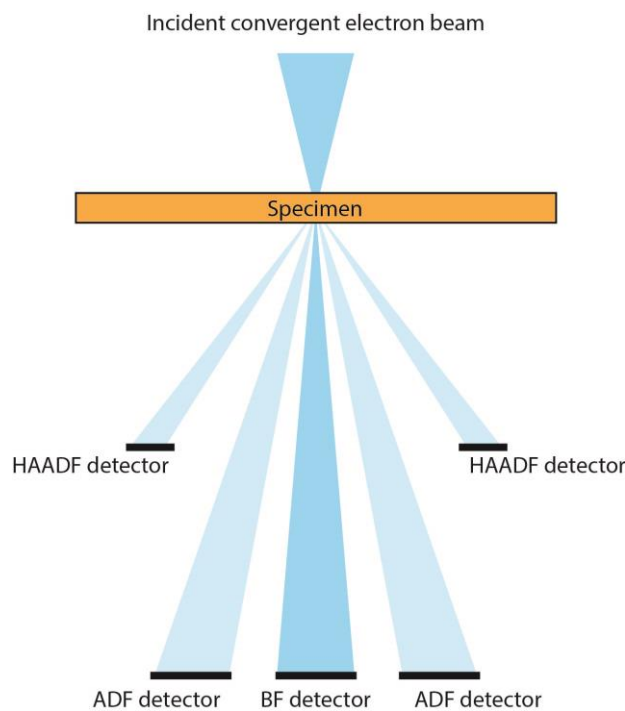


Figure 3-4: Schematic of conventional detectors in a STEM.

The highly localized signal stream from STEM enables the use of secondary electrons, scattered beam electrons, characteristic X-rays, and electron energy loss for analytical studies. STEM-based electron energy loss spectroscopy (EELS) and energy-dispersive X-ray spectroscopy (EDS) are widely used techniques for quantitative elemental analysis. EELS analyzes the energy distribution of transmitted electrons after they interact with the sample (Fig.3-2), providing information on elemental identity, chemical bonding, valence, and conduction band electronic properties.

X-rays detected in EDX are generated from a two-step process. As illustrated in Figure 3-5, the energy transferred from the electron beam to the atomic electron knocks it off, leaving a hole behind. This

position is then filled by another electron from a higher energy shell while emitting the characteristic X-ray. Such characteristic X-ray radiation can be used for both qualitative and quantitative analysis of the material components within the sample. EELS exhibits better energy resolution (<1 eV) than that in X-ray spectroscopy (about 150 eV) and it is more suitable for low atomic number elements.

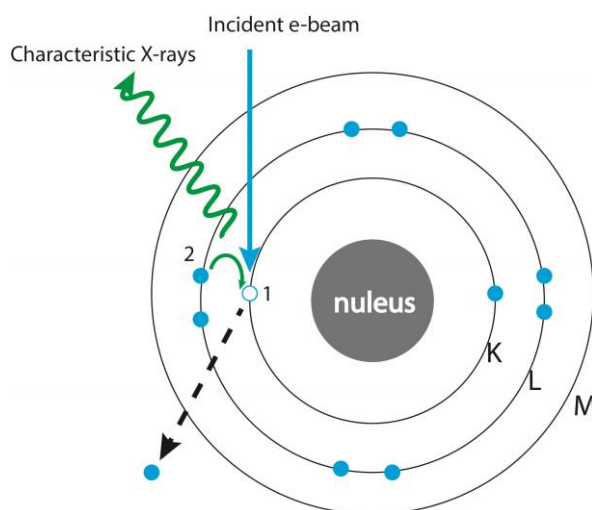


Figure 3-5: Schematic of characteristic X-rays generation in EDS.

3.2. Electrochemical liquid-phase TEM

To enable the analysis of specimens in the liquid phase in the TEM, specialized holders were introduced in the 1940s[115]. The breakthrough of the reliable fabrication of suspended silicon nitride (SiN) membranes (about 50 nm in thickness) on silicon chips granted the ability to encapsulate the liquid and isolate it from the vacuum chamber. Figure 3-6a demonstrates a liquid-electrochemistry holder tip that is used herein. The holder tip is designed to carry a micro-volume liquid enclosure sealed with two SiN-membrane chips by placing o-rings in between. The top electrochemical chip (Fig. 3-6b) is patterned with three electrodes: working, reference, and counter for performing electrochemical reactions in the liquid-cell. The bottom spacer chip determines the gap for enclosing the liquid and provides the thickness of the cell. The biasing contacts on the tip are directly in contact with the electrodes on the electrochemical chip and the internal microfluidic channels sit on two sides of the electrochemical cell

allowing the introduction of the liquid into the microcell. At the center of each chip is a $50\text{ }\mu\text{m} \times 200\text{ }\mu\text{m}$ window.

The performance of liquid-phase TEM and its experimental limitations have been explored by researchers in order to utilize its full potential for electrochemical analysis. In terms of TEM resolution, the highest resolution for an object within a liquid is achieved when the object is at the exit side of the sample along the electron beam[116]. The approximate value for a typical case can reach 4 nm. Electron beam-sample interactions are a key factor in any electron microscopy experiment. For liquid samples, a rigorous interpretation of results certainly requires an understanding of beam effects. Previous reports indicated that a dose of $500\text{ e}^-/\text{nm}^2$ is within the limit of radiation damage for *in situ* electrode studies in organic electrolytes[109], [117]. Additionally, the liquid environment is determined by the gap between the two SiN membranes that is provided by the spacer and, typically, the smaller the spacer, the thinner the liquid layer, and thus better resolution can be achieved for imaging.

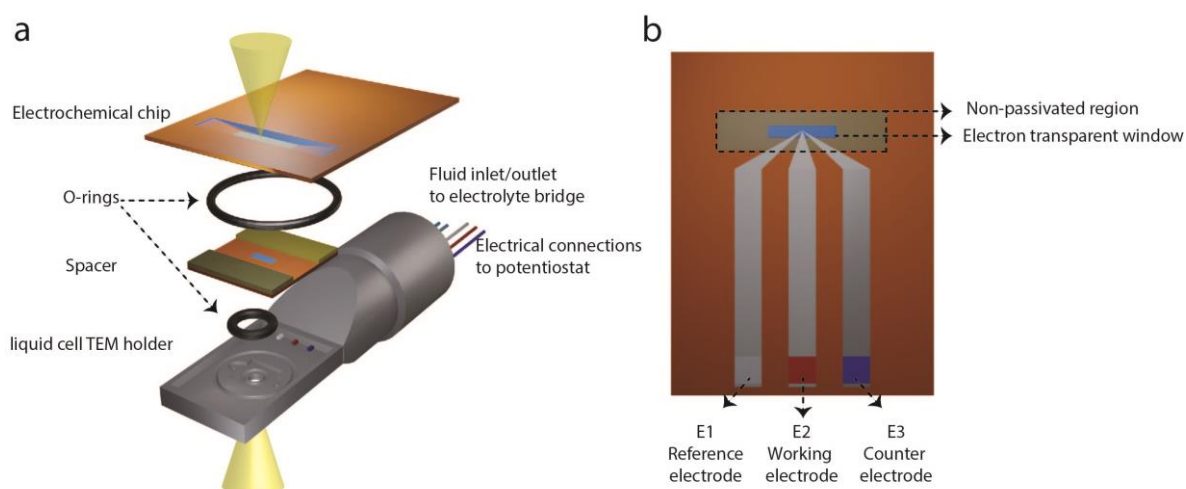


Figure 3-6: (a) Schematic of a liquid cell TEM holder. (b) The electrochemical chip is patterned with electrodes which can be connected with an external potentiostat.

3.3. Liquid-cell optimization for battery cycling

Optimization of the TEM liquid-cell operation for battery cycling can be established by harmonizing the electrochemical measurements from the liquid-cell with bulk cell measurements. Figure 3-7 shows the different battery configurations that were used in this work.

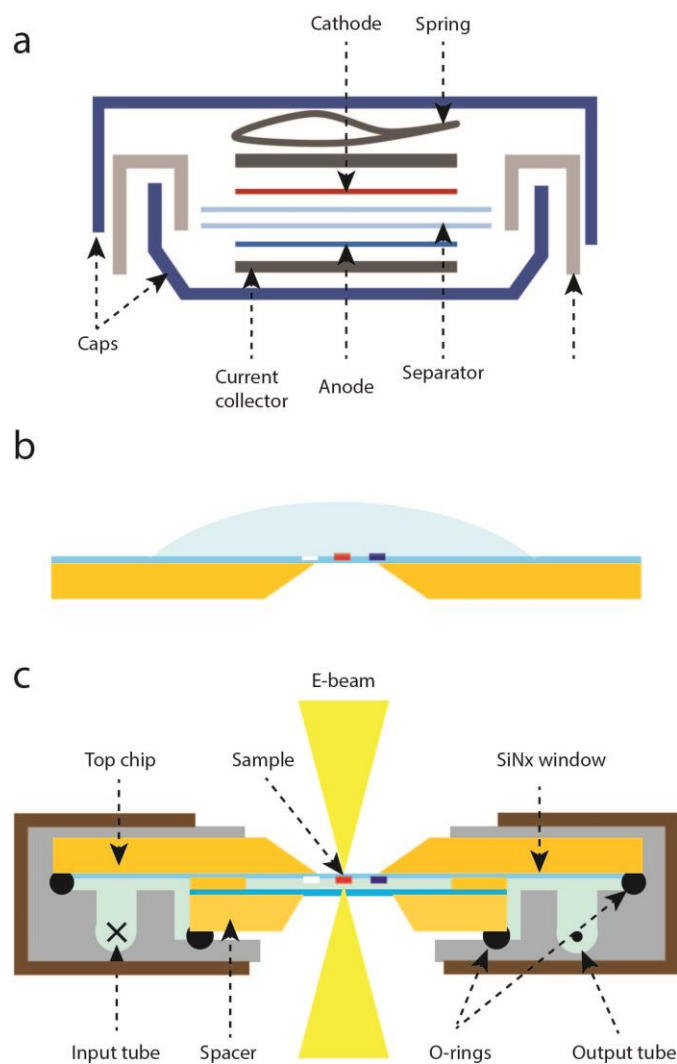


Figure 3-7: Schematic illustration of (a) coin cell, (b) open cell, and (c) liquid cell assembly for electrochemical battery measurements.

The most commonly used coin cell was assembled and cycled as the reference for the electrochemical performance of the sample. Also, an open-cell setup using the liquid-cell electrochemical chip but without the enclosed liquid environment was used for cycling to determine the electrochemical

performance of the chip. Finally, electrochemical experiments were carried out in a closed liquid cell mounted on the TEM holder (Fig. 3-7c). The electrochemical and microstructural results from the three methods were compared in order to ensure the stability of the liquid microcell.

3.3.1. Chip configuration

The electrochemical chip is the one that is patterned with electrodes, holding the most functionality for battery experiments in a liquid cell. Following initial designs[108], [116], diverse materials have been patterned either as electrodes or current collectors for loading materials in various configurations[118].

Herein, in-house designs were utilized to run the micro battery experiments in the liquid cell. A larger surface area of the working and counter electrodes is preferred to facilitate the requested electrode material loading. In contrast, the electrodes outside the viewable area in TEM need to be minimized for better coherence between the microscopic observation with the electrochemical measurement monitored by the potentiostat.

The sputtered metals used for the electrodes are vital for having a reliable electrochemical measurement during *in situ* experiments. To date, commercial electrochemical chips have been restricted in materials flexibility with Au, Pt, or C electrodes with a thickness of about 20 nm[108]. Since serving as electrodes or current collectors, the metals used ought to be inert toward the working environment that is composed of the volatile organic electrolyte and stable within the working conditions where a high potential range can be applied. Carbon has been abandoned for the liquid cell TEM studies on LIBs due to the possibility of it being involved as the electrode for lithium intercalation, complicating the electrochemical measurements of the target electrodes by potentially consuming lithium or having the risk of dendrite formation. Therefore, Au and Pt were chosen to be patterned on our in-house chip designs. The comparison between using Au and Pt either for the current collector or for lithiation substrate is presented in Figure 3-8. The Au is good for alloying with Li and can be applied as a reference for the electrochemical measurements, while Pt is stable as a current collector for running

cyclic voltammetry. Finally, the thickness of the electrodes is important. Due to the variation of particle size for forming a continuous thin film from Au and Pt, the electrode thickness limitation that can be achieved on an electrochemical chip is 50 nm and 15 nm for Au and Pt, respectively.

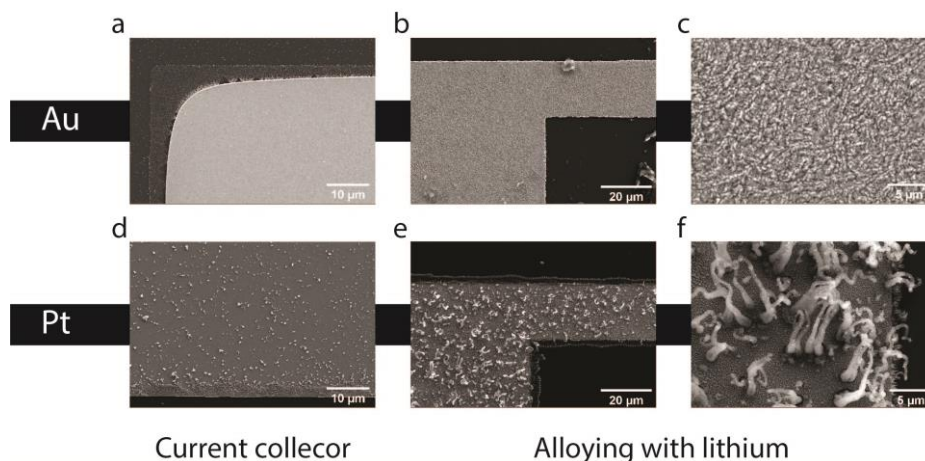


Figure 3-8: SEM images of the surface morphology of Au (a-c) and Pt (d-f) electrodes after cycling. They are utilized either as the current collector for loading electrode materials (a)&(d) or as the lithiation substrate for forming alloys (b)&(e). (c)&(f) are taken from (b)&(e) at higher magnification.

With respect to the battery operation of the liquid-cell, the geometry of the three co-planar patterned electrodes should be representative of the bulk electrochemical measurements. The reference electrode (RE) is typically between the working electrode (WE) and the counter electrode (CE), and different geometries have been fabricated. Figure 3-9a shows the original three electrodes with RE between WE and CE. In this configuration, only the WE is patterned within the window region. Figure 3-9b concerns a design where the working electrode is surrounded by the counter electrode that is partially patterned upon the membrane. A more homogeneous electric field distribution over the electrode surface during electrochemical cycling is expected from the working electrode-based symmetric pattern. Moreover, more narrow electrodes and the distance between them can enhance the electrolytes' coverage over the whole electrode surface, providing more controllable electrochemical conditions in the experiment. A slim reference electrode is set between the working and counter for facilitating the measurement of individual electrodes in the full cell setup. The exposed region on the counter electrode through the membrane is also desirable for examining the CE modification after cycling the WE.

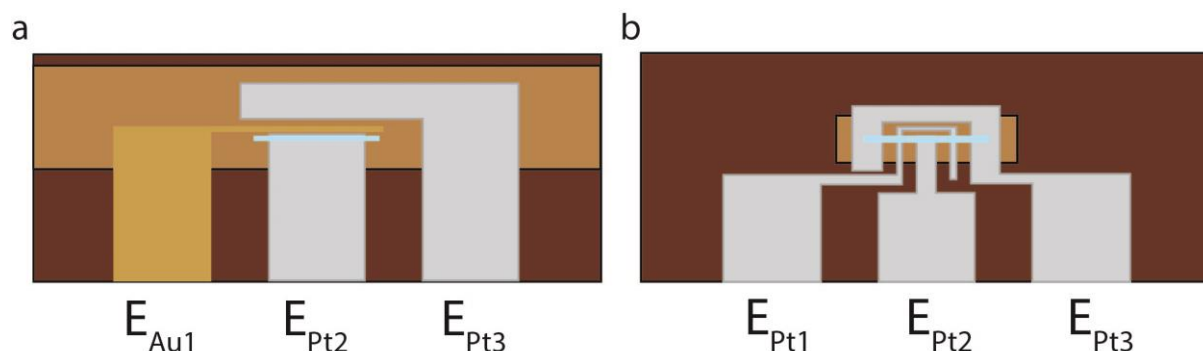


Figure 3-9: Two different designs for lithium-ion battery setup on the electrochemical chip. (a) has a gold electrode to be stabilized for applying as a reference electrode, while the working and counter electrode material is loaded on the Pt current collector. (b) has symmetric design over the electrically active region with all current collectors made from Pt.

3.3.2. Site-specific deposition of battery electrodes

3.3.2.1. Size modification of NCM cathode materials

NCM particles are hierarchical structured secondary particles (a few μm) that are assembled from primary particles (100s nm). As the size of the loading material is restricted in the sub-micron scale in the liquid cell, wet ball milling and ultrasonic wet-milling were chosen for crushing the NCM particles into their primary particle size without modifying the original crystal structure.

Firstly, planetary ball milling was applied to decrease the size of particles. The direction of movement of the sun wheel was set to be opposite to that of the grinding jars to superimpose the centrifugal forces, making the grinding balls collide at high impact energy. Since the difference in speeds produces an interaction between frictional and impact forces, the process was conducted stepwise for producing the high and effective degree of size reduction. Annealing is demanded in this method for restoring the potentially damaged crystal structure of ball-milled powder due to the violent collision.

Although the outcome from ball milling shows satisfied and controllable particle size reduction, the disassembling of secondary particles was also tried out through probe ultrasonication technique as a more convenient and efficient approach. Probe ultrasonication provides a practical and clean result for particle size reduction compared to conventional ball milling due to the absence of grinding beads and unnecessary sieving after each grinding step. Moreover, since the original secondary particles are

disrupted into primary particles directly in the suspension, the risk of agglomeration of small particles during electrode slurry preparation can be diminished as well.

The size distribution and crystal structure of processed particles are characterized by SEM and TEM in order to ensure the size restriction goal as well as the consistency of the material's crystal structure after processing. Figure 3-10 presents the size and structure of primary particles from both methods. The primary particles with a size less than 500 nm fulfil the requirement of membrane defined chamber in the liquid TEM cell. The primary particle of cathode material remains as a layered structure of $R\bar{3}m$ after milling and helps to rule out possible effects of structural modification during processing on the electrochemical performance.

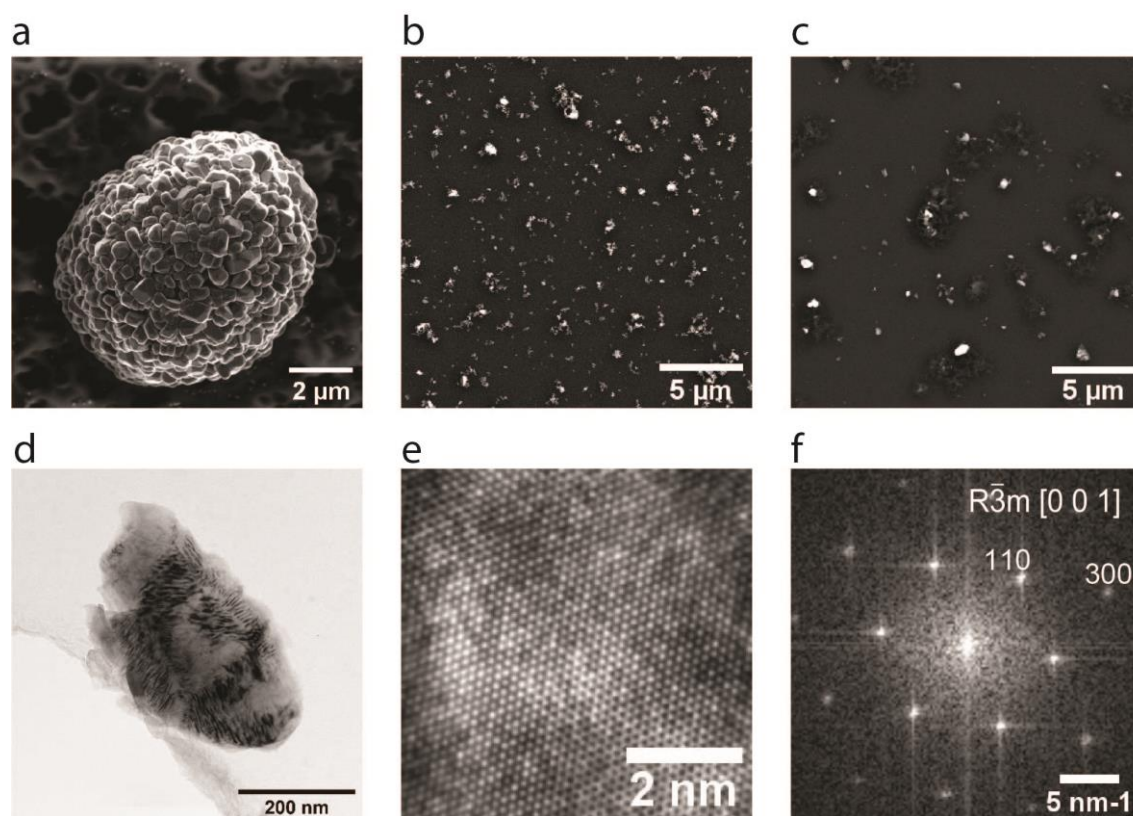


Figure 3-10: (a) SEM image of a pristine NCM622 particle. (b-c) SEM of processed NCM622 particles from ball-milling (b) and ultrasonic wet milling (c). (d) TEM image of a primary NCM622 processed from ultrasonic wet milling. HRTEM (e) and the corresponding FFT (f) of the edge of the particles in (d).

3.3.2.2. Working electrode preparation and loading

To introduce the crushed particles on the electrochemical chip, a suspension was prepared. It consisted of processed NCM particles, binders, and additives dispersed in an organic solvent (1-methyl-2-pyrrolidinone, NMP). The binders are introduced for keeping the electrode materials on the surface of the current collectors while the additives aim at improving the electron transfer through the interface of cathode material particles, hence accelerating the charge transfer process on the cathode surface and providing extra electron-conducting pathways among the cathode material particles and between the cathode material particles and the current collector[119]. A higher proportion of binder and additives is required for avoiding the agglomeration caused by the higher surface area on ball-milled NCM, enhancing the conductivity between the particles and current conductor. The ink was prepared in the ball-milling machine at low speed to enhance the dispersion. Finally, to site-specifically load the ink on the current corrector patterned on the electrochemical chip, a micromanipulator was used.

3.3.3. Electrochemical configuration for battery study in liquid cell

3.3.3.1. Three-electrodes connection

From an electrochemical perspective, a three-electrode method is utilized for investigating the fundamental physics of the battery operation by decoupling the two electrodes' responses. As illustrated in Figure 3-11a, in a three-electrode setup, a reference electrode is introduced for measuring the anode and the cathode separately during cycling, by which the contribution of each component in the system can be collected simultaneously and the mechanism of battery decay caused exclusively by the electrode material can be verified[120], [121]. Since no current can pass through the reference electrode, it provides an ideally stable voltage, leading to more precise measurements of individual electrodes' electrochemical potential without disturbing the cycling as a complete cell between the working and counter electrode. In the liquid cell where only individual particles are attached to the current collector for completing the electrochemical process, the proper selection of counter and reference also becomes

critical for having a reasonable micro-battery system. In such a configuration, for the counter electrode, graphite has been tried as it is commonly used in bulk cells[122]. Unfortunately, the processing of graphite into the size that can fit in the liquid cell is not very practical, which also makes it hard to load. The alternatives of graphite, such as lithium-metal alloys (e.g., LiZn, LiAl, and LiAg), however, are limited by their intrinsic properties, including volume expansion, delamination, and possibility of forming nanowires[123], [124]. Although the LiFePO_4 was first invented as a more stable cathode candidate for lithium-ion batteries, its low potential and electron mobility hinders its application in the electric vehicle field. However, it is a promising counter electrode specifically for micro battery systems, since the delithiated LFP is a great Li host with a high capacity (485 to 375 mAh/g) [125].

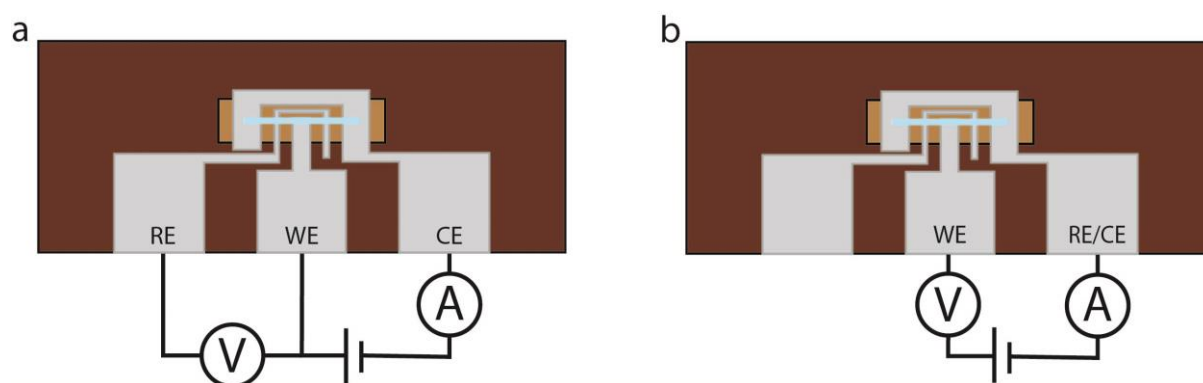


Figure 3-11: Schematic illustration of (a) three-electrodes and (b) two-electrodes cell connection for lithium-ion battery testing during cycling.

3.3.3.2. Two-electrodes connection

Although the abovementioned setup is capable of measuring the performance of the working electrode while mimicking its cycling condition in a full battery, it needs to be further optimized to simplify the complex and time-consuming reference stabilization by lithiation before running the three-electrode connection system for battery testing. An alternative reference electrode is LFP since it has a flat voltage plateau at 3.4V vs. Li/Li^+ over a wide range of state of charge [3]. A well-defined reference potential

can be obtained by LFP, and thus delithiated LFP can serve as a reference electrode for the electrochemical chip-based micro-battery system. To prepare delithiated LFP, the LFP particles were first dropcasted onto the counter electrode and delithiated by transferring its Li onto the blank Au electrode by forming Li_xAu alloy. The delithiated LFP serves not only as a counter electrode for hosting lithium but also as a pseudo-reference electrode maintaining the stable potential over the measurement during cycling. Therefore, the system can be simplified to a two-electrode configuration reliable setup (Fig. 3-11b).

3.4. Identical location studies

Identical location transmission electron microscopy (IL-TEM) concerns imaging of the same specimen at the same spot before and after the electrochemical treatment. The electrochemical treatment of cathode particles is conducted in the electrolyte sealed in the liquid-cell holder, while the microscopic characterization before and after the operation is performed in conventional TEM. Thus, the surface modification and other structural and compositional features at the nanoscale can be identified. Compared to electrochemical *in situ* liquid cell TEM, which introduces extremely demanding technical challenges for reproducibility and data interpretation that are caused by the potential variation in the TEM and the interaction of electron-beam with electrode material and supporting electrolyte, IL-TEM is a non-destructive method that allows monitoring of the electrode material's evolution without external factors affecting the electrochemical conditions during operation. High-resolution TEM (HRTEM), scanning TEM (STEM), and energy-dispersive X-ray spectroscopy (EDS) were combined to identify structural and compositional changes after the electrochemical operation on the Ni-rich cathodes. It is noted that despite the fact that spatially resolved TEM methodologies are widely applied for elucidating the structure-property relationships for the rational design of advanced batteries, the electron beam damage is a common phenomenon, complicating data interpretation. Feng et al. have reported the possibility of the reduction of the transition metal ions by knocking out or evaporating lithium and oxygen ions from the cathode material caused by electron irradiation, which may possibly

lead to structural reconstruction [116]. As such, special attention was taken to avoid electron beam irradiation damage for identical location studies.

3.5. Analytical electron microscopy

3.5.1. Radiation impact

The electron beam may potentially bring knock-on, ionization, and thermal effects on the analyzed sample, leading to degradation of the material and artefacts in the analysis. It has been reported that the critical dose limit for keeping the chemical and structural stability of LIB electrode material is about $750 \text{ e}^-/\text{\AA}^2$ for lithium carbonate and roughly $6 \times 10^6 \text{ e}^-/\text{\AA}^2$ for NCM materials, which are more resistant to electron beam degradation[126]. Moreover, the electron dose rate, which is the beam current normalized by the irradiated area, is also a critical parameter for evaluating the potential radiation damage on the observing samples[127]. The regular STEM-EDS analysis condition of the transition metal ions within NCM particles was performed with a dose of roughly $1.56 \times 10^7 \text{ e}^-/\text{\AA}^2$ with an electron probe of 0.5nA. This could introduce artifacts such as the Ni/Li disorder, oxygen release, and structural degradation, as a result of electron beam irradiation. However, in the following, the discussion focuses on the migration of the different transition metal ions or the elemental distribution within a particle of size up to a few hundred nanometers, which remains at most unaffected by the electron dose rate used for the experiments herein[128]–[130].

3.5.2. Errors in the EDS chemical mapping

For compositional analysis, chemical mapping with STEM-EDS would provide not only the location of specific elements but also some description of their relative abundance within a particular region. In principle, measuring X-ray spectra from EDS allows identification of the sample composition and is typically sensitive down to levels of about 0.5 to 1 atomic percent and 0.1 weight percent. However, obtaining accurate quantitative data from EDS is challenging due to the different X-ray fluorescence yields and absorption rates for the different characteristic lines being analyzed[131].

To accurately determine the number of counts in spectral peaks that is associated with each element in the sample, it is assumed that the counts reflect the concentration of the present elements. In practice, the quantification is a two-step process. First, the Bremsstrahlung (background or continuum) X-ray counts are subtracted and, then, the characteristic X-ray peaks are post-processed. The number of Bremsstrahlung X-rays varies with the mean atomic number (Kramer's Law), while every element in the sample has an effect on the measured characteristic X-ray intensity of each peak in the spectrum. Therefore, various correction methods are applied for dealing with this nontrivial relationship for quantitative microanalysis. For example, the "ZAF" correction compares the number of X-ray counts in the peak of interest to standards with a known concentration of the element of interest. The concentration of element of interest c_i can be approximated by the X-ray intensity of characteristic peak line I_i , and a sensitive factor K , as presented in Eq. 3-1.

$$C_i C_i^{std} = [K] I_i / I_i^{std} \quad (3-1)$$

Three factors contributing to the K parameter: "Z", the mean atomic number; "A", the absorption of X-rays absorbed in the specimen, and "F", the fluorescence of X-rays within the specimen.

Herein, the quantitative EDS analysis utilized the standard Cliff-Lorimer (K-factor) quantification, combined with absorption correction, as implemented in the Velox software from ThermoFisher Scientific. Instead of using a standard, the weight percent of each element, such as C_A and C_B was related to the characteristic intensities I_A and I_B directly following Eq. 3-2.

$$\frac{C_A}{C_B} = k_{AB} \frac{I_A}{I_B} \quad (3-2)$$

The Cliff-Lorimer factor k_{AB} is related only to the atomic-number correction factor "Z" as that in the ZAF correction method. The absolute value of concentration for each element was therefore obtained by assuming that the selected elements constitute 100% of the specimen. For instance in a binary system: $C_A + C_B = 100\%$. [132] Using this approximation, the absorption and fluorescence terms are neglected, which is a reasonable assumption for electron transparent specimens.

In addition to the sample, the electron optics, specimen holders, and associated detectors are also essential for estimating potential errors in the analysis system[133] For our chip-based system, quantitative elemental analysis becomes more challenging due to the difficulty of accounting for unwanted electron scattering from the SiN windows and metallic current collectors, that are serving as substrates for target electrode materials.[134]. Thus, possible spectral artefacts involved in our experimental setup may arise from the inaccurate atomic number correction (Z) and the absorption correction (A) due to the varying thickness across the probed region of the sample with different composition and density, especially when the sample contains low (Li) and high (Pt) atomic number elements at the same time. Additionally, the relative low number of counts used due to the sensitivity of the electrode materials to the high energy electron beam in STEM mode, may further limit the accuracy of counting statistics. Thus, the error in the EDS quantification maps of the cathode particles on the electrochemical chip is expected to be higher than in the case of typical EDS analysis of electron transparent specimen (up to 2 atomic percent). Nevertheless, in this study, the relative fraction of transition metals among the particle based on the EDS analysis is supposed to offer a semi-quantitative indication for electrode materials modification after cycling. This methodology is therefore used as a practical, compositional analysis technique for the trends encountered during in situ electrode cycling of cathode materials.

Chapter 4: Li-Au alloy as micro-reference electrode

The contents of this chapter are based on the published article [135]:

Lithium-Gold Reference Electrode for Potential Stability During *In situ* Electron Microscopy Studies of Lithium-Ion Batteries

Jing Hou, Robin Girod, Nikolaos Nianias, Tzu-Hsien Shen, Jialiang Fan, and Vasiliki Tileli

Institute of Materials, École Polytechnique Fédérale de Lausanne, CH-1015 Lausanne, Switzerland

J. Electrochem. Soc. 167 110515 (2020)

DOI: 10.1149/1945-7111/ab9eea

Contribution of J.Hou: Performed sample preparation, characterization, data analysis and wrote the manuscript with contributions from all authors.

4.1. Introduction

For *in situ* TEM studies, the range of usable electrode materials is constrained by the scale of the cell and by the micromechanical fabrication procedure of the components of the cell. As a result, commercially available electrodes are currently limited to Pt, Au, Ni, Cu, or C/Pt. The use of these materials as quasi-reference electrodes (QRE) presents two important shortcomings. First, QREs may exhibit critical potential shifts over time or may be modified during operation. This is particularly the case with *in situ* TEM where the influence of the electron beam on the electrolyte and the electrodes themselves remains poorly controlled. Second, limited literature is available on the use of these QREs for the study of LIB electrode materials, making it difficult to readily interpret and compare electrochemical results obtained in the TEM with bulk studies.

The challenge of implementing a stable micro-reference electrode in a battery is not, however, exclusive to the *in situ* microscopy field. There is a growing body of literature on reference electrodes in electrochemical impedance spectroscopy (EIS) investigations of LIBs where a Li reference electrode is electrochemically deposited or alloyed with metallic wires. In such experiments, a micro-sized reference electrode is indeed crucial to mitigate disruptions in the electrical field between symmetrical working and counter electrodes. Zhou et al. used electrodeposited lithium on a copper wire. However, depending on the plating parameters, the properties and stability of the plated film were impeded by the continuous SEI formation and dissolution of lithium ions into the electrolyte[136]. Recently, Solchenbach et al. used a gold wire that thermodynamically resulted in an alloy when lithiated[137]. Due to the greater chemical stability of Li-Au alloys and to a small exposed area with regard to the total alloyed volume, their reference electrode was stable for several weeks and exhibited a reference potential indicative of a Li_xAu ($0 < x < 1.2$) alloy[138].

Stemming from the interest in Li_xAu as an anode material, previous *in situ* TEM studies focused on the cycling behavior and structural evolution of gold films during lithiation and delithiation[113], [139]. While these reports establish the feasibility of electrochemically alloying lithium and gold in an *in situ* TEM apparatus, their methodologies need to be adapted, and mild alloying conditions need to be

defined in order to achieve a structurally undamaged and stable reference electrode for electrochemical electron microscopy studies.

Here, we report on the alloying of lithium with a gold micro-electrode thin film patterned on the electrochemical chip and on its performance as a stable reference electrode for liquid-phase TEM investigations of LIBs. We first establish the feasibility of this procedure *ex situ* and outside of the TEM holder and investigate various sources such as metallic lithium, LiFePO_4 delithiation, and reduction of Li salt containing electrolyte, to support the lithiation of the gold micro-electrodes using chronopotentiometry (CP). We investigate the morphological modifications induced by this step with scanning electron microscopy (SEM) and TEM and confirm the formation of a Li-Au alloy using electron energy-loss spectroscopy (EELS) and high-resolution (HR)TEM. We then show that this methodology can be applied directly in an *in situ* TEM holder to obtain a Li_xAu reference electrode stable over hours whose potential can be directly related to bulk values from the literature. We cycle LiFePO_4 as a model cathode and show that reproducible and coherent measurements can be performed outside and *in situ* in the TEM with limited effects of the electron beam on the electrochemical signal, thereby demonstrating the merit of our reference electrode for future *in situ* TEM investigations of LIB electrode materials. Finally, the chemical stability of the electrolyte during the full process is confirmed by nuclear magnetic resonance (NMR) spectroscopy.

4.2. Experimental

4.2.1. Electrochemical micro-chips for *in situ* TEM measurements

The chips have been designed and manufactured in-house to fit in a TEM liquid-electrochemistry holder (Hummingbird Scientific, Lacey, WA, USA) and create a microfluidic cell [140], [141]. The configuration used in this study features two platinum electrodes ($\text{E}_{\text{Pt},2}$, on the window, and $\text{E}_{\text{Pt},3}$, the counter one) and one gold electrode in the middle ($\text{E}_{\text{Au},1}$) intended to be lithiated and used as the reference electrode. The patterned electrodes are partially isolated from the electrolyte by a passivation layer (SiO_2) deposited on top, except for the regions of the electron transparent window and of the

contacts with the holder pins. By doing so, the electrochemical reaction sites can be optimized within the viewing region. The non-passivated (electrochemically active) surface areas of the three electrodes are 0.1553 mm^2 for $E_{\text{Au},1}$, 0.11 mm^2 for $E_{\text{Pt},21}$, and 0.4974 mm^2 for $E_{\text{Pt},3}$.

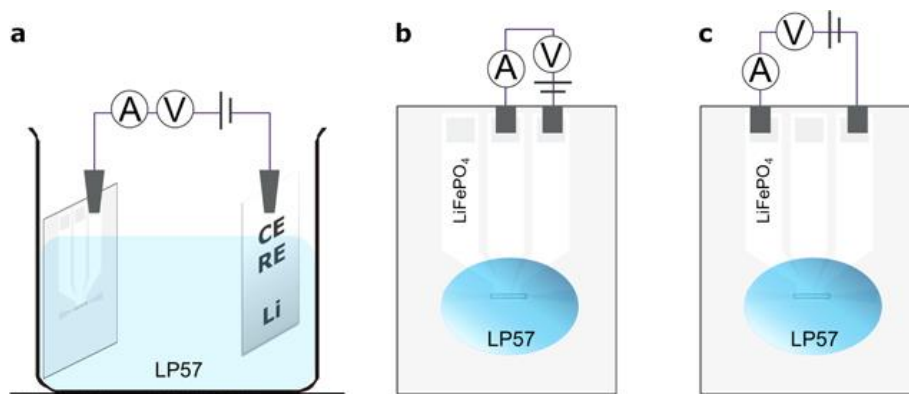


Figure 4-1: (a) The glass cell setup for gold lithiation by metallic lithium. Lithium was clamped as counter and reference electrode, while the gold, working electrode on the chip was lithiated by applying negative current. (b)–(c) The open cell setup for gold lithiation either from the electrolyte (b) or LiFePO₄ particles (c). LiFePO₄ particles were dropcast on the electrode that has the largest conductive surface.

4.2.2. Site-specific deposition of LiFePO₄ (LFP) particles

For LFP deposition on $E_{\text{Pt},2}$ or $E_{\text{Pt},3}$, the particles were dispersed in a solution of 10 mg/ml polyvinylidene fluoride (PVDF, Kynar HSV 900) dissolved in 1-methyl-2-pyrrolidinone (NMP, 99.5%, AcroSeal) that act as a binder for the particles, in a weight ratio of 1:6. The suspension was pipetted with a capillary (Narishige GD-C 1, Tokyo, Japan) pulled by a Narishige puller (Narishige PC-10, Tokyo, Japan), and then was dropcast on the selected electrode using a micromanipulator (Narishige MMO-4 hydraulic micromanipulator combined with a mechanical coarse manipulator) in ambient atmosphere. The prepared chip was heated at 60 °C for 12 h to remove NMP in the Ar-filled glovebox.

4.2.3. Reference electrode preparation in open-cell configuration.

Open cell setup conducted in the glovebox was used for practical reasons and in order to allow for various materials to be tested as lithium sources for alloying. In particular, galvanostatic lithiation of

gold thin films supported by metallic lithium or by decomposition of lithium hexafluorophosphate salt (LiPF_6)-containing electrolyte has been reported in the literature[138], [142], [143]. In addition to those known lithium sources, we also investigated the feasibility of using the charge (i.e. oxidation at the counter electrode) of LFP particles to support the lithiation current, in an attempt to avoid electrolyte decomposition.

When using metallic lithium, experiments were conducted in a beaker as presented in Figure 4-1a, with the chip and a lithium plate clamped separately as the working and counter/reference electrodes respectively and both immersed in a standard electrolyte containing 1 M LiPF_6 in a 3:7 weight ratio of ethylene carbonate (EC) and ethyl methyl carbonate (EMC) (LP57, w-w < 20 ppm H_2O , BASF SE, Germany). Lithiation from LP57 reduction or LFP particles delithiation was carried out by mounting the chip on a flexible flat cable/flexible printed circuit connector (FFC/FPC, Molex, 52207 series), allowing for connection with all three electrodes outside of the holder while leaving the non-passivated area exposed (Fig. 4-1b&c). A 2 μl droplet of electrolyte was cast on the electrodes within the membrane region. The gold electrode was lithiated by applying a current between the counter electrode ($\text{E}_{\text{Pt},3}$ pristine, or LFP deposited on $\text{E}_{\text{Pt},3}$) and the gold electrode. Nominal C rates were derived from the applied current and a calculated initial gold weight estimated from the gold electrode surface area (0.1553 mm^2), using the bulk value of the density of gold ($\rho_{\text{Au}} = 19.3 \text{ g cm}^{-3}$). The chip was rinsed with dimethyl carbonate (DMC, anhydrous, $\geq 99\%$ Sigma-Aldrich) after lithiation and was dried at 60 $^\circ\text{C}$ in the glovebox for post mortem characterization with electron microscopy, including SEM, STEM and EELS.

4.2.4. Chemical stability assessment after lithiation

Once the electroplating of lithium was finished (or after the *in situ* experiments), the electrolyte was collected in an NMR tube within the Ar glovebox and mixed with dimethyl sulfoxide- d_6 (DMSO-d_6 , 99.9 atom % D, anhydrous Sigma-Aldrich). The solution was then subjected to analysis with liquid NMR spectroscopy (AV NEO-400, Bruker, 400 MHz).

4.2.5. Reference electrode assessment in liquid-cell

Prior to experiments in the holder, the electrochemical chip was air-plasma treated at 100 W for 2.5 min. After assembling the cell with a bottom chip (spacer, 1 μm) in ambient atmosphere, the holder was stored under vacuum for 1–2 h for degassing before transferring it inside an Ar-filled glovebox, so that the remaining air and moisture were removed from the assembled cell through the open microfluidic tube. Ar was then passed with a syringe through the liquid cell to remove possible air/moisture residues. The electrolyte (LP57) was introduced into the liquid chamber by the microfluidic tubes under the Ar atmosphere until a stable potential reading was achieved on the three electrodes.

Lithiated gold reference electrodes from LFP particles delithiation were prepared in the liquid cell by applying a current of 500 nA for 3 h between the LFP loaded counter electrode ($E_{\text{Pt},3}$) and the gold electrode, while the third electrode ($E_{\text{Pt},1}$), also loaded with LFP, was used as the effective reference electrode. The electrolyte was continuously flowed through the liquid cell with the help of a pumping system at a flow rate of 5 $\mu\text{l}/\text{min}$. Open circuit voltage measurement for 30 min was conducted after finishing the lithiation. For CVs of LFP, the connections were swapped to use the lithiated gold as the reference electrode, and $E_{\text{Pt},2}$ was cycled against $E_{\text{Pt},3}$ at 20 mV s^{-1} between 1.5 V and 5.5 V vs Li_xAu for five cycles. All the described electrochemical measurements were carried out in the glovebox. After sealing the fluidic tubes, the liquid cell was transferred to the TEM. Measurements were repeated for comparison.

4.2.6. Electron microscopy

Morphology analysis was performed in a Zeiss Merlin SEM. Electronic structure and composition studies were performed by HRTEM (Talos 200 kV, ThermoFisher Scientific, USA) and EELS (Titan Themis 200 kV, ThermoFisher Scientific, USA). The *in situ* TEM was performed on a TEM operated at 200 kV (JEOL 2200FS, Japan).

4.3. Results and Discussion

4.3.1. Benchtop galvanostatic lithiation of gold reference electrode from various sources

As a first step, galvanostatic lithiation of gold thin film reference electrodes patterned on the electrochemical chips was investigated in open cell. Figure 4-2a shows the cell potential curves during gold lithiation supported by the oxidation of metallic lithium (at a nominal 32.67 C rate, 10 min, solid green curve), of LFP (3.27 C, 1 h, dotted red curve), and of the electrolyte (3.27 C, 1 h, dashed blue curve). Note that the open cell setup for lithiation from metallic lithium, LP57, or LFP is different, as described in the experimental part (and illustrated in Fig. 4-1) so that the potential differences are measured either between the gold electrode and lithium counter electrode (case of lithiation from metallic lithium) or between the gold electrode and another platinum electrode patterned on the chip either deposited with LFP particles or left pristine (case of LP57 reduction). In all three cases, a distinct first potential plateau can be observed (around 0.2 V vs Li/Li⁺ in the metallic lithium experiment within the glass beaker, Figure 4-2a, solid green curve, coherent with values reported for gold lithiation and Au-Li phase transformation and around -6 V for the other experiments on the chip)[137]. A second plateau appears at -6.2 V in the LP57 case. In comparison, during lithiation from metallic lithium, the first plateau remains stable until the end of the experiment, while during lithiation from LFP, the cell voltage after the first plateau decreases slowly until the experiment is stopped. When LP57 is used as the lithiation medium, a clear potential drop at -6.2 V is observed at the beginning of the experiment before stabilizing at the first plateau, while the potential curve during lithiation from LFP does not exhibit any similar initial dip and stabilizes within 10 min of the experiment.

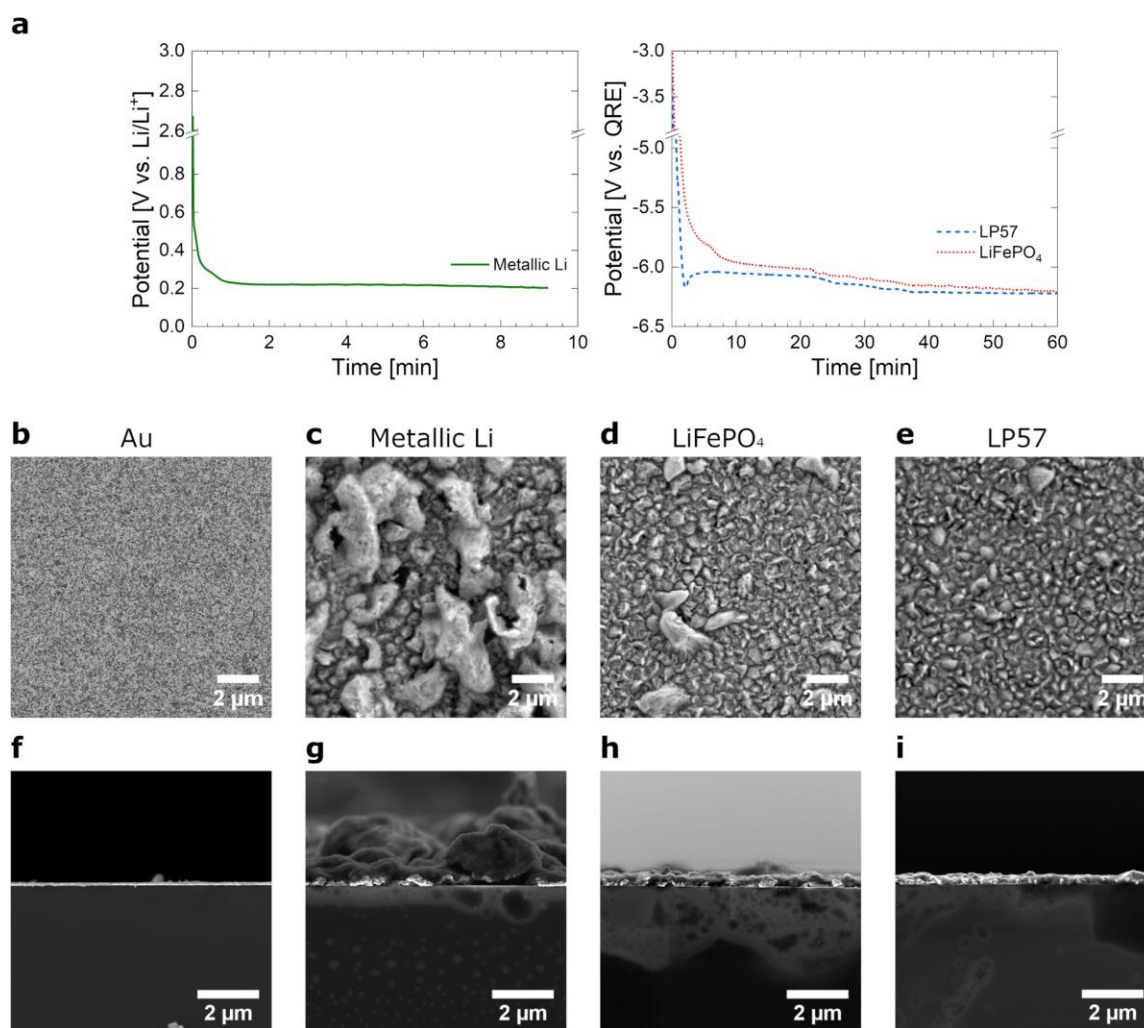


Figure 4-2: (a) Comparison of potential evolution of lithiated gold during galvanostatic lithiation from metallic lithium oxidation (solid green curve, vs Li/Li^+) at a 32.67 C rate (2 μA), from reduction of LP57 (dashed blue curve, QRE is Pt) and from LiFePO_4 particles oxidation (dotted red curve, QRE is LFP) both at a 3.27 C rate (200 nA). Top-view (b)–(e) and cross-sectional (f)–(i) SEM images of the pure Au electrode and the lithiated gold electrodes from metallic lithium, LiFePO_4 , and LP57.

The coherent potential curves observed against Li/Li^+ during lithiation from metallic lithium show that the setup used for this experiment allows lithium ions to transfer from the counter electrode to the gold electrode efficiently. On the other hand, the large cell voltage recorded during lithiation from LP57 could indicate the decomposition of the electrolyte, with high oxidative potential required at the counter electrode in order to support the lithiation current. LFP nanoparticles used for the last experiment are likely to delithiate in the first minutes of the experiment, causing the small potential shoulder observed at -5.8 V (Fig. 4-2a—dotted red curve) and the discrepancies with the lithiation experiment from LP57.

It is likely that the amount of lithium available from LFP is not enough to sustain the complete lithiation of the gold electrode and supplementary Li-ions from the electrolyte become necessary over time.

Top-down and cross-sectional SEM images of the lithiated gold electrodes are depicted in Figure 4-2b-i. Compared to a pristine gold electrode surface (Fig. 4-2b), 300–500 nm diameter grains can be observed on the three lithiated electrode surfaces. Bulky extrusions of several microns are exclusively seen from the surface lithiated with metallic lithium with higher current. In the cross-sectional images, an inhomogeneous lithiation front within the gold electrode can be observed in all cases, with discrepancies in the depth of penetration between the methods. Differences in the surface layer morphology and thickness can also be observed, with the electrodes lithiated from LFP and LP57 exhibiting a thin ~200 nm surface layer while the electrode lithiated from metallic lithium has a 1–2 μm layer clearly visible on top of the gold film.

These discrepancies between the methods could arise from the different rates used to lithiate the gold electrodes. Additionally, the protruding surface features are likely related to overcharging and subsequent lithium deposition, as the nominal C rates used were relatively high and were maintained beyond the specific capacity of the most Li-rich phase (Li_3Au , 408 mAh/g). It is noted that the rates used in this study were dictated by the setup. Reasons remain unclear, but when low current was applied to the cells (typically when inferior to 100 nA), the potential did not stabilize for the duration of the experiment, and no lithiation was observed. Finally, cell voltage plateaus during lithiation using metallic lithium or LP57 were stable well beyond the overcharge state. We hypothesize that this behavior arises from the lithiation of the silicon substrate which takes place around 0.1 V vs Li/Li^+ , as the back of the chip was also connected by the clamp, as well as from possible diffusion of lithium under the passivation layer[144].

Based on these results, gold electrode lithiation can be performed directly on the electrochemical TEM chips and the lithium source can be adjusted between metallic lithium or LP57. While deposited LFP seemingly does not provide enough lithium for lithiation of the gold electrode, obtaining lithium-

depleted particles at the counter electrode can nevertheless provide an interesting anode material for *in situ* studies of high-potential cathodes such as Ni–Co–Mn layered oxides[145].

4.3.2. Benchtop evaluation of lithiated gold stability

To evaluate the stability of the lithiated gold electrode, we performed OCV measurements following an open cell lithiation at 100 nA for 3 h with LFP deposited on the counter electrode, Figure 4-3. After the lithiation, the gold electrode potential ramps up to an initial relatively stable region at ~ -3.3 V vs LiFePO₄ within 40 min. Subsequently, a second plateau around -3 V appears at the 200 min mark and remains for the next 6 h, until the end of the measurement. Considering an LFP potential at 3.42 V vs Li/Li⁺, the two observed regions would correspond to potentials of ~ 0.1 V vs Li/Li⁺ and ~ 0.4 V vs Li/Li⁺, matching well with gold delithiation plateaus previously reported in the literature and indicating a final Li_xAu alloy with $0 < x < 1$ [138], [145], [146].

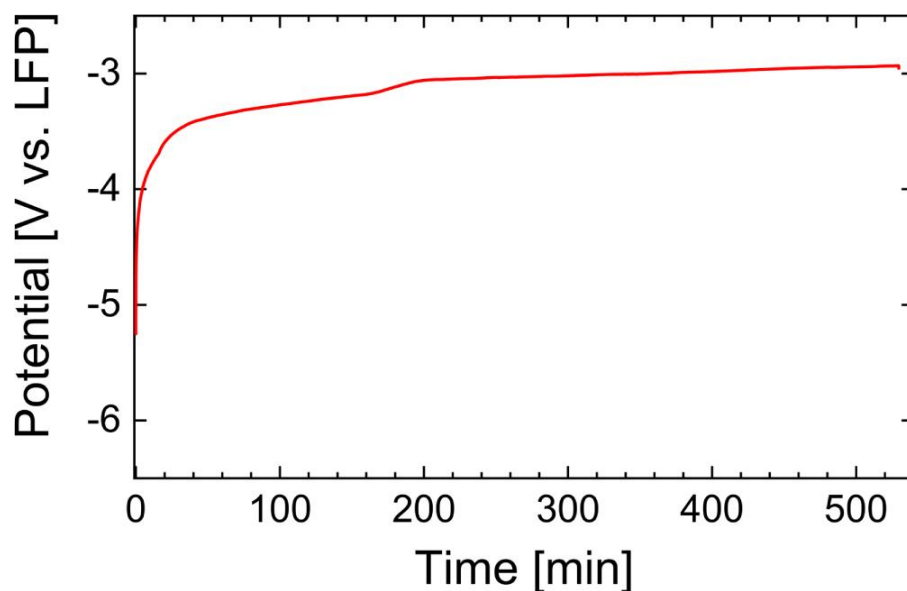


Figure 4-3: Open circuit voltage between lithiated gold electrode and delithiated LFP after 3 h of galvanostatic lithiation at 100 nA in the open cell.

We attribute the good stability of the second plateau to the diffusion of lithium under the passivation layer during galvanostatic lithiation. Since this area is not directly exposed to the electrolyte during the OCV, it would provide a lithium reserve which prevents lithium depletion in the non-passivated area, therefore mitigating possible SEI formation and side reactions with the electrolyte.

4.3.3. Characterization of lithiated electrode

To further confirm that Li is inserted in the structure, we performed TEM structural and chemical analysis. Figure 4-4a shows an EEL spectrum acquired at the edge of a previously lithiated gold electrode, with the peak at 55 eV unambiguously confirming the presence of Li. STEM images of the gold electrode before and after lithiation are shown in Figure 4-4b–c. After lithiation, the structure becomes less dense and exhibits a porous structure that is consistent with previous studies on the fabrication of nanoporous metals by electrochemical alloying and de-alloying with lithium[147], [148]. Finally, HRTEM micrographs of the pristine and lithiated gold electrodes were compared in order to acquire information on phase changes in the structure. The fast Fourier transform (FFT) of HRTEM image taken from the pristine electrode in Figure 4-4d, shows cubic packed gold crystal structure. In contrast, the lithiated Au particles exhibit a crystalline pattern that matches well with the $[0\ -1\ 2]$ zone axis of tetragonal AuLiO_2 alloys, Figure 4-4e. The oxidation likely results from the transfer of the lithiated chip outside the glovebox for the *ex situ* analysis.

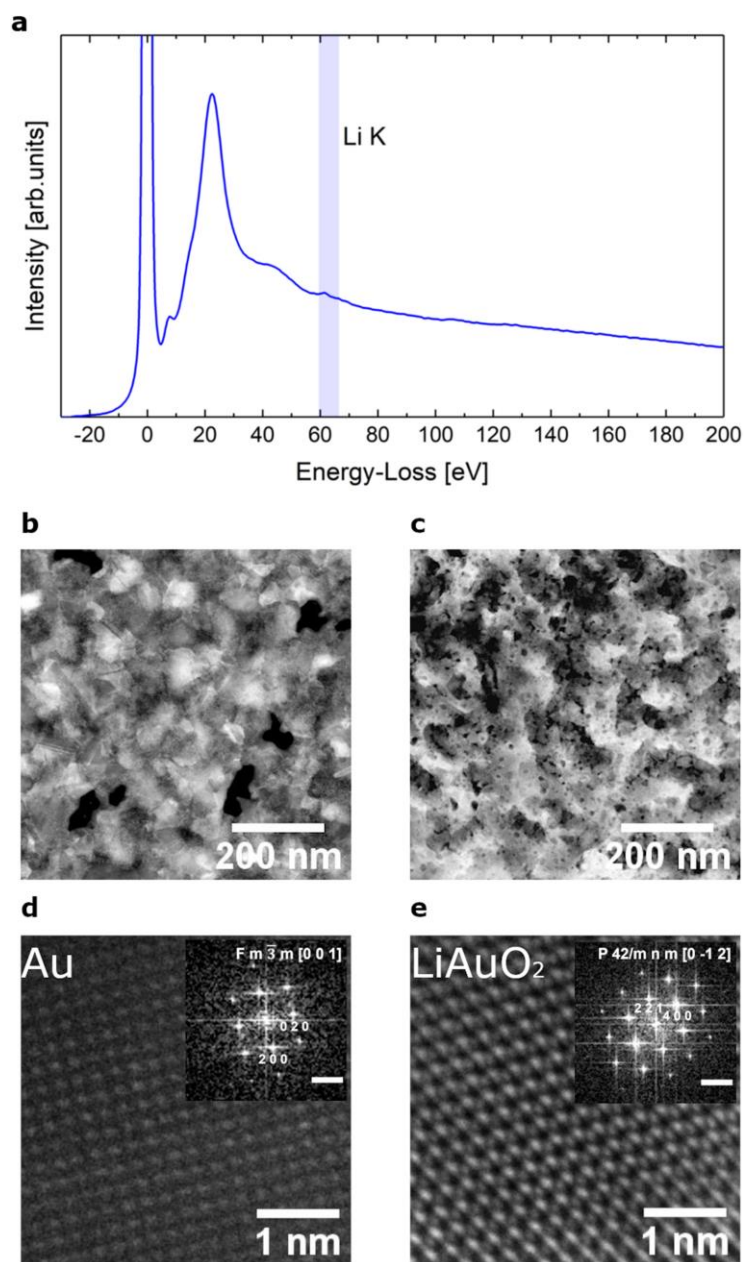


Figure 4-4: (a) Low-loss EEL spectrum of lithiated gold. (b)–(c) STEM images of bare and lithiated gold electrode. (d)–(e) HRTEM micrographs of the pristine gold electrode and of the lithiated gold respectively. The insets are the corresponding FFTs with the scale bar of 5 nm⁻¹.

4.3.4. Galvanostatic lithiation of gold reference electrode in liquid cell

Having confirmed the feasibility of fabricating a Li_xAu micro-electrode patterned on a chip, we examine its electrochemical performance for *in situ* experiments. A liquid cell was assembled in the *in situ* TEM

holder, with LFP deposited on both platinum electrodes. The reference electrode was lithiated inside the glovebox by applying a 500 nA current between the counter electrode ($E_{Pt,3}$) and the gold electrode for 3 h under a $5 \mu\text{l min}^{-1}$ electrolyte flow rate. The cell voltage during the galvanostatic lithiation and the following 30 min OCV is presented in Figure 4-5a. A plateau at -5.5 V was observed, with a decrease to -6 V after 130 min. While the cell voltage does not show as well-defined plateaus as during the open cell experiments, the subsequent OCV indicates a lithiated gold reference electrode potential of -3.3 V vs LFP, coherent with the previous measurements.

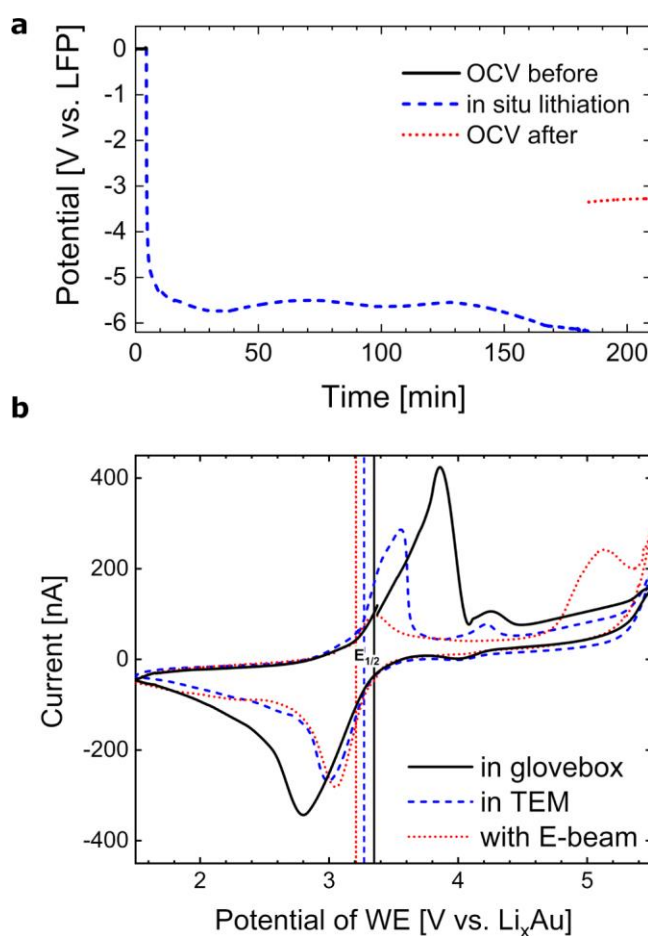


Figure 4-5: (a) Gold electrode lithiation with LiFePO_4 as the lithium source in liquid cell using CP by applying a constant current of 500 nA between the LFP counter electrode and gold electrode for 3 h followed by 30 min OCV. Dashed blue curve indicates the potential difference evolution between the lithiated gold electrode and the delithiated LFP loaded as lithium source on the counter electrode. Solid black and dotted red curves represent the OCV between them before and after lithiation respectively. (b) Cyclic voltammetry of LFP with delithiated LFP as counter electrode and lithiated gold as the reference electrode from 1.5 V to 5.5 V at 20 mV/s within the liquid cell holder in the glovebox (solid black curve), in the TEM with electron beam off (dashed blue curve) and on (dotted red curve). Electron dose rate was $42.6 \text{ e}^-/\text{nm}^2 \text{ s}$.

We note that lithiation attempts were successful only when a current above a certain threshold was applied. That is, for currents lower than 500 nA applied in the liquid cell, the gold electrode potential would quickly return to the pristine gold potential regardless of the duration of the lithiation. Furthermore, maintaining an electrolyte flow was necessary to avoid complete electrolysis of the electrolyte as the non-passivated surface area of the gold electrode used in this study is relatively large.

4.3.5. Electrochemical evaluation of lithiated gold as reference in liquid cell

To demonstrate the merit of our reference electrode for *in situ* measurements, we then used LFP particles deposited on the chip's working electrode ($E_{\text{Pt},2}$) as a model cathode material. Figure 4-5b shows three CV profiles recorded against the pre-lithiated gold reference electrode, inside the glovebox and in the TEM with and without electron beam exposure. Each measurement exhibits the classical CV shape with well-defined oxidation and reduction peaks, without the dramatic effects of the electron beam previously reported[149]. Furthermore, each measurement was well reproducible over 5 cycles. The half-wave potentials $E_{1/2}$ are measured around 3.3 V, again demonstrating that the reference electrode exhibits a potential coherent with lithiated gold, about 0.1 V vs Li/Li⁺[150], [151]. A 50 mV shift is observed between the measurements in the glovebox and the one in the TEM, possibly indicating that the former was performed before complete stabilization of the reference potential. The further shift observed between measurements without and with electron beam irradiation is due to the significant decrease in the anodic peak in the latter. Despite a relatively low electron dose rate ($42.6 \text{ e}^- \text{ nm}^{-2} \text{ s}^{-1}$), it is assumed that this decrease is associated with possible narrowing of the working potential window of the electrolyte due to increased beam-induced radicals and subsequent electrolyte degradation causing reduced ability for lithium transport[152], [153]. This is further supported by the oxidative peak appearing at 5.1 V vs Li_xAu under irradiation. It is also interesting to note that the peak-to-peak distance is significantly reduced inside the TEM, indicating reduced ohmic losses. This could be associated with an increase in the liquid layer thickness due to the membrane bulging in the microscope[109].

4.3.6. Chemical stability of the system

In addition to the air-sensitive nature of lithium-ion battery experiments, the methodology to acquire a stable lithiated reference electrode requires overcharging of the lithium source which brings in the risk of electrolyte decomposition and adds complexity to the experimental setup for the subsequent electrochemical measurements. Therefore, we used nuclear magnetic resonance (NMR) spectroscopy of the liquid electrolyte to verify the chemical stability of our system after the electrochemical processing for reference electrode preparation. Test solutions were taken after the open cell lithiation of the reference electrode as well as after the *in situ* experiments. It is noted that despite the small volume of liquid electrolyte, sampling was possible. We compared these results with fresh and ambient-air-oxidized electrolyte solutions for reference, as depicted in Figure 4-6. According to previous studies, the oxidation of LiPF_6 in LP57 mainly follows the route expressed in reactions 1 to 3[154]–[157]. Therefore, possible degradation of the electrolyte would be detected by the oxidized by-products such as PO_4^{3-} , PO_3F^{2-} and PO_2F_2^- , as shown in the air-exposed electrolyte NMR results. However, after open cell lithiation experiments with the constant volume of electrolyte or after lithiation conducted in the liquid cell with continuous flow of electrolyte, we confirm that the liquid electrolyte remains unaffected without evidence of considerable degradation of oxidative by-products and can therefore be readily used for the subsequent *in situ* electrochemical analysis.



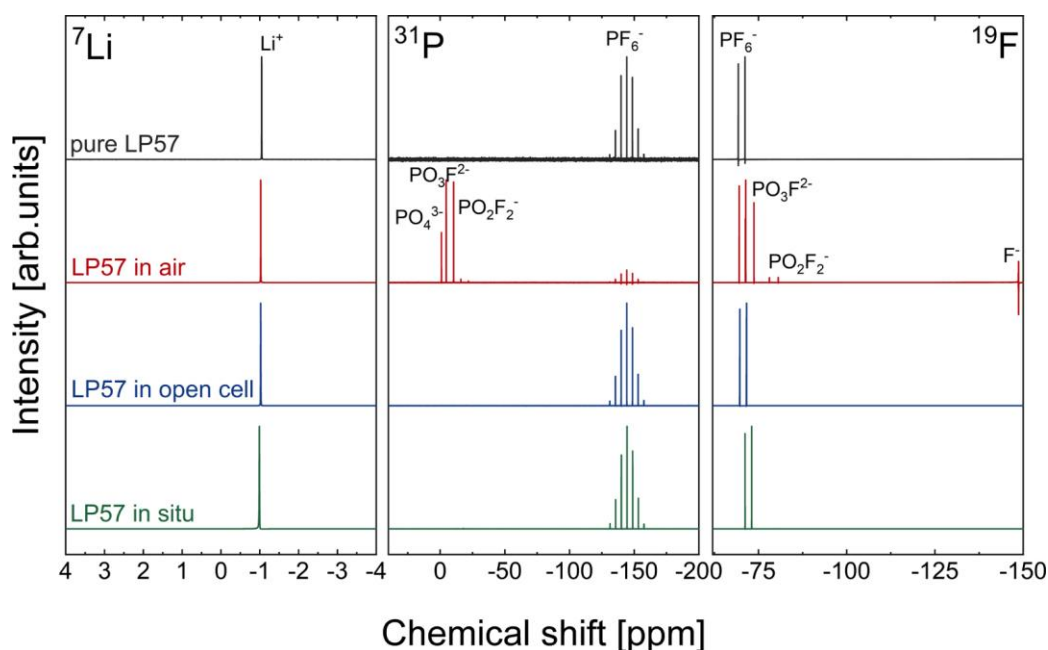


Figure 4-6: NMR spectra showing the ${}^7\text{Li}$, ${}^{31}\text{P}$ and ${}^{19}\text{F}$ of the pure electrolyte LP57 (black), LP57 exposed in air for seven days (red), LP57 collected from the open cell experiments conducted in the glovebox (blue) and LP57 collected after the *in situ* experiments within the TEM liquid cell (green).

4.4. Conclusion

In summary, using a combination of *in situ* TEM and *ex situ* chemical characterization methods, we have demonstrated a practical way of fabricating a lithium-based reference electrode for *in situ* investigations of lithium-ion batteries. Stabilizing a reference electrode for microcell testing in confined space can be achieved on the bench and within an *in situ* TEM holder by applying a constant current for steady lithiation of a gold micro-electrode without damaging the substrate and by using various sources including metallic Li, Li salt electrolyte or LiFePO_4 particles. Furthermore, the system composed of the stable potential reference electrode of Li_xAu and the partially delithiated LiFePO_4 particles on the counter electrode can be beneficial for *in situ* studies of cathode materials. Therefore, such a micro-battery setup can be optimized into a reasonable and reproducible system for more adaptable and precise characterization of real-time observations using liquid-phase electrochemical TEM.

Chapter 5: Cycling of NCM622 in the micro-battery system

The contents of this chapter are based on the published article[158]:

Charge/discharge cycling of $\text{Li}_{1+x}(\text{Ni}_{0.6}\text{Co}_{0.2}\text{Mn}_{0.2})_{1-x}\text{O}_2$ primary particles performed in a liquid microcell for transmission electron microscopy studies

Jing Hou¹, Anna Freiberg², Tzu-Hsien Shen¹, Robin Girod¹, Julien Gonthier¹, Sung-Jin Kim³, Filippo Maglia³, Hubert A. Gasteiger² and Vasiliki Tileli¹

¹Institute of Materials, École Polytechnique Fédérale de Lausanne, CH-1015 Lausanne, Switzerland

²Chair of Technical Electrochemistry, Department of Chemistry and Catalysis Research Center, Technische Universität München, D-85748 Garching, Germany

³BMW Group, Petuelring 130, 80788 München, Germany

J. Phys. Energy 2 (2020) 034007

<https://iopscience.iop.org/article/10.1088/2515-7655/ab979c>

Contribution of J.Hou: Performed sample preparation, characterization, data analysis and wrote the manuscript with contributions from all authors.

5.1. Introduction

Monitoring real-time degradation mechanisms of NCM using in situ TEM has not been possible due to the restrictions imposed by the large particle size. In addition, the system used for liquid cell observations does not emulate well the real battery system (cathode, additives, binders, electrolytes, reference electrode and anode) and no direct comparison with a standard battery setup such as a coin cell has previously been reported.

Herein, we demonstrate that battery cycling of NCM-based materials in conventional liquid TEM microcells is feasible. Specifically, the electrode configuration inside the liquid cell system was designed and optimized for the cycling of primary NCM622 particles and it was found to conform well with the expected bulk electrochemical measurements. We describe the utilization of LFP particles as non-gassing counter electrode which does not contaminate the electrolyte and which can be used as a pseudo-reference electrode. Cyclic voltammetry (CV) and galvanostatic charge/discharge electrochemical analysis were performed to evaluate the capacity decay of the cathode material during cycling. The results confirm that NCM cycling can be performed in the liquid cell over 50 cycles with reasonable coulombic efficiency and capacity retention of ~ 65%, which is realistic for such a cell.

5.2. Methods

5.2.1. Particle size modification of NCM622

$\text{Li}_{1+x}(\text{Ni}_{0.6}\text{Co}_{0.2}\text{Mn}_{0.2})_{1-x}\text{O}_2$ powder, simplified as NCM622 in the following, was provided as secondary particles (BASF, Germany). To decrease the particle size so that they fit within the restricted volume of the liquid cell and are electron transparent, a three-step wet ball milling method using N-methyl pyrrolidone (NMP, anhydrous, 99.5%, Sigma-Aldrich) as the solvent was introduced. Milling was performed using a ZrO_2 beaker with ZrO_2 beads of varying sizes with a Fritsch pulverisette 7 ball-mill (Fritsch, Germany). The milling details are summarized in table 1. The crushed powder was annealed with a ramp rate of $10\text{ }^\circ\text{C min}^{-1}$ up to $600\text{ }^\circ\text{C}$ and it was then placed on hold for 1 h before free-cooling to room temperature in order to recrystallize the particles. Specific area measurements were used to

track the size of NCM622 particles after each milling step. The specific surface area (SSA) of the particles was measured using the Brunauer–Emmett–Teller (BET) method by an Autosorb iQ nitrogen gas sorption analyzer (Quantachrome Instruments, USA). Micrographs of secondary and ball milled primary particles were also taken with a scanning electron microscope (Zeiss Merlin) for checking the morphology change after processing. Due to the increasing specific surface area of the ball-milled NCM622 particles, the proportion of binders and additives was increased to stabilize the particles that were placed onto the current collector. To perform coin cell electrochemical measurements of the crushed particles, the binders and additives were added by performing an additional ball-milling step at low rotation speed to homogeneously distribute all the materials. However, for the liquid cell experiments, the recrystallized crushed powder was simply mixed with the binders and additives, without any additional mechanical force (see section 5.3.3 for details).

Table 5-1: The procedure of three-step ball-milling of NCM622 particles.

Step	Milling balls (mm)	Material to solvent ratio by weight	Speed (rpm)	Time (min)	Rest (min)	Repeat	SSA (m ² /g)
1	10	1:1.5	400	5	15	6	N.A.
2	3	1:1.5	800	2	18	6	3.257
3	1	1:3	1000	3	17	32	14.991

5.2.2. Chip optimization for the chip-based micro-battery system

Typically, two microelectromechanical-based (MEMS) chips are used to seal the fluid for liquid cell electron microscopy studies: a top chip that is specially patterned with microelectrodes and a bottom chip that acts as a spacer that determines the thickness/volume of the liquid layer. For the battery studies herein, the top chip was microfabricated in-house with the electrodes configuration as presented in Figure 3-6a. The working electrode ($5.85 \times 10^5 \mu\text{m}^2$) was patterned on the membrane window, and the counter electrode was designed to have a larger surface area ($7.625 \times 10^5 \mu\text{m}^2$). Platinum electrodes were used as stable current collectors due to the ability of Pt to transfer electrons without any risk for corrosion of the electrode within the examined potential range during the measurements. Two-

electrodes connection was applied for electrochemical cycling of NCM cathode in this experiment. The requirements for the counter electrode concern adequate lithium hosting during NCM622 delithiation, whereas the reference electrode needs to remain stable during cycling. To this end, LFP particles were dropcast onto the counter electrode strip using a micromanipulator where they served as lithium host and as a pseudo-reference electrode. The delithiation of LFP was achieved by lithiating the blank Au electrode before cycling the NCM material (vs. LFP), where the Li_xAu alloy [137] could form without much volume expansion or thickness extension. Due to the restricted volume of the Au layer, however, we expect major portions of the lithium being deposited in its metallic state rather than as Au-Li alloy, so that a well-defined reference potential for the LFP during delithiation can be obtained. More than 50 reproducible cyclic voltammograms and galvanostatic charge/discharge cycles were achieved with this setup.

5.2.3. Electrode preparation

For the working electrode, either pristine or ball-milled NCM622 primary particles (after milling step 3) were used as cathode active material for coin cell testing. The electrode was prepared by dispersing the particles (96% wt for pristine NCM or 80% wt for ball-milled NCM), conductive carbon (Super C65, Timcal, Switzerland) (2% wt or 10% wt), and polyvinylidene fluoride binder (PVDF, Kynar HSV 900, Arkema, France) (2% wt or 10% wt) in NMP. The NCM622 slurry was mixed in a planetary mixer (Thinky, USA). The slurry of primary NCM622 particles was mixed with 10 mm ZrO_2 grinding balls in the planetary ball-mill in order to avoid the agglomeration and enhance the dispersion of components. A 30 μm 4-edge blade in an automated coater (RK PrintCoat Instruments, UK) was used for spreading the slurry on Al foil (18 μm , 99%, MTI, USA). It was dried at 50 $^\circ\text{C}$ and the final loading was 0.167 mg/cm^2 . Electrodes with a diameter of 14 mm were punched and dried overnight at 120 $^\circ\text{C}$ under dynamic vacuum in a glass oven (drying oven 585, Büchi, Switzerland) and they were then transferred to an inert gas glovebox (O_2 and H_2O < 0.1 ppm, MBraun, Germany) without exposure to ambient air. Metallic lithium discs (450 μm , 99.9%, Rockwood Lithium, USA) with 15 mm diameter were used as

counter/reference electrode in the coin cell. For the *in situ* studies, the counter/reference electrode consisted of 90% wt LiFePO₄ (LFP, Umicore) particles and 10 wt% of PVDF.

The diluted suspension (6 mg/ml) of both slurries in NMP was sonicated for 30 min prior to filtering with 1 µm pore size paper. The filtered suspension was sonicated for 10 min before dropcasting the suspensions onto the current collector strips. The suspension was then taken with a capillary (Narishige GD-C 1, Tokyo, Japan) pulled by a micropipette puller (Narishige PC-10, Tokyo, Japan), and dropcast on the selected electrode (NCM on the working and LFP on the counter electrode) using a micromanipulator (Narishige MMO-4 hydraulic micromanipulator combined with a mechanical coarse manipulator). The prepared chip was dried on a hot-plate at 60 °C in an Ar filled glovebox for 12 h to fully remove NMP without damaging the electrochemical chip.

5.2.4. Micro-battery assembly within liquid cell

Prior to assembling the chips onto the TEM holder (Hummingbird Scientific, Lacey, WA, USA) [141], both top and bottom (spacer thickness was 1 µm) chips were treated with air plasma for 90 sec at 100 W to enhance the wettability of the electrolyte with the surfaces of the three electrodes. The holder was then transferred into the glovebox for degassing. Ar gas was purged through the microfluidic tube to remove the trapped gas from the micro-cell. The holder was kept in Ar environment for 3 h before introducing the electrolyte (1 M LiPF₆ in 3:7 ethylene carbonate (EC): ethyl methyl carbonate (EMC), BASF, <20 ppm water). Wetting of the electrodes was confirmed by a stable open circuit voltage (OCV) reading on the connected potentiostat (SP-300, BioLogic, France) once the electrolyte was introduced into the liquid cell through microfluidic tubes.

5.2.5. Electrochemical measurements

The coin cell was assembled using the method described in detail previously [159], with both pristine and ball-milled NCM622 as the cathode. Both coin cells were cycled at C/5 between 3 V and 4.6 V (vs Li/Li⁺) for 10 cycles. For liquid cell measurements, the amount of electrode material loaded onto the

chip by dropcasting was difficult to quantify (roughly a few hundred pAh NCM on the working electrode). Therefore, galvanostatic charge/discharge measurements were conducted at an experimentally selected current of 50 nA between -1 V and $+1.5$ V vs. LFP (resulting in $+2.5$ V to $+5$ V vs Li/Li^+ assuming the LFP potential of roughly 3.5 V vs Li/Li^+ in this current range). Additionally, a higher upper cutoff potential was applied for galvanostatic charge/discharge compared to the potential set for cyclic voltammetry (1.4 V vs. LFP) to compensate for the high overpotential involved in the liquid cell system under constant current cycling conditions. Cyclic voltammetry (CV) with a rather fast scan rate of 20 mV s^{-1} was also performed. This accelerated ageing test method was initially chosen to facilitate the degradation observations with *in situ* characterization by TEM, which is generally limited by the experimental time[160], [161].

Before using loaded LFP as counter/reference, pre-delithiation needed to be conducted for driving the LFP into the stage of charge (SOC) where it is able to hold a stable potential over a wide range of lithiation/delithiation during cycling of the NCM working electrode [162]. The LFP loaded Pt electrode was connected as working electrode, while the blank Au was connected as counter and reference. 500 nA current was applied to initialize the delithiation of the LFP and the current was decreased step by step until the potential of LFP vs. lithiated gold started to deviate from the stable potential of delithiated LFP vs. Li/Li^+ . NCM was then connected as working electrode while delithiated LFP was connected as counter (and reference) for *in situ* cycling.

In order to measure the electrochemical performance of the cathode of the micro-battery assembled in the liquid cell, CV was firstly used to confirm the stability and reproducibility of the experiments. Then, galvanostatic charge/discharge was carried for tracking the reversibility of the reaction during cycling and the subsequent capacity decay. A low current of 50 nA was typically used for *in situ* liquid electrochemical experiments due to the otherwise too large ohmic losses of the setup. Additionally, as relatively longer cycling time was consumed for one cycle while applying such a low constant current, this is considered as a milder way of cathode cycling compared to CV and therefore the mass transport of lithium ions of electrolyte could be well regulated under these conditions.

5.2.6. Post mortem electron microscopy

After cycling in the liquid cell holder, the chip was unmounted and rinsed with dimethyl carbonate (DMC) to remove the electrolyte residues. The chip was kept sealed within an Ar filled vial during the transfer between the glovebox and the microscopes. A ThermoFisher Scientific Talos F200X TEM operated at 200 kV was used to examine the top chip. Scanning TEM (STEM) and energy dispersive spectroscopy (EDS) were used to identify structural and compositional changes, respectively, after the electrochemical operation. The loading time was kept short to minimize exposure of the samples to air.

5.3. Results and discussion

5.3.1. Bulk electrochemical response of ball-milled primary particles

The average size of the secondary NCM particles is in the micrometer scale (Fig. 5-1a), which makes it impossible to load in the liquid cell for electron microscopy studies. Therefore, a procedure for retrieving the primary particles from the secondary particles was introduced. A three-step ball-milling method was undertaken to produce particle sizes of 200–300 nm (Fig. 5-1b), which was followed by annealing to recrystallize the particles. To confirm the electrochemical performance of the ball-milled particles as cathode electrodes, coin cell cycling of the secondary and ball-milled particles was first performed. Figure 5-1c depicts the differential capacity of the ball-milled and pristine particles as a function of the working electrode voltage vs. Li/Li⁺. The good alignment of the differential capacity peaks for both materials indicates that the same redox reactions during cycling take place at 3.7–3.8 V vs. Li/Li⁺. Compared to the pristine NCM622 (Fig. 5-1d) the initial specific capacity of the ball-milled NCM622 sample (Fig. 5-1e) has decreased by 40% (i.e. drop from 200 mAh/g to 120 mAh/g). This capacity loss of the ball-milled NCM622 could be linked to the interaction between the surface of the electrode material with the electrolyte as a result of the ≈ 50 -fold larger exposed surface area of the ball-milled NCM622 particles (from 0.3 m²/g in the case of the pristine NCM622 to 15 m²/g for the ball-milled material). In addition, the capacity loss of the crushed particles for the coin cell measurements could be due to possible structural damage during the slurry preparation with the participation of

grinding balls. The layered structure of the crushed particles after annealing was confirmed by high resolution TEM (HRTEM) in Figure 5-1f, where the periodicity of the fringes matches the spacing of the layers 0.47 nm [163] and the fast Fourier transform (FFT) (Fig. 5-1h) on the edge of the particle is consistent with $R\bar{3}m$ rhombohedral crystal structure from $[1\ 1\ 0]$ zone axis. In contrast, HRTEM and the corresponding FFT on the selective regions of grinded particles after slurry preparation for coin cell measurements (Fig. 5-1g) shows that the structure is damaged and is partially transformed into spinel ($Fd\bar{3}m$) close to the surface of the particle. However, it is noted that this final preparation step was specifically performed for coin cell measurements and it was not involved in the electrode suspension preparation for dropcasting on the electrochemical chip for *in situ* TEM. Therefore, the electrochemical measurements of the ball-milled NCM622 particles used as working electrode for the experiments with the *in situ* TEM cell are expected to represent well the properties of the pristine NCM622 material making the electrochemical measurements with the two different cell setups comparable.

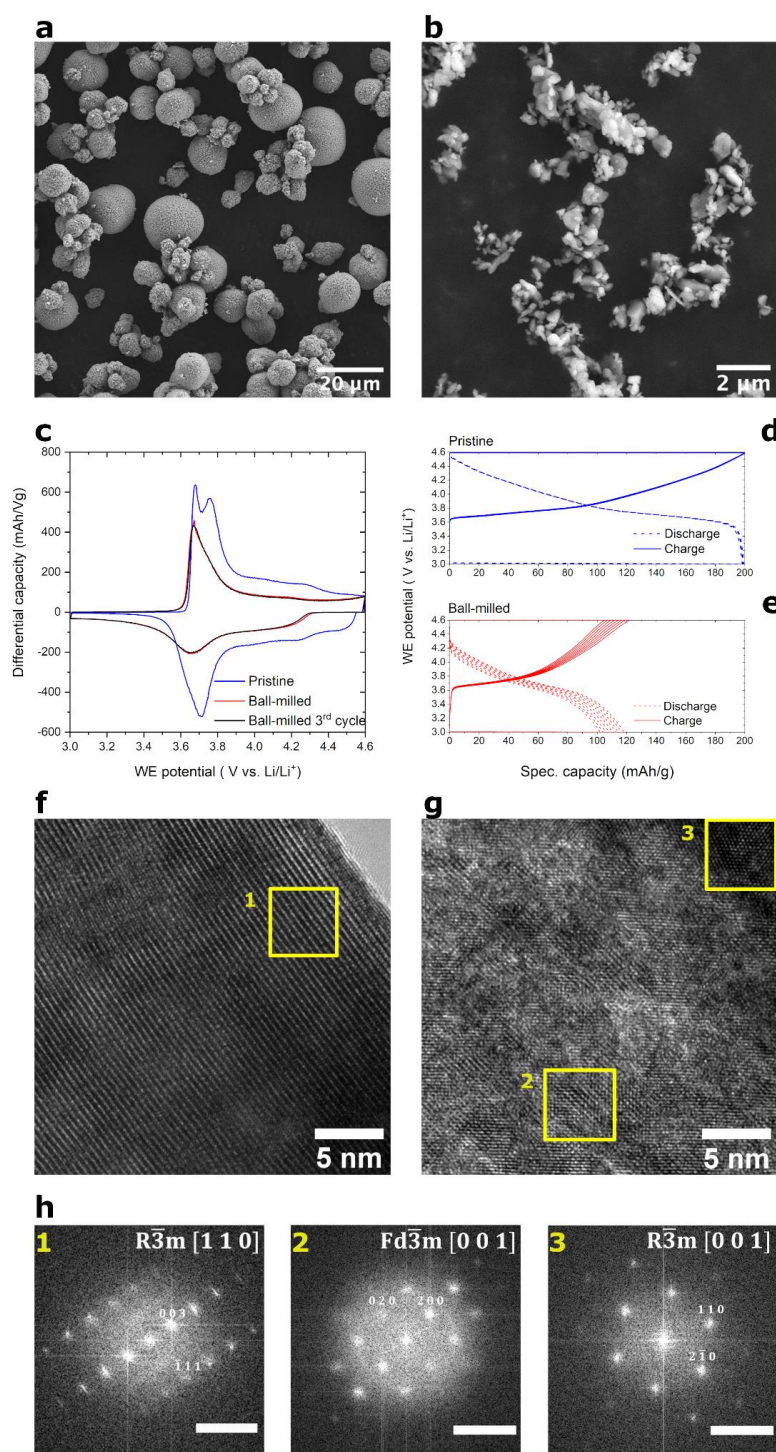


Figure 5-1: SEM micrographs of the pristine (a) and the ball-milled (b) NCM622 particles, respectively. The following electrochemical performance characteristics of the pristine and of the ball-milled NCM622 particles obtained in conventional coin cells are shown in the following: (c) Differential capacity vs. potential plot for the pristine NCM622 (blue) and the ball-milled NCM622 first (red) and third (black) cycle for a C/5 charge/discharge between 3 V and 4.6 V vs. Li/Li^+ . Working electrode potential vs. specific NCM622 capacity for 10 galvanostatic charge/discharge cycles between 3-4.6 V for pristine NCM622 (d) and for the ball-milled NCM622 particles (e). (f) HRTEM micrograph of the annealed particles. (g) HRTEM micrograph of the primary particles after grinding assisted slurry preparation. (h) FFT of regions indicated as yellow squares in (f) & (g) with corresponding number. The scale bar is 5 nm^{-1} .

5.3.2. Electrochemical response of ball-milled primary particles on the electrochemical chip

The cycling performance of ball-milled NCM particles was first tested in the confined electrochemical configuration of the liquid cell. The SEM images in Figure 5-2a&b indicate the microfabricated coplanar electrode geometry of the top electrochemical chip. The geometry of the working and counter electrodes allows to site-specifically deposit the ball-milled NCM622 particles and LiFePO_4 nanoparticles on the respective electrodes. After control experiments, a two-electrode configuration was found to provide interpretable electrochemical profiles, hence the third electrode, normally used as a reference, was left unloaded. Prior to the cycling experiments of the NCM622 particles, the LFP particles were pre-delithiated by electrochemically transferring the lithium ions onto the Au reference electrode strip of the cell (labeled RE in Fig. 5-2a). This preparation of the counter electrode serves to utilize it as simultaneous pseudo-reference electrode (i.e. as electrode which retains an essentially constant potential so that its potential serves as pseudo-reference potential). To initiate the nucleation of metallic lithium on the Au reference electrode strip during delithiation of the LFP, a current of 500 nA was firstly applied and then reduced step-wise until the stable potential plateau of LFP was observed, as shown in Figure 5-2c. The potential reading between the partially delithiated LFP and the lithiated Au stabilized at the value closer to the theoretical value of delithiated LFP vs. Li_xAu alloy (3.5 V) while applying lower current densities (from 500 nA down to 5 nA). After this partial delithiation of the LFP deposited on the counter electrode strip, galvanostatic charge/discharge cycling was performed in the liquid cell inside the glovebox to confirm the electrochemical performance of the system. Cycling with a constant current of 50 nA shows reasonable electrochemical performance of the ball-milled NCM622 particles (Fig. 5-2d). Interestingly, the coulombic efficiency of this setup is close to 100% after a few cycles, which indicates good reversibility of the charge/discharge reaction in the liquid cell configuration, reasonably close to the expected behavior for a conventional cell setup. Moreover, the initial discharge capacity and the capacity fading of the ball-milled NCM622 particles obtained in the liquid cell setup was found to be quite comparable with the corresponding values obtained in the coin cell configuration (see Fig. 5-1e), having around 80% capacity remaining after 10 cycles.

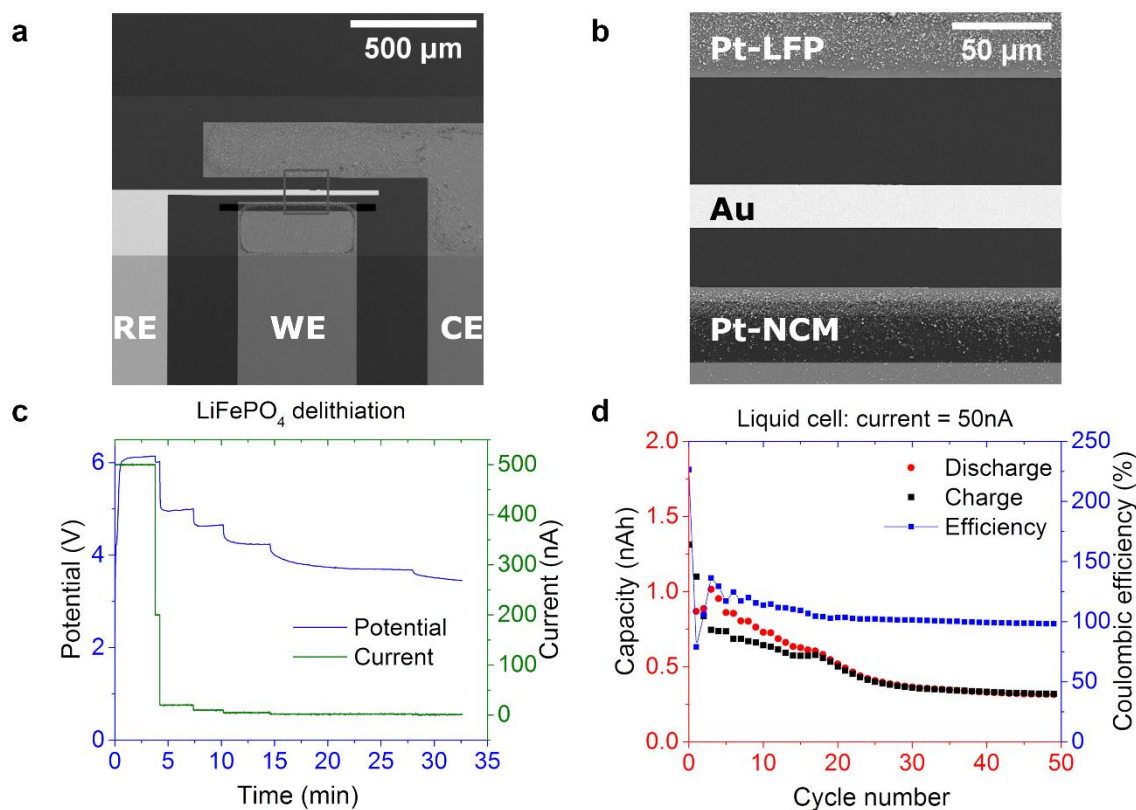


Figure 5-2: (a) SEM images of the electrochemical chip patterned with electrodes made from one Au electrode strip (labeled as RE) and two Pt electrode strips (labeled as WE and CE). (b) Zoom-in of the grey square region in (a), the Pt WE electrode covering the electron transparent area was loaded with ball-milled NCM622. The Pt CE electrode with the largest surface area was loaded with LFP. (c) Partial delithiation of LFP by applying a constant anodic current with step-wise reduced magnitude between the CE and RE strips. The potential (blue) stabilized at different values at the different values of the applied current (green). (d) Charge (black) and discharge (red) capacity of NCM622 over 50 galvanostatically controlled charge/discharge cycles conducted in the liquid-cell setup between 1.5V and -1V (vs. partially delithiated LFP) at a current of ± 50 nA; the blue symbols show the corresponding coulombic efficiencies.

5.3.3. Cycling of ball-milled particles with varying electrochemical input in a liquid microcell TEM holder and post mortem TEM analysis

Local chemical transformations of the ball-milled particles were evaluated *in situ* by applying a range of electrochemical conditions. The electrochemical stimuli performed in the liquid cell TEM holder and the post mortem STEM-EDS analysis of the NCM particles participating in the reactions are displayed in Figure 5-3. The particles' response to cyclic voltammetry was first investigated (Fig. 5-3a). Compared

to reported CV curves from coin cell experiments, broadening of the redox peak in the CV within the liquid cell is seen. This is attributed to geometric differences between the two configurations. It is known that the liquid TEM cell causes deviations from the ideal Nernstian behavior and exhibits increased ohmic drop [109], [152], [164], [165]. Moreover, geometry dependent mass transport and diffusion variation in the microband/microfluidic system will impact the electrochemical measurement and also result in peak broadening [166]. The particles did not exhibit significant compositional modification after 5 cycles and the structure remained intact, as revealed by the atomic ratio of Ni, Co and Mn that remained at 3:1:1 over the whole particle (Fig. 5-3b&c). Typically, the high scan speed during CV analysis does not provide sufficient time for lithium ion transport towards the electrode. Such CV conditions are inadequately used in liquid cell TEM testing of battery systems and cannot be directly compared to galvanostatic battery cycling. Next, charge/discharge measurements were performed. Particles mapped in Figure 5-3e were cycled 50 times with a constant current of 50 nA with one hour rest every 10 cycles (Fig. 5-3d). They exhibit Mn and Co dissolution up to 20 nm from the surface as indicated by the arrow in the line profile of atomic fraction in Figure 5-3f. The dissolution of Mn and Co ions from the NCM particles after cycling is caused by the ionic disorder that takes place along with the de-/intercalation process consisting of ionic diffusion within the electrolyte and solid-state diffusion of lithium atoms within the electrode material [167], [168]. The pause introduced between the cycles ceases the polarization via minimization of the adsorbed ions on the surface of the electrode, which is reflected in the observed bounce back and destabilization of the charge capacity from the first cycle after each pause, as depicted in Figure 5-3d. Suspending the polarization on the electrode not only triggers the relaxation of ions within the double layer by electrolyte ionic concentration gradient redistribution but also assists on the rearrangement of the lithium atoms through solid-state diffusion within the NCM particles. As reported previously, the ionic radius of Ni^{2+} (0.69 Å) is similar to Li^+ (0.76 Å) and has lower diffusion barrier, making it more feasible for Ni/Li exchange and Ni rearranging within the NCM material while the Mn and Co ions tend to undergo irreversible chemical reaction with the liquid electrolyte that, together with the electrochemical redox, leads to their

dissolution from the surface of the particles after cycling [169], [170]. The rest between several cycles provides the opportunity for element relaxation from the disordering induced by the lithium de-/intercalation during charge and discharge cycling and it should serve as the means to perform reproducible battery cycling experiments using liquid-phase electron microscopy.

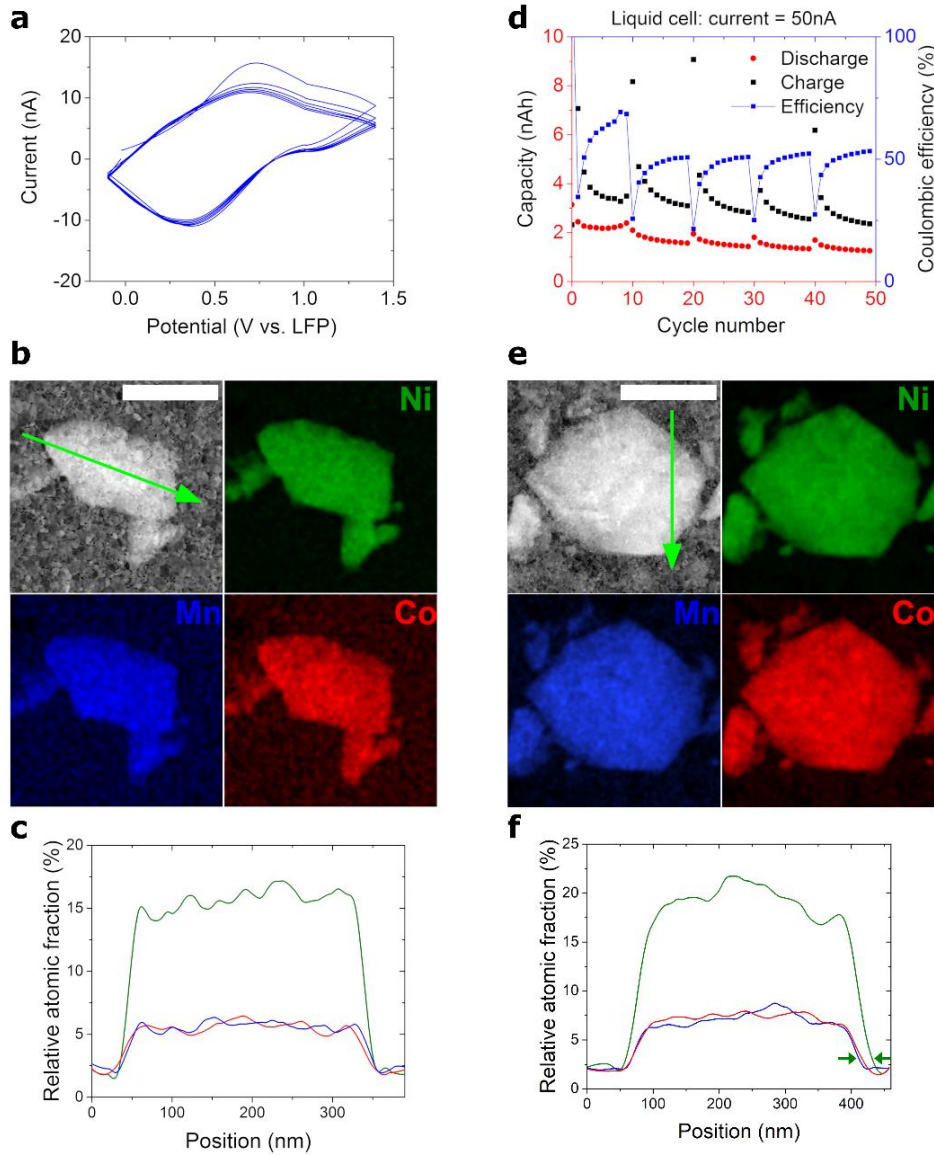


Figure 5-3: (a-c) CV-based analysis: a is the CV curve for cycling NCM particles inside the liquid cell at 20 mV/s for 5 cycles. (b) shows the HAADF image of a particle after cycling and the EDS elemental maps for Ni (green), Mn (blue) and Co (red). (c) depicts an EDS line profile across the particle (green arrow in HAADF image) that demonstrates the distribution of the three transition metals. (d-f) Galvanostatic charge/discharge analysis: d shows the capacity profiles for cycling at 50 nA for 50 cycles with 1 h rest between every 10 cycles. Plotted in the same figure is the measured coulombic efficiency. (e) shows the HAADF image and EDS elemental maps of a particle after 50 cycles. f is an EDS line profile across the particles along the green arrow displayed in the HAADF image in (d). The subtle elemental dissolution of Co and Mn is depicted with arrows in (f). The scale bar is 200nm in both HAADF images.

5.4. Conclusion

In summary, a versatile setup for micro-battery TEM experiments in liquid electrolytes was assembled and it was found practical for a range of electrochemical measurements pertinent to lithium-ion battery testing. The electrochemical performance of ball-milled NCM622 primary particles was shown to be representative of the secondary ones that are commonly used in bulk systems. Therefore, the mass transfer limitation and internal resistance caused by the relatively smaller volume of the electrolyte and the restrictions imposed by the quantity of the electrode active material that can be loaded on the microelectrodes do not inhibit the experimental measurements. However, the electrochemical measurements revealed that the geometry-related limitations of the *in situ* TEM setup can affect the lithium de-/intercalation within the Ni-rich layered oxide cathodes which drive the migration of transition metal ions. In this study, we showed that by adding pause conditions during galvanostatic charge/discharge cycling, the micro-system's electrochemical behavior leads to cathode degradation mechanisms comparable to the expected ones in bulk cells. Thus, with the methodology developed herein, we are now close to monitoring in real-time the complex degradation processes involved in the positive electrodes of lithium-ion batteries and directly relate them with the electrochemical conditions applied for their ageing.

**Chapter 6: Electrochemical and structural
 evolution of NCM622 and
 NCM811 in micro-batteries**

6.1. Introduction

Layered oxide cathodes of the general formula $\text{Li}[\text{Ni}_{1-x-y}\text{Co}_x\text{Mn}_y]\text{O}_2$ (NCM) have been developed with growing Ni-content due to their higher energy density that can be obtained for a given upper cut-off potential by extracting more lithium from the layered NCM structure[171]. A structure with more increased Ni content from NCM622 is the 811 (0.8Ni, 0.1Co, 0.1Mn). This exhibits higher theoretical electrochemical performance and it is also less sensitive to the change of cobalt prices that is a vital concern in the battery cost[172]. Considering that the transition metal ions have strong influence on the intrinsic properties of NCM materials, the relationships between the composition evolution and the electrochemical performance that fade in the layered lithium transition metal oxides need to be systematically studied.

Herein, we demonstrate the comparative cycling of cathode materials with two concentration ratios of transition metal ions NCM622 and NCM811 in our optimized liquid TEM microcells. Galvanostatic charge/discharge electrochemical analysis was performed to evaluate cathode cycling in both macro and microsystems. This accelerated aging test method was initially chosen to facilitate the degradation observations with *in situ* characterization by TEM, which is generally limited by the experimental time[160], [161], [173]. The results confirm that the electrochemical cycling of primary NCM622 and NCM811 primary particles in the liquid cell can provide comparative coulombic efficiency and capacity retention to the conventional secondary particle-based coin cell tests. Thus, the cycling stability of the particles is investigated in the liquid cell by running accelerated cell aging tests. The transition metal ion dissolution aging mechanism was studied by *ex situ* STEM EDS. The phase separation was observed in NCM622 with Ni and Co rich patches. However, NCM811 shows less stability over the same cycling condition and it is mainly affected by the surface interaction with the electrolyte.

6.2. Methods

6.2.1. Material processing and electrode preparation

$\text{Li}_{1+x}(\text{Ni}_{0.6}\text{Co}_{0.2}\text{Mn}_{0.2})_{1-x}\text{O}_2$ (NCM622) and $\text{Li}_{1+x}(\text{Ni}_{0.8}\text{Co}_{0.1}\text{Mn}_{0.1})_{1-x}\text{O}_2$ (NCM811) were provided as secondary particles with the size of around 10 μm (BASF, Germany). The hierarchically structured particles were processed by three-step wet ball milling (as being described in section 5.3.1) into primary particles with the size of 200-300 nm. The ball-milled NCM622 and NCM811 primary particles (after milling step 3) were used as active cathode material for coin cell and liquid cell testing.

The primary-particle-based electrode slurry for coin cell and micro cell test was prepared following the procedures explained in section 5.3.3. The loading of active materials of NCM622 and NCM811 electrodes in the coin cell was 0.296 mg/cm^2 and 0.25 mg/cm^2 , respectively. Coin cell testing was carried out on a half-cell that was assembled with metallic lithium as the counter/reference electrode, while delithiated LiFePO_4 was used as the counter/reference electrode in the two-electrodes connection for micro cell testing.

6.2.2. Battery assembly

6.2.2.1. Coin cell

A reliable electrochemical setup is essential to evaluate the basic properties of batteries. Half-cell configurations with two electrodes are typically applied, in which electrode active materials to be evaluated is used as the working electrode (WE). In contrast, the other electrode is used as the counter (CE) and the reference (RE) electrode[174]. Electrochemical cycling of NCM/Li coin cell was assembled in an Ar filled glove box with NCM as the working electrode and lithium as the counter electrode. The two electrodes were assembled face to face with two glass fiber separators (glass microfiber filter, 691, VWR, Germany) with an equal diameter in between. Cells were assembled with 80 μl of LP57 electrolyte soaked in the separator between working and counter electrode. Stainless-steel current collectors and a spring were placed on maintaining pressure on the electrode stack, while

the electrical insulation and airtightness were ensured by the polypropylene gasket. The tight sealing was accomplished by a specific crimping machine, making the setup ready for long-term cycling at a lab scale.

6.2.2.2. Open cell

The reliability of the chip is evaluated by micro-battery system with primary particles as electrodes. The loaded electrochemical top chip was clamped onto a specially designed planar casing that was connected to the external potentiostat. Then, 100 μl of electrolyte was dropped to cover all electrodes and therefore allowing for ion transport between them and for running electrochemical measurements. Both the assembly of open cell and the electrochemical experiments were conducted in the Ar filled glovebox.

6.2.2.3. Liquid cell

The electrochemical chip with symmetric electrode configuration as presented in Figure 3-7b are assembled with a 1 μm spacer after both been treated with air plasma for enhancing wettability following the method described in section 5.3.4. The system stabilization of the liquid cell after introducing the electrolyte through a microfluidic tube is confirmed by the stable open circuit voltage (OCV) reading on the connected potentiostat.

6.2.3. Electrochemical measurements

Coin cells were cycled at C/5 between 3 V and 4.6 V vs. Li/Li⁺ for 5 cycles. The C-rate was referenced to the approximate theoretical specific capacity of the NCM622 (220 mAh/g) and NCM811 (275 mAh/g) at 1 C (equating to areal capacities of 0.065 mAh/cm² for NCM622 and 0.069 mAh/cm² for NCM811). The cells were cycled in a 25 °C climate chamber (Binder, Germany) with a battery cycler (Series 4000, Maccor, USA). For micro cell measurements, the amount of electrode material loaded onto the chip by dropcasting was difficult to quantify (roughly a few hundred pAh NCM on the working electrode).

Therefore, galvanostatic charge/discharge measurements were conducted at an experimentally selected current of 10 nA on the micro cell between 2 V and 5.5 V for 50 cycles, 1 h rest was introduced between every 10 cycles. Here, the potential values were calculated vs. Li/Li^+ , which was determined by considering a stable LFP potential of 3.5 V vs. Li/Li^+ . Because of the remarkable overpotential involved in the liquid cell system, 100 nA was requested for cycling primary NCM particles in the liquid cell.

6.2.4. Post mortem electron microscopy

After cycling in the liquid cell holder, the chip was unmounted in the Ar-filled glovebox and rinsed with dimethyl carbonate (DMC) to remove the electrolyte residues. The harvest chip was kept sealed within an Ar filled vial during the transfer between the glovebox and the microscopes. The loading time was kept short to minimize exposure of the samples to air. A ThermoFisher Scientific Talos F200X TEM operated at 200 kV was used to examine the top chip. Scanning TEM (STEM) and energy dispersive spectroscopy (EDS) were used to identify structural and compositional changes, respectively, after the electrochemical operation.

6.3. Results and discussion

6.3.1. Electrochemical measurements of the two Ni-rich cathodes on coin and micro open cell configurations

First, the cycling capability of cathode primary particles on the coin cell and chip-based microcell setup is compared. An overall higher overpotential in the chip-based microcell setup is measured. This is attributed to the considerably large distance between the coplanar microelectrodes which results in a larger ohmic drop within the electrolyte. Additionally, limited electrode reaction sites due to the small quantity of active electrode materials that are loaded on the electrochemical chip as well as the consequent high current density may end up with insufficient ion migration for electron neutralization on the electrode surface leading to higher diffusion overpotential in the system (charge transfer limitation). Such kinetic inhibition on the electrode reaction requires higher overpotential[175].

Therefore, an extensive range of cycling potentials was applied for galvanostatic charge/discharge in open cell (2 V to 5.5 V vs. Li/Li⁺) than the potential set for coin cell tests (3 V to 4.6 V vs. Li/Li⁺). As presented in Figure 6-1a-d, instead of holding the overall capacity of more than 80% in coin cell, the NCM particles have less than 50% capacity left in the open cell after the first 5 cycles. The unexpected large capacity measured from the primary particle of NCM811 (Fig. 6-1b) is a hint for significant parasite reactions taking place with the electrolyte while cycling. Although the practical discharge capacity of NCM811 (161 pAh) is higher than that of NCM622 (134 pAh) under the same cycling condition, NCM811 is less stable compared to NCM622 when cycling in the open cell. Only 40% capacity retention is observed for NCM811, while NCM622 holds 60% of the initial capacity after 50 cycles. The fast decay of NCM particles observed in the open cell system is expected due to the high current rate[176]. In the galvanostatic charge/discharge open cell measurements, the operational current is dependent on the experimental setup and the active material loading is hard to estimate, however, the current rate can be calibrated by the average time used for completing the cycles. The C rate was calculated to be around 780 C for NCM622 and 310 C for NCM811. Such accelerating cycling condition is crucial for *in situ* study with TEM, where efficient stimulation of the degradation in cathode materials can bring more chances of capturing the electrochemically induced modification. However, the high current condition may, on the other hand, interrupt the stabilization of the open cell system. As shown in Figure 6-1e&f, the differential capacity during galvanostatic charge/discharge has peaks overlapping from most of the cycles. For the first ones, indicated as red curves in Figure 6-1e&f and highlighted in red boxes in galvanostatic graphs in Figure 6-1c&d, the dQ/dV curves are shifted, indicating the reactions taking place initially between electrode and electrolyte for stabilizing the system. Interestingly, despite the electrode loading on the electrochemical chip being two orders of magnitude smaller than for the coin cell, the micro-battery system based on separately loaded electrode particles takes more cycles to stabilize, which is attributed to the fully exposed electrode material surface area boosting the chance for the interface reaction between electrode and electrolyte.

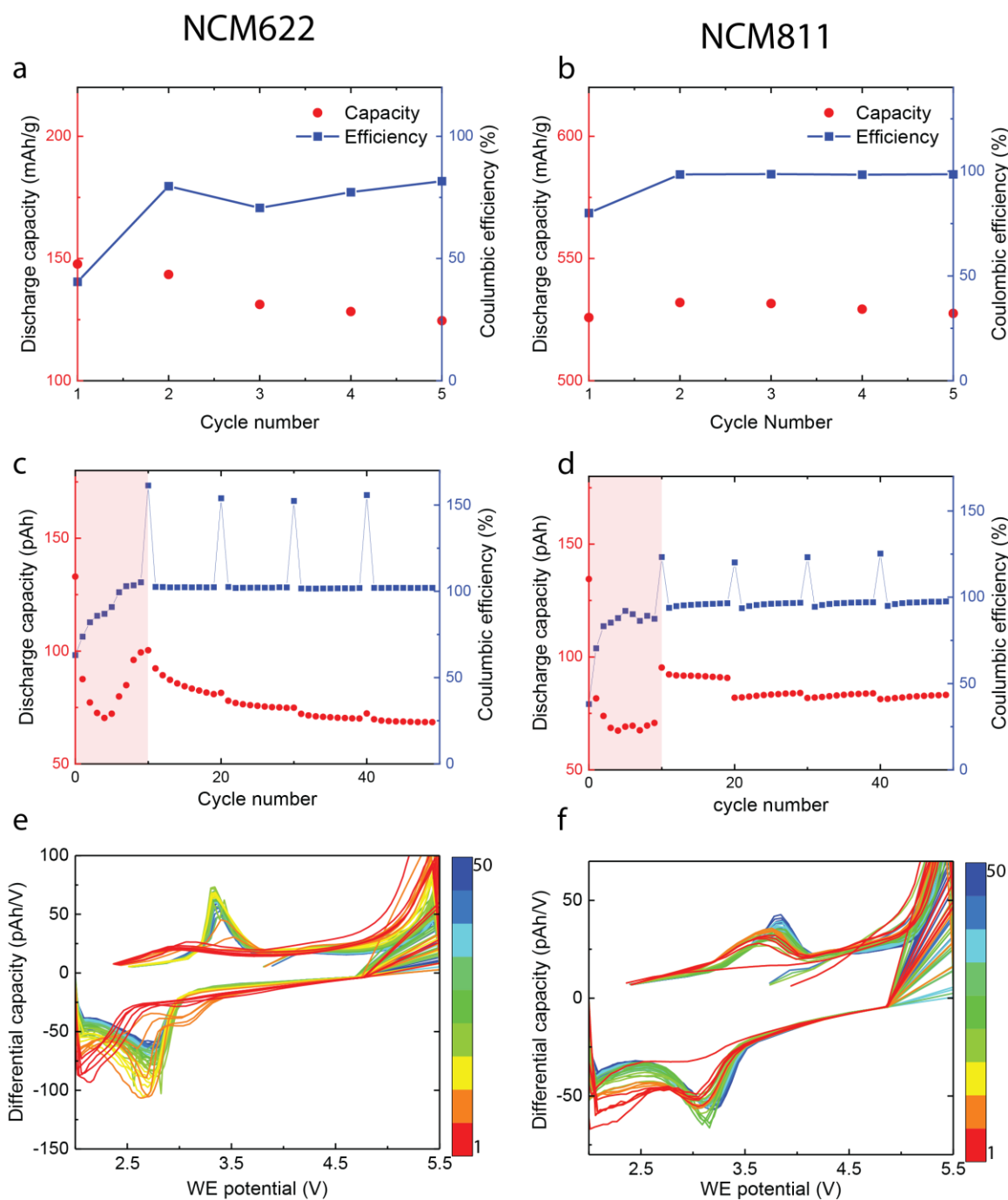


Figure 6-1: Coin cell galvanostatic charge/discharge of NCM622 (a) and NCM811 (b) primary particles between 3 V to 4.6 V (vs. Li/Li⁺) at C/5 for 5 cycles. Galvanostatic charge/discharge of NCM622 (c) and NCM811 (d) primary particles on electrochemical based micro cell between 2 V to 5.5 V (vs. Li/Li⁺) at 10 nA for 50 cycles with 1 h rest between every 10 cycles. Red boxes indicate the cycles for stabilizing the micro battery system. (e-f) Differential capacity from galvanostatic charge/discharge of NCM622 (c) and NCM811(d) from 1st (red) to 50th (blue) cycle.

6.3.2. Chemical evolution of particles cycled in the liquid cell

The local compositional modification of the primary NCM particles after electrochemical stimuli performed in the liquid cell TEM holder is evaluated by the post mortem STEM-EDS. A two-phase separation within the particle was observed from the NCM622 particle mapped in Figure 6-2, which was cycled 100 times with a constant current of 100 nA with 10min rest every 10 cycles. The coulombic efficiency dropped from 90% to 80% after 100cycles with the capacity retention decreases during the first 30cycles by 60%, but increasing subsequently. Rather than continuous concentration variation as reported for particles cycled with longer resting time[177], there is a sharp boundary between the Ni-rich and Co-rich phase domains, which can be seen from the EDS composition of the selected region and line profile in Figure 6-2c&d. Even though Mn does not vary as much as the other two transition metals across the particles, the overall composition of the whole particles indicates slight Co and Mn deficiency. This local various compositional modification caused by shorter rest time is assumed to result from solid-state diffusion together with the charge-transfer kinetically controlled lithium intercalation. The high current rate may have driven the redox reaction of both Li and transition metals, while there is not sufficient time either for Li diffusion-limited reactions on the electrode or for elements relaxing from the disordering induced by the lithium dis/intercalation during charge and discharge. The tendency of Ni^{2+} (0.69 Å) ions substituting Li^+ (0.76 Å) ion in octahedral sites (cationic disorder) can drive the Ni^{2+} ion migration during delithiation, especially for the ones occupying the 3a site of Li-layer. Meanwhile, Ni^{2+} ions and the oxidized Ni^{3+} ions that are formed during delithiation are preferentially utilized for facilitating faster lithium diffusion due to the lower activation barrier[170]. Thus, the irreversible Ni migration is hypothesized to be the reason for developing the Ni-rich region. Moreover, the irreversible chemical reaction between Mn and Co ions with the electrolyte is accompanied by oxygen release under high upper cutoff potential, which can lead to elemental rearranging within the NCM materials during cycling for charge neutralization and potential Mn dissolution as has been previously reported[170], [178]–[180]. The lattice distortion due to the transition metal migration and phase separation can lead to bulk phase transformation and capacity decay. However, no surface

modification was observed from the cycled particle. The only bulky phase attaching to the particle that is rich in O and F (Fig. 6-2 h-i) is expected from the electrolyte residue on the chip after processing.

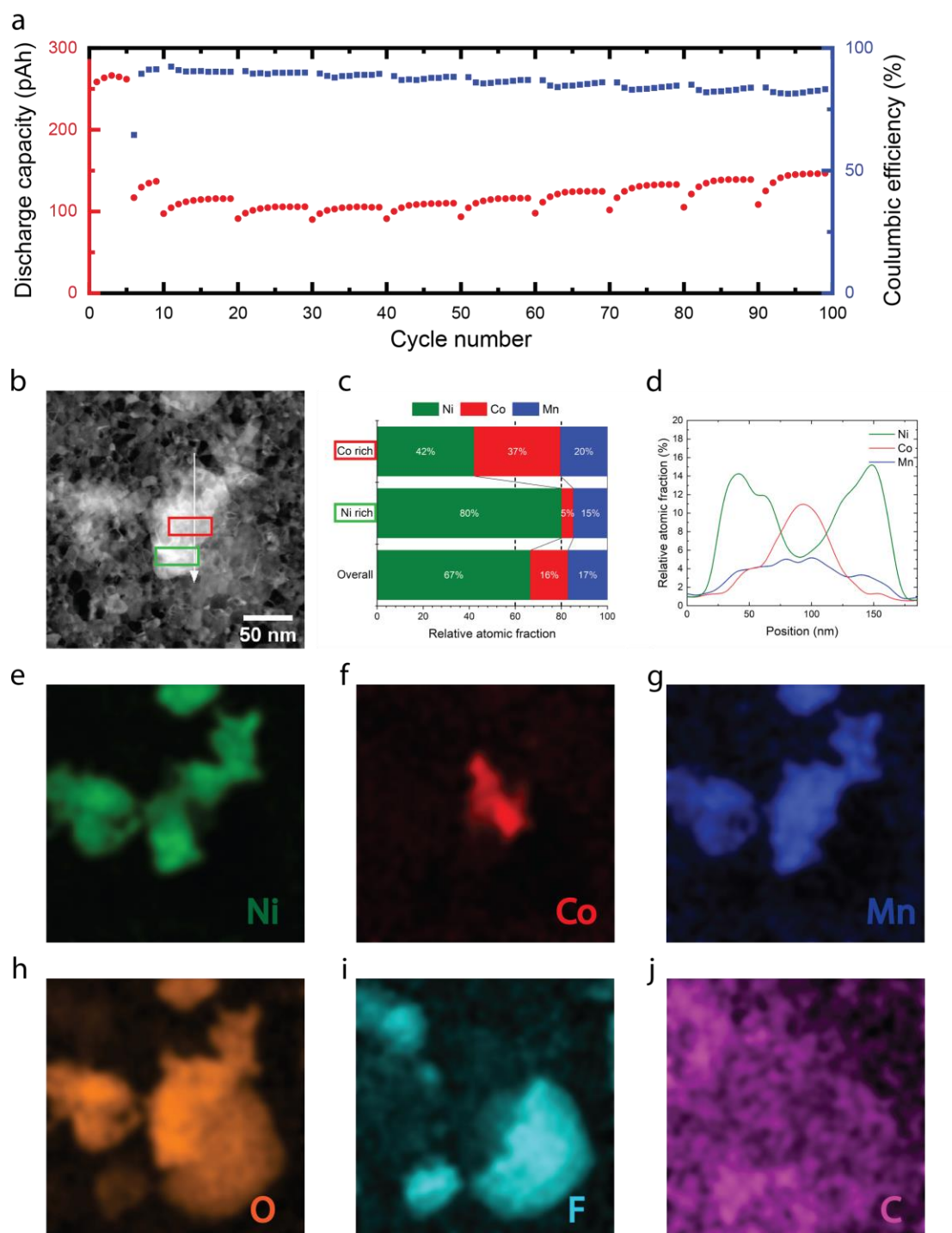


Figure 6-2: (a) presents capacity (red dots) and coulombic efficiency (blue squares) profiles of galvanostatic charge/discharge at 100 nA between 2.7 V - 5.5 V (vs. Li/Li⁺) for 100 cycles with 10 min rest between every 10 cycles. (b) shows the HAADF image of an NCM622 particle after cycling. (c) illustrates the relative atomic fraction of transition metals in the selective regions in (b) (red box indicates the Co rich region and the green box

indicates the Ni-rich area). The vertical dash lines indicate the theoretical composition of the particle. (d) depicts an EDS line profile across the particle (white arrow in HAADF image) that demonstrates the distribution of the three transition metals. (e-j) EDS elemental maps for Ni (green), Co (red), Mn (blue), O (orange), F (turquoise), and C (purple).

The micro battery cycling in the liquid cell with NCM811 at the same voltage range as for NCM622 remains operational for only 30 cycles. The coulombic efficiency (CE), serving as an indicator for quantifying the magnitude of side reactions and the reversibility of the cycling is used for estimating the health state of a battery and provide estimation on the battery degradation[181], [182]. Therefore, the dramatic decrease of the CE of NCM811 from 86% to 56%, as depicted in Figure 6-3a, indicates that the micro battery has reached the end of its life by then. The abnormal capacity increase during efficiency drop can be a reason of the surface reaction induced by the high upper cutoff potential for cycling NCM811. The elemental characterization of NCM811 harvested from this cycled micro battery is presented in Figure 6-3b-j. Instead of the phase separation with a distinct phase boundary as in NCM622, the NCM811 does not shows compositional variation over the entire particle (Fig. 6-3c, e-g). However, the subtle Co and Mn dissolution up to 10nm from the surface of the particle can be identified through the line profile of the atomic fraction of the transition metal ions along the particle (Figure 6-3d). The dissolution of Mn and Co ions from the NCM particles after cycling is caused by the ionic diffusion and solid-state diffusion induced ionic disorder within the electrode material[169], [170]. Even though the rest time was shorter and the applied current was higher, the NCM811 shows similar compositional evolution to the NCM622 cycling in the liquid cell with the same coulombic drop[177]. Thus, the irreversible de/intercalation of Li^+ without much compositional degradation in NCM811 after cycling suggest that its degradation is more related to the interface reaction between electrode and electrolyte rather than structural or chemical transformation within the electrode particle. From the previous studies using density functional theory calculations as well as in situ Raman spectroscopy, increasing Ni content in the positive electrode materials has been found to promote the dehydrogenation of carbonate-based electrolytes, leading electrode impedance growth[183], [184]. Such interface normally consists of inorganic constituents (Li_2O , LiF and Li_2CO_3), and the organic

constituents (ROCO_2Li and ROLi) [185], which is coherent with the F and C-rich shell forming on the surface of NCM811 particles after cycling as can be seen from Figure 6-3h-i.

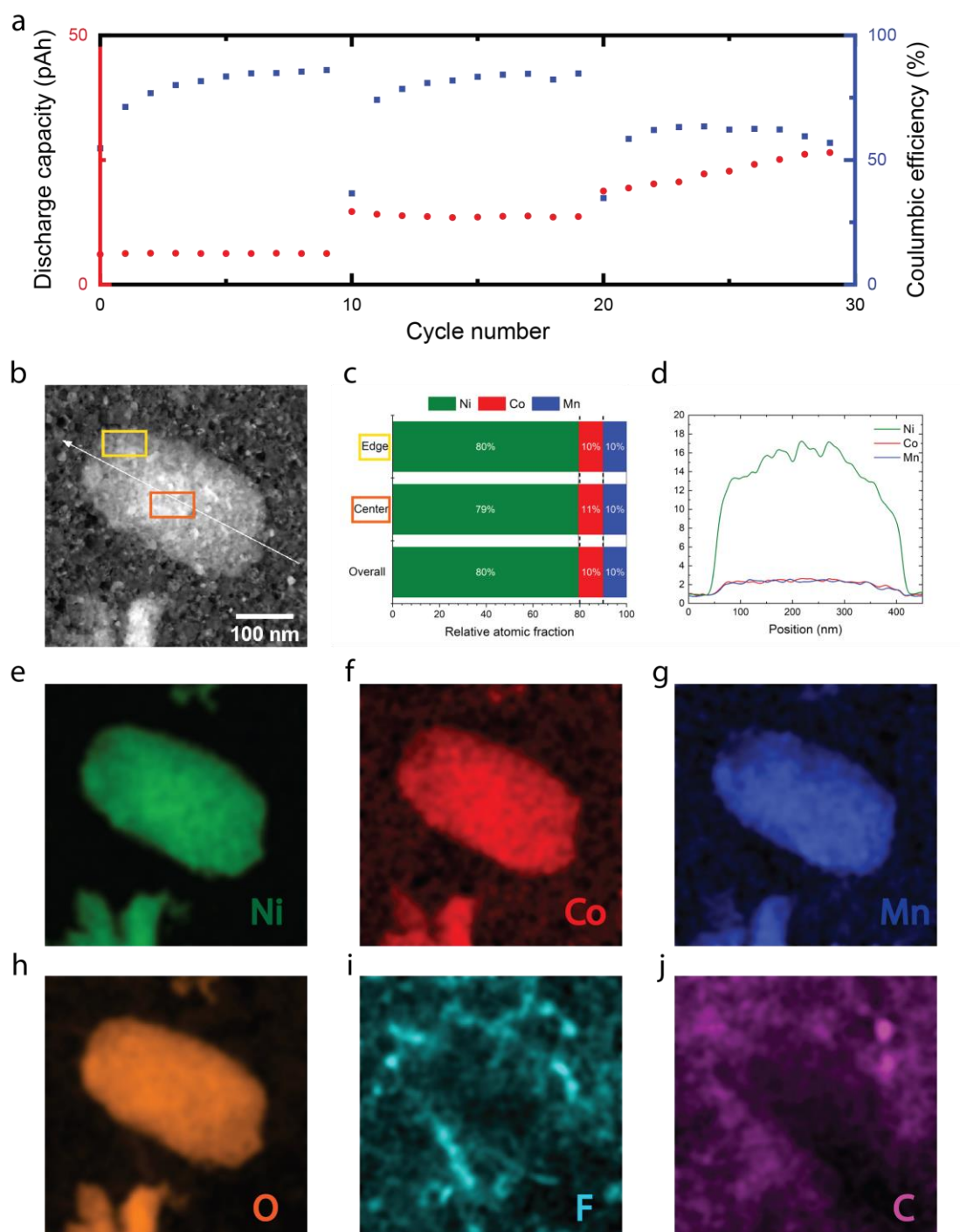


Figure 6-3: (a) present the capacity (red dots) and coulombic efficiency (blue squares) profiles of galvanostatic charge/discharge NCM811 at 100 nA between 2.7 V - 5.5 V (vs. Li/Li^+) for 30 cycles with 10 min rest between every 10 cycles. (b) shows the HAADF image of an NCM811 particle after cycling. (b) illustrates the relative atomic fraction of transition metals in the selective regions in (a) (the yellow box indicates the particle edge particle, and the orange box indicates the particle center). (c) depicts an EDS line profile across the particle (white

arrow in HAADF image) that demonstrates the distribution of the three transition metals. (e-j) EDS elemental maps for Ni (green), Co (red), Mn (blue), O (orange), F (turquoise), and C (purple).

6.4. Conclusion

The electrochemical measurement of the micro-battery protocol in the liquid cell is reliable and reproducible for *in situ* analysis. NCM811 shows not only less stability under the same cycling condition in the liquid cell compared to NCM622 but also different degradation mechanisms. The influence of increasing Ni content on NCM dominates in the interaction of particle surface with the electrolyte other than the intraparticle phase transformation in the accelerated (high charge/discharge rate) cycling conditions. Sufficient resting time is necessary to compensate for the rate effect and discover the surface structural related degradation mechanism of various Ni-rich NCM materials.

Chapter 7: Conclusions and perspectives

Observing the dynamic evolution of the interface and internal structure of lithium-ion battery electrodes during operation can extend our understanding of the underlying degradation mechanisms by correlating the material evolution with its electrochemical performance decay. *In situ* TEM is a promising diagnostic technique with the potential of monitoring the structural and chemical degradation processes with high spatial, temporal, and energy resolution. Nevertheless, the integration of the liquid electrolyte and electrode system in the TEM holder for running reliable electrochemical measurements remains a fundamental challenge.

Therefore, the aim of this thesis was to optimize the liquid phase electrochemical TEM system for battery cycling. The on-chip micro-battery setup has been firstly revised from both liquid cell system and cycling condition aspects. Symmetric electrode configuration and proper functionalization of the electrode have improved the reproducibility of battery cycling. Electrode materials have been processed into compatible size to the liquid cell by milling while preserving their properties. Dropcasting was found to be a practical method for material loading on the chip. Galvanostatic cycling with additional pause conditions was shown to be more reliable than cyclic voltammetry for the characterization of the electrode materials at nanoscale in the liquid cell.

Using the optimized system, degradation mechanisms of Ni-rich NCM layered oxide cathodes for high energy density lithium-ion batteries have been analyzed with post mortem STEM-EDS. The detrimental reactions for Ni-rich NCM capacity fade were thereby identified. The electrode degradation was evaluated as gradual capacity decay or electrode isolation from the electrolyte, for which we assume it is caused by bulk phase transition and surface reaction, respectively. Increasing Ni content in NCM particles was found to facilitate the surface reaction between the electrode and electrolyte so that the electrode degradation is more likely to result in resistive surface layer formation. The subtle compositional deficiency due to the surface layer formation that is observed in NCM811 is responsible for the irreversible capacity loss. In comparison, the NCM622 electrode loses its reversible capacity through bulk phase transformation with distinct compositional domains, from which the diffusion path of lithium ions within the material is halted.

To conclude, in general, the methodology described in this thesis for studying the electrochemical process in the liquid cell can provide reasonable electrochemical measurements by adjusting the conventional cycling parameter to overcome the geometry limitation. It can also be used for analyzing other electrochemical stimuli triggered phenomenon in the liquid phase. The degradation path variation that is discovered in Ni-rich NCM with different compositions brings novel insights on understanding the failure mechanism of NCM cathodes with increasing Ni content. Therefore, our results aspire towards the design of next-generation Ni-rich NCM cathodes with long-term advanced electrochemical performance and improved stability.

The electrochemical cell established in this thesis for TEM also opens up the possibility for fundamental studies of the solid electrolyte interphase formation and evolution, anode aging mechanism, and the influence from the electrode surface or electrolyte modification. Hence, valuable insights can be attained for systematic performance optimization in lithium-ion batteries. Moreover, the high current density involved in the electrochemical cycling in the liquid cell can be desirable for studying fast-charging lithium-ion batteries. Stabilizing the battery system under the extremely fast charging rates can be particularly interesting for battery-based EVs, which will promote the adoption of EVs in the future electric transportation.

Still, the ultimate goal is to have a robust system for performing operando diagnostic studies in liquid phase TEM that is capable of measuring the material properties during the *in situ* TEM studies and correlating their electrochemical measurements with structural characterization. This, however, needs to be further optimized for overcoming operational and interpretable challenges. The limited spatial/energy resolution of imaging or spectroscopy analyses remains a drawback due to the thickness of the liquid layer defined by the liquid cell membranes and the effects on particle and electrolyte degradation due to electron beam irradiation remains difficult to mitigate.

Bibliography

- [1] M. Li, J. Lu, Z. Chen, and K. Amine, “30 Years of Lithium-Ion Batteries,” *Adv. Mater.*, vol. 30, no. 33, pp. 1–24, 2018, doi: 10.1002/adma.201800561.
- [2] J. Tomić and W. Kempton, “Using fleets of electric-drive vehicles for grid support,” *J. Power Sources*, vol. 168, no. 2, pp. 459–468, 2007, doi: 10.1016/j.jpowsour.2007.03.010.
- [3] N. Nitta, F. Wu, J. T. Lee, and G. Yushin, “Li-ion battery materials: Present and future,” *Mater. Today*, vol. 18, no. 5, pp. 252–264, 2015, doi: 10.1016/j.mattod.2014.10.040.
- [4] O. Schmidt, A. Hawkes, A. Gambhir, and I. Staffell, “The future cost of electrical energy storage based on experience rates,” *Nat. Energy*, vol. 2, no. 8, pp. 1–8, 2017, doi: 10.1038/nenergy.2017.110.
- [5] B. Nykvist and M. Nilsson, “Rapidly falling costs of battery packs for electric vehicles,” *Nat. Clim. Chang.*, vol. 5, no. 4, pp. 329–332, 2015, doi: 10.1038/nclimate2564.
- [6] K. Edström *et al.*, “BATTERY 2030+. Inventing the sustainable batteries of the future. Research needs and future actions,” 2020.
- [7] M. Marinaro *et al.*, “Bringing forward the development of battery cells for automotive applications: Perspective of R&D activities in China, Japan, the EU and the USA,” *J. Power Sources*, vol. 459, no. March, p. 228073, 2020, doi: 10.1016/j.jpowsour.2020.228073.
- [8] EUCAR, “Battery requirements for future automotive applications,” in *Eg Bev&Fcev*, 2019, no. July, pp. 1–18.
- [9] H. Li, “Practical Evaluation of Li-Ion Batteries,” *Joule*, vol. 3, no. 4, pp. 911–914, 2019, doi: 10.1016/j.joule.2019.03.028.
- [10] B. Stiaszny, J. C. Ziegler, E. E. Krauß, M. Zhang, J. P. Schmidt, and E. Ivers-Tiffée, “Electrochemical characterization and post-mortem analysis of aged LiMn 2O4-NMC/graphite lithium ion batteries part II: Calendar aging,” *J. Power Sources*, vol. 258, pp. 61–75, 2014, doi:

- 10.1016/j.jpowsour.2014.02.019.
- [11] D. Qian, C. Ma, K. L. More, Y. S. Meng, and M. Chi, “Advanced analytical electron microscopy for lithium-ion batteries,” *NPG Asia Mater.*, vol. 7, no. 6, pp. 1–11, 2015, doi: 10.1038/am.2015.50.
 - [12] J. Chen, J. Liu, Y. Qi, T. Sun, and X. Li, “Unveiling the Roles of Binder in the Mechanical Integrity of Electrodes for Lithium-Ion Batteries,” *J. Electrochem. Soc.*, vol. 160, no. 9, pp. A1502–A1509, 2013, doi: 10.1149/2.088309jes.
 - [13] H. Zheng, R. Yang, G. Liu, X. Song, and V. S. Battaglia, “Cooperation between active material, polymeric binder and conductive carbon additive in lithium ion battery cathode,” *J. Phys. Chem. C*, vol. 116, no. 7, pp. 4875–4882, 2012, doi: 10.1021/jp208428w.
 - [14] M. Indrikova, S. Grunwald, F. Golks, A. Netz, B. Westphal, and A. Kwade, “The Morphology of Battery Electrodes with the Focus of the Conductive Additives Paths,” *J. Electrochem. Soc.*, vol. 162, no. 10, pp. A2021–A2025, 2015, doi: 10.1149/2.0441510jes.
 - [15] T. Ohzuku and Y. Makimura, “Layered lithium insertion material of $\text{LiCo}_{1/3}\text{Ni}_{1/3}\text{Mn}_{1/3}\text{O}_2$ for lithium-ion batteries,” *Chem. Lett.*, no. 7, pp. 642–643, 2001, doi: 10.1246/cl.2001.642.
 - [16] A. Chakraborty *et al.*, “Layered Cathode Materials for Lithium-Ion Batteries: Review of Computational Studies on $\text{LiNi}_{1-x}\text{yCo}_x\text{MnyO}_2$ and $\text{LiNi}_{1-x}\text{yCo}_x\text{AlyO}_2$,” *Chem. Mater.*, vol. 32, no. 3, pp. 915–952, 2020, doi: 10.1021/acs.chemmater.9b04066.
 - [17] L. Zhang and C. Chen, “Electrode materials for lithium ion battery,” *Prog. Chem.*, vol. 23, no. 2–3, pp. 275–283, 2011, doi: 10.1016/j.mset.2018.08.001.
 - [18] S. Goriparti, E. Miele, F. De Angelis, E. Di Fabrizio, R. Proietti Zaccaria, and C. Capiglia, “Review on recent progress of nanostructured anode materials for Li-ion batteries,” *J. Power Sources*, vol. 257, pp. 421–443, 2014, doi: 10.1016/j.jpowsour.2013.11.103.
 - [19] M. S. Balogun *et al.*, “A review of the development of full cell lithium-ion batteries: The impact of nanostructured anode materials,” *Nano Res.*, vol. 9, no. 10, pp. 2823–2851, 2016, doi:

- 10.1007/s12274-016-1171-1.
- [20] J. Lu, Z. Chen, F. Pan, Y. Cui, and K. Amine, “High-Performance Anode Materials for Rechargeable Lithium-Ion Batteries,” *Electrochem. Energy Rev.*, vol. 1, no. 1, pp. 35–53, 2018, doi: 10.1007/s41918-018-0001-4.
 - [21] W. J. Zhang, “A review of the electrochemical performance of alloy anodes for lithium-ion batteries,” *J. Power Sources*, vol. 196, no. 1, pp. 13–24, 2011, doi: 10.1016/j.jpowsour.2010.07.020.
 - [22] G. G. Botte, R. E. White, and Z. Zhang, “Thermal stability of LiPF₆-EC:EMC electrolyte for lithium ion batteries,” *J. Power Sources*, vol. 97–98, pp. 570–575, 2001, doi: 10.1016/S0378-7753(01)00746-7.
 - [23] Z. Wang, Y. Sun, L. Chen, and X. Huang, “Electrochemical Characterization of Positive Electrode Material LiNi_{1/3}Co_{1/3}Mn_{1/3}O₂ and Compatibility with Electrolyte for Lithium-Ion Batteries,” *J. Electrochem. Soc.*, vol. 151, no. 6, p. A914, 2004, doi: 10.1149/1.1740781.
 - [24] S. S. Zhang, “A review on electrolyte additives for lithium-ion batteries,” *J. Power Sources*, vol. 162, no. 2 SPEC. ISS., pp. 1379–1394, 2006, doi: 10.1016/j.jpowsour.2006.07.074.
 - [25] C. M. Julien, A. Mauger, K. Zaghib, and H. Groult, “Comparative Issues of Cathode Materials for Li-Ion Batteries,” *Inorganics*, vol. 2, pp. 132–154, 2014, doi: 10.3390/inorganics2020132.
 - [26] C. Daniel, D. Mohanty, J. Li, and D. L. Wood, “Cathode materials review,” *AIP Conf. Proc.*, vol. 1597, no. February, pp. 26–43, 2014, doi: 10.1063/1.4878478.
 - [27] A. Mendiboure, C. Delmas, and P. Hagenmuller, “New layered structure obtained by electrochemical deintercalation of the metastable LiCoO₂ (O₂) variety,” *Mater. Res. Bull.*, vol. 19, no. 10, pp. 1383–1392, 1984, doi: 10.1016/0025-5408(84)90204-6.
 - [28] Y. Jiang, C. Qin, P. Yan, and M. Sui, “Origins of capacity and voltage fading of LiCoO₂ upon high voltage cycling,” *J. Mater. Chem. A*, vol. 7, no. 36, pp. 20824–20831, 2019, doi: 10.1039/c9ta06579b.

- [29] M. M. Thackeray, W. I. F. David, P. G. Bruce, and J. B. Goodenough, "Lithium insertion into manganese spinels," *Mater. Res. Bull.*, vol. 18, no. 4, pp. 461–472, 1983, doi: 10.1016/0025-5408(83)90138-1.
- [30] A. Yamada, S. C. Chung, and K. Hinokuma, "Optimized LiFePO₄ for Lithium Battery Cathodes," *J. Electrochem. Soc.*, vol. 148, no. 3, p. A224, 2001, doi: 10.1149/1.1348257.
- [31] A. Rougier, P. Gravereau, and C. Delmas, "Optimization of the Composition of the Li_{1-z}Ni_{1+z}O₂ Electrode Materials: Structural, Magnetic, and Electrochemical Studies," *J. Electrochem. Soc.*, vol. 143, no. 4, pp. 1168–1175, 1996, doi: 10.1149/1.1836614.
- [32] H. Arai, S. Okada, Y. Sakurai, and J. I. Yamaki, "Thermal behavior of Li_{1-y}NiO₂ and the decomposition mechanism," *Solid State Ionics*, vol. 109, no. 3–4, pp. 295–302, 1998, doi: 10.1016/S0167-2738(98)00075-7.
- [33] B. Xu, D. Qian, Z. Wang, and Y. S. Meng, "Recent progress in cathode materials research for advanced lithium ion batteries," *Mater. Sci. Eng. R Reports*, vol. 73, no. 5–6, pp. 51–65, 2012, doi: 10.1016/j.mser.2012.05.003.
- [34] J. Xu, F. Lin, M. M. Doeff, and W. Tong, "A review of Ni-based layered oxides for rechargeable Li-ion batteries," *J. Mater. Chem. A*, vol. 5, no. 3, pp. 874–901, 2017, doi: 10.1039/C6TA07991A.
- [35] J. K. Ngala, N. A. Chernova, M. Ma, M. Mamak, P. Y. Zavalij, and M. S. Whittingham, "The synthesis, characterization and electrochemical behavior of the layered LiNi_{0.4}Mn_{0.4}Co_{0.2}O₂ compound," *J. Mater. Chem.*, vol. 14, no. 2, pp. 214–220, 2004, doi: 10.1039/b309834f.
- [36] S. T. Myung *et al.*, "Nickel-Rich Layered Cathode Materials for Automotive Lithium-Ion Batteries: Achievements and Perspectives," *ACS Energy Lett.*, vol. 2, no. 1, pp. 196–223, 2017, doi: 10.1021/acsenergylett.6b00594.
- [37] K. Kang, Y. S. Meng, J. Bréger, C. P. Grey, and G. Ceder, "Electrodes with high power and high capacity for rechargeable lithium batteries," *Science (80-.)*, vol. 311, no. 5763, pp. 977–980, 2006, doi: 10.1126/science.1122152.

- [38] R. Jung, M. Metzger, F. Maglia, C. Stinner, and H. A. Gasteiger, “Oxygen Release and Its Effect on the Cycling Stability of $\text{Li}_{1-x}\text{Ni}_x\text{Mn}_y\text{Co}_{1-x-y}\text{O}_2$ (NMC) Cathode Materials for Li-Ion Batteries,” *J. Electrochem. Soc.*, vol. 164, no. 7, pp. A1361–A1377, 2017, doi: 10.1149/2.0021707jes.
- [39] S. S. Zhang, “Problems and their origins of Ni-rich layered oxide cathode materials,” *Energy Storage Mater.*, vol. 24, no. July 2019, pp. 247–254, 2020, doi: 10.1016/j.ensm.2019.08.013.
- [40] C. Tian, F. Lin, and M. M. Doeff, “Electrochemical Characteristics of Layered Transition Metal Oxide Cathode Materials for Lithium Ion Batteries: Surface, Bulk Behavior, and Thermal Properties,” *Acc. Chem. Res.*, vol. 51, no. 1, pp. 89–96, Jan. 2017, doi: 10.1021/acs.accounts.7b00520.
- [41] Y. Ding, Z. P. Cano, A. Yu, J. Lu, and Z. Chen, “Automotive Li-Ion Batteries: Current Status and Future Perspectives,” *Electrochem. Energy Rev.*, vol. 2, no. 1, pp. 1–28, 2019, doi: 10.1007/s41918-018-0022-z.
- [42] S. B. Schougaard, J. Bréger, M. Jiang, C. P. Grey, and J. B. Goodenough, “ $\text{LiNi}_{0.5+\delta}\text{Mn}_{0.5-\delta}\text{O}_2$ -a high-rate, high-capacity cathode for lithium rechargeable batteries,” *Adv. Mater.*, vol. 18, no. 7, pp. 905–909, 2006, doi: 10.1002/adma.200500113.
- [43] E. Zhao *et al.*, “New insight into Li/Ni disorder in layered cathode materials for lithium ion batteries: A joint study of neutron diffraction, electrochemical kinetic analysis and first-principles calculations,” *J. Mater. Chem. A*, vol. 5, no. 4, pp. 1679–1686, 2017, doi: 10.1039/c6ta08448f.
- [44] H. Yu *et al.*, “Study of the lithium/nickel ions exchange in the layered $\text{LiNi}_{0.42}\text{Mn}_{0.42}\text{Co}_{0.16}\text{O}_2$ cathode material for lithium ion batteries: Experimental and first-principles calculations,” *Energy Environ. Sci.*, vol. 7, no. 3, pp. 1068–1078, 2014, doi: 10.1039/c3ee42398k.
- [45] Y. Koyama, H. Arai, I. Tanaka, Y. Uchimoto, and Z. Ogumi, “Defect chemistry in layered LiMO_2 ($\text{M} = \text{Co}, \text{Ni}, \text{Mn}$, and $\text{Li}_{1/3}\text{Mn}_{2/3}$) by first-principles calculations,” *Chem. Mater.*, vol. 24, no. 20, pp. 3886–3894, 2012, doi: 10.1021/cm3018314.

- [46] T. Li, X.-Z. Yuan, L. Zhang, D. Song, K. Shi, and C. Bock, “Degradation Mechanisms and Mitigation Strategies of Nickel-Rich NMC-Based Lithium-Ion Batteries,” *Electrochem. Energy Rev.*, vol. 3, no. 1, pp. 43–80, 2020, doi: 10.1007/s41918-019-00053-3.
- [47] H. H. Ryu, K. J. Park, C. S. Yoon, and Y. K. Sun, “Capacity fading of Ni-rich Li[Ni_xCo_yMn_{1-x-y}]O₂ (0.6 ≤ x ≤ 0.95) Cathodes for High-Energy-Density Lithium-Ion Batteries: Bulk or Surface Degradation?,” *Chem. Mater.*, vol. 30, no. 3, pp. 1155–1163, 2018, doi: 10.1021/acs.chemmater.7b05269.
- [48] P. Yan, J. Zheng, M. Gu, J. Xiao, J. G. Zhang, and C. M. Wang, “Intragranular cracking as a critical barrier for high-voltage usage of layer-structured cathode for lithium-ion batteries,” *Nat. Commun.*, vol. 8, pp. 1–9, 2017, doi: 10.1038/ncomms14101.
- [49] Y. K. Ahn, Y. N. Jo, W. Cho, J.-S. S. Yu, and K. J. Kim, “Mechanism of Capacity Fading in the LiNi_{0.8}Co_{0.1}Mn_{0.1}O₂ Cathode Material for Lithium-Ion Batteries,” *Energies*, vol. 12, no. 9, p. 1638, Apr. 2019, doi: 10.3390/en12091638.
- [50] R. Jung, M. Metzger, F. Maglia, C. Stinner, and H. A. Gasteiger, “Chemical versus electrochemical electrolyte oxidation on NMC111, NMC622, NMC811, LNMO, and conductive carbon,” *J. Phys. Chem. Lett.*, vol. 8, no. 19, pp. 4820–4825, 2017, doi: 10.1021/acs.jpcclett.7b01927.
- [51] S. M. Bak *et al.*, “Structural changes and thermal stability of charged LiNi_xMn_yCo_zO₂ cathode materials studied by combined in situ time-resolved XRD and mass spectroscopy,” *ACS Appl. Mater. Interfaces*, vol. 6, no. 24, pp. 22594–22601, 2014, doi: 10.1021/am506712c.
- [52] F. Lin *et al.*, “Surface reconstruction and chemical evolution of stoichiometric layered cathode materials for lithium-ion batteries,” *Nat. Commun.*, vol. 5, no. March, p. 3529, 2014, doi: 10.1038/ncomms4529.
- [53] N. Y. Kim, T. Yim, J. H. Song, J. S. Yu, and Z. Lee, “Microstructural study on degradation mechanism of layered LiNi_{0.6}Co_{0.2}Mn_{0.2}O₂ cathode materials by analytical transmission electron microscopy,” *J. Power Sources*, vol. 307, pp. 641–648, 2016, doi:

10.1016/j.jpowsour.2016.01.023.

- [54] M. Dixit, B. Markovsky, F. Schipper, D. Aurbach, and D. T. Major, “Origin of Structural Degradation during Cycling and Low Thermal Stability of Ni-Rich Layered Transition Metal-Based Electrode Materials,” *J. Phys. Chem. C*, vol. 121, no. 41, pp. 22628–22636, 2017, doi: 10.1021/acs.jpcc.7b06122.
- [55] A. Tornheim *et al.*, “Effect of electrolyte composition on rock salt surface degradation in NMC cathodes during high-voltage potentiostatic holds,” *Nano Energy*, vol. 55, no. October 2018, pp. 216–225, 2019, doi: 10.1016/j.nanoen.2018.10.065.
- [56] H. R. Morin *et al.*, “Transition-Metal Dissolution from NMC-Family Oxides: A Case Study,” *ACS Appl. Energy Mater.*, vol. 3, no. 3, pp. 2565–2575, 2020, doi: 10.1021/acsaem.9b02277.
- [57] J. Wandt *et al.*, “Transition metal dissolution and deposition in Li-ion batteries investigated by operando X-ray absorption spectroscopy,” *J. Mater. Chem. A*, vol. 4, no. 47, pp. 18300–18305, Nov. 2016, doi: 10.1039/C6TA08865A.
- [58] P. Lyu, Y. Huo, Z. Qu, and Z. Rao, “Investigation on the thermal behavior of Ni-rich NMC lithium ion battery for energy storage,” *Appl. Therm. Eng.*, vol. 166, no. May 2019, p. 114749, 2020, doi: 10.1016/j.applthermaleng.2019.114749.
- [59] H.-J. J. Noh, S. Youn, C. S. Yoon, and Y.-K. K. Sun, “Comparison of the structural and electrochemical properties of layered $\text{Li}[\text{Ni}_x\text{Co}_y\text{Mn}_z]\text{O}_2$ ($x = 1/3, 0.5, 0.6, 0.7, 0.8$ and 0.85) cathode material for lithium-ion batteries,” *J. Power Sources*, vol. 233, pp. 121–130, Jul. 2013, doi: 10.1016/j.jpowsour.2013.01.063.
- [60] H. Maleki Kheimeh Sari and X. Li, “Controllable Cathode–Electrolyte Interface of $\text{Li}[\text{Ni}_{0.8}\text{Co}_{0.1}\text{Mn}_{0.1}]\text{O}_2$ for Lithium Ion Batteries: A Review,” *Adv. Energy Mater.*, vol. 9, no. 39, pp. 1–31, 2019, doi: 10.1002/aenm.201901597.
- [61] S. Neudeck, A. Mazilkin, C. Reitz, P. Hartmann, J. Janek, and T. Brezesinski, “Effect of Low-Temperature Al_2O_3 ALD Coating on Ni-Rich Layered Oxide Composite Cathode on the Long-Term Cycling Performance of Lithium-Ion Batteries,” *Sci. Rep.*, vol. 9, no. 1, pp. 1–11, 2019,

doi: 10.1038/s41598-019-41767-0.

- [62] X. Xu *et al.*, “Progressive concentration gradient nickel-rich oxide cathode material for high-energy and long-life lithium-ion batteries,” *J. Mater. Chem. A*, vol. 7, no. 13, pp. 7728–7735, 2019, doi: 10.1039/C9TA00224C.
- [63] S. Zheng *et al.*, “Microstructural Changes in LiNi_{0.8}Co_{0.15}Al_{0.05}O₂ Positive Electrode Material during the First Cycle,” *J. Electrochem. Soc.*, vol. 158, no. 4, p. A357, 2011, doi: 10.1149/1.3544843.
- [64] M. D. Radin *et al.*, “Narrowing the Gap between Theoretical and Practical Capacities in Li-Ion Layered Oxide Cathode Materials,” *Adv. Energy Mater.*, vol. 7, no. 20, pp. 1–33, 2017, doi: 10.1002/aenm.201602888.
- [65] C. Liu, Z. G. Neale, and G. Cao, “Understanding electrochemical potentials of cathode materials in rechargeable batteries,” *Mater. Today*, vol. 19, no. 2, pp. 109–123, 2016, doi: 10.1016/j.mattod.2015.10.009.
- [66] J. B. Goodenough and Y. Kim, “Challenges for rechargeable Li batteries,” *Chem. Mater.*, vol. 22, no. 3, pp. 587–603, 2010, doi: 10.1021/cm901452z.
- [67] Y. X. Lin, Z. Liu, K. Leung, L. Q. Chen, P. Lu, and Y. Qi, “Connecting the irreversible capacity loss in Li-ion batteries with the electronic insulating properties of solid electrolyte interphase (SEI) components,” *J. Power Sources*, vol. 309, pp. 221–230, 2016, doi: 10.1016/j.jpowsour.2016.01.078.
- [68] S. J. An, J. Li, C. Daniel, D. Mohanty, S. Nagpure, and D. L. Wood, “The state of understanding of the lithium-ion-battery graphite solid electrolyte interphase (SEI) and its relationship to formation cycling,” *Carbon N. Y.*, vol. 105, pp. 52–76, 2016, doi: 10.1016/j.carbon.2016.04.008.
- [69] S. Ge *et al.*, “A new approach to both high safety and high performance of lithium-ion batteries,” *Sci. Adv.*, vol. 6, no. 9, pp. 1–9, 2020, doi: 10.1126/sciadv.aay7633.
- [70] Y. T. Weng *et al.*, “An ultrathin ionomer interphase for high efficiency lithium anode in

- carbonate based electrolyte,” *Nat. Commun.*, vol. 10, no. 1, pp. 1–10, 2019, doi: 10.1038/s41467-019-13783-1.
- [71] P. Teichert, G. G. Eshetu, H. Jahnke, and E. Figgemeier, “Degradation and aging routes of ni-rich cathode based li-ion batteries,” *Batteries*, vol. 6, no. 1, pp. 1–26, 2020, doi: 10.3390/batteries6010008.
- [72] Y. Xing, W. He, M. Pecht, and K. L. Tsui, “State of charge estimation of lithium-ion batteries using the open-circuit voltage at various ambient temperatures,” *Appl. Energy*, vol. 113, pp. 106–115, 2014, doi: 10.1016/j.apenergy.2013.07.008.
- [73] J. Li, L. E. Downie, L. Ma, W. Qiu, and J. R. Dahn, “Study of the Failure Mechanisms of $\text{LiNi}_{0.8}\text{Mn}_{0.1}\text{Co}_{0.1}\text{O}_2$ Cathode Material for Lithium Ion Batteries,” *J. Electrochem. Soc.*, vol. 162, no. 7, pp. A1401–A1408, 2015, doi: 10.1149/2.1011507jes.
- [74] N. Zhang *et al.*, “Structural, Electrochemical, and Thermal Properties of Nickel-Rich $\text{LiNi}_x\text{Mn}_y\text{Co}_z\text{O}_2$ Materials,” *Chem. Mater.*, vol. 30, no. 24, pp. 8852–8860, 2018, doi: 10.1021/acs.chemmater.8b03827.
- [75] U. Tröltzsch, O. Kanoun, and H. R. Tränkler, “Characterizing aging effects of lithium ion batteries by impedance spectroscopy,” *Electrochim. Acta*, vol. 51, no. 8–9, pp. 1664–1672, 2006, doi: 10.1016/j.electacta.2005.02.148.
- [76] V. J. Ovejas and A. Cuadras, “Impedance characterization of an LCO-NMC/graphite cell: Ohmic conduction, SEI transport and charge-transfer phenomenon,” *Batteries*, vol. 4, no. 3, 2018, doi: 10.3390/batteries4030043.
- [77] X. Zhou, J. Huang, Z. Pan, and M. Ouyang, “Impedance characterization of lithium-ion batteries aging under high-temperature cycling: Importance of electrolyte-phase diffusion,” *J. Power Sources*, vol. 426, no. December 2018, pp. 216–222, 2019, doi: 10.1016/j.jpowsour.2019.04.040.
- [78] M. Labrini, I. Saadoun, A. Almaggoussi, J. Elhaskouri, and P. Amoros, “The $\text{Li}_y\text{Ni}_{0.2}\text{Mn}_{0.2}\text{Co}_{0.6}\text{O}_2$ electrode materials: A structural and magnetic study,” *Mater. Res. Bull.*, vol. 47, no. 4, pp. 1004–1009, 2012, doi: 10.1016/j.materresbull.2012.01.008.

- [79] A. O. Kondrakov *et al.*, “Anisotropic Lattice Strain and Mechanical Degradation of High- and Low-Nickel NCM Cathode Materials for Li-Ion Batteries,” *J. Phys. Chem. C*, vol. 121, no. 6, pp. 3286–3294, 2017, doi: 10.1021/acs.jpcc.6b12885.
- [80] Q. Lin *et al.*, “Ni–Li anti-site defect induced intragranular cracking in Ni-rich layer-structured cathode,” *Nano Energy*, vol. 76, no. June, p. 105021, 2020, doi: 10.1016/j.nanoen.2020.105021.
- [81] K. Märker, P. J. Reeves, C. Xu, K. J. Griffith, and C. P. Grey, “Evolution of Structure and Lithium Dynamics in LiNi_{0.8}Mn_{0.1}Co_{0.1}O₂ (NMC811) Cathodes during Electrochemical Cycling,” *Chem. Mater.*, vol. 31, no. 7, pp. 2545–2554, 2019, doi: 10.1021/acs.chemmater.9b00140.
- [82] X. Mu *et al.*, “Comprehensive analysis of TEM methods for LiFePO₄/FePO₄ phase mapping: spectroscopic techniques (EFTEM, STEM-EELS) and STEM diffraction techniques (ACOM-TEM),” *Ultramicroscopy*, vol. 170, pp. 10–18, 2016, doi: 10.1016/j.ultramic.2016.07.009.
- [83] J. D. Sugar *et al.*, “High-resolution chemical analysis on cycled LiFePO₄ battery electrodes using energy-filtered transmission electron microscopy,” *J. Power Sources*, vol. 246, pp. 512–521, 2014, doi: 10.1016/j.jpowsour.2013.08.003.
- [84] C. Vidal-Abarca, P. Lavela, and J. L. Tirado, “The Origin of Capacity Fading in NiFe₂O₄ Conversion Electrodes for Lithium Ion Batteries Unfolded by ⁵⁷Fe Mossbauer Spectroscopy,” *J. Phys. Chem. C*, vol. 114, no. 29, pp. 12828–12832, 2010, doi: 10.1021/jp103888a.
- [85] O. Pecher, J. Carretero-Gonzalez, K. J. Griffith, and C. P. Grey, “Materials’ methods: NMR in battery research,” *Chem. Mater.*, vol. 29, no. 1, pp. 213–242, 2017, doi: 10.1021/acs.chemmater.6b03183.
- [86] C. P. Grey and J. M. Tarascon, “Sustainability and in situ monitoring in battery development,” *Nat. Mater.*, vol. 16, no. 1, pp. 45–56, 2016, doi: 10.1038/nmat4777.
- [87] C. Shen, S. Wang, Y. Jin, and W. Q. Han, “In Situ AFM Imaging of Solid Electrolyte Interfaces on HOPG with Ethylene Carbonate and Fluoroethylene Carbonate-Based Electrolytes,” *ACS Appl. Mater. Interfaces*, vol. 7, no. 45, pp. 25441–25447, 2015, doi: 10.1021/acsami.5b08238.

- [88] I. Landa-Medrano *et al.*, “In Situ Analysis of NMC|graphite Li-Ion Batteries by Means of Complementary Electrochemical Methods,” *J. Electrochem. Soc.*, vol. 167, no. 9, p. 090528, 2020, doi: 10.1149/1945-7111/ab8b99.
- [89] N. Sharma *et al.*, “Structural changes in a commercial lithium-ion battery during electrochemical cycling: An in situ neutron diffraction study,” *J. Power Sources*, vol. 195, no. 24, pp. 8258–8266, 2010, doi: 10.1016/j.jpowsour.2010.06.114.
- [90] L. Vitoux, M. Reichardt, S. Sallard, P. Novák, D. Sheptyakov, and C. Villevieille, “A cylindrical cell for operando neutron diffraction of Li-ion battery electrode materials,” *Front. Energy Res.*, vol. 6, no. AUG, pp. 1–16, 2018, doi: 10.3389/fenrg.2018.00076.
- [91] M. A. Rodriguez, D. Ingersoll, S. C. Vogel, and D. J. Williams, “Simultaneous in Situ Neutron Diffraction Studies of the Anode and Cathode in a Lithium-Ion Cell,” *Electrochem. Solid-State Lett.*, vol. 7, no. 1, pp. 8–11, 2004, doi: 10.1149/1.1628664.
- [92] X. L. Wang *et al.*, “Visualizing the chemistry and structure dynamics in lithium-ion batteries by in-situ neutron diffraction,” *Sci. Rep.*, vol. 2, pp. 1–7, 2012, doi: 10.1038/srep00747.
- [93] N. Sharma *et al.*, “Direct evidence of concurrent solid-solution and two-phase reactions and the nonequilibrium structural evolution of LiFePO_4 ,” *J. Am. Chem. Soc.*, vol. 134, no. 18, pp. 7867–7873, 2012, doi: 10.1021/ja301187u.
- [94] S. Taminato *et al.*, “Real-time observations of lithium battery reactions - Operando neutron diffraction analysis during practical operation,” *Sci. Rep.*, vol. 6, no. February, pp. 1–12, 2016, doi: 10.1038/srep28843.
- [95] F. Lin *et al.*, “Synchrotron X-ray Analytical Techniques for Studying Materials Electrochemistry in Rechargeable Batteries,” *Chem. Rev.*, p. acs.chemrev.7b00007, Sep. 2017, doi: 10.1021/acs.chemrev.7b00007.
- [96] X. Zhang *et al.*, “Direct view on the phase evolution in individual LiFePO_4 nanoparticles during Li-ion battery cycling,” *Nat. Commun.*, vol. 6, no. May, pp. 1–7, 2015, doi: 10.1038/ncomms9333.

- [97] J. Lim *et al.*, “Origin and hysteresis of lithium compositional spatiodynamics within battery primary particles,” *Science* (80-.), vol. 353, no. 6299, pp. 566–571, 2016, doi: 10.1126/science.aaf4914.
- [98] D. Liu *et al.*, “Review of Recent Development of In Situ/Operando Characterization Techniques for Lithium Battery Research,” *Adv. Mater.*, vol. 31, no. 28, pp. 1–57, 2019, doi: 10.1002/adma.201806620.
- [99] S. M. Bak, Z. Shadike, R. Lin, X. Yu, and X. Q. Yang, “In situ/operando synchrotron-based X-ray techniques for lithium-ion battery research,” *NPG Asia Mater.*, vol. 10, no. 7, pp. 563–580, 2018, doi: 10.1038/s41427-018-0056-z.
- [100] K. Kleiner *et al.*, “Origin of High Capacity and Poor Cycling Stability of Li-Rich Layered Oxides: A Long-Duration in Situ Synchrotron Powder Diffraction Study,” *Chem. Mater.*, vol. 30, no. 11, pp. 3656–3667, 2018, doi: 10.1021/acs.chemmater.8b00163.
- [101] D. Chen, S. Indris, M. Schulz, B. Gamer, and R. Mönig, “In situ scanning electron microscopy on lithium-ion battery electrodes using an ionic liquid,” *J. Power Sources*, vol. 196, no. 15, pp. 6382–6387, 2011, doi: 10.1016/j.jpowsour.2011.04.009.
- [102] G. Rong *et al.*, “Liquid-Phase Electrochemical Scanning Electron Microscopy for In Situ Investigation of Lithium Dendrite Growth and Dissolution,” *Adv. Mater.*, vol. 29, no. 13, 2017, doi: 10.1002/adma.201606187.
- [103] X. H. Liu *et al.*, “In situ atomic-scale imaging of electrochemical lithiation in silicon,” *Nat. Nanotechnol.*, vol. 7, no. 11, pp. 749–756, 2012, doi: 10.1038/nnano.2012.170.
- [104] X. H. Liu *et al.*, “Ultrafast electrochemical lithiation of individual Si nanowire anodes,” *Nano Lett.*, vol. 11, no. 6, pp. 2251–2258, 2011, doi: 10.1021/nl200412p.
- [105] J. Y. Huang *et al.*, “In Situ Observation of the Electrochemical Lithiation of a Single SnO₂ Nanowire Electrode,” *Science* (80-.), vol. 330, no. 6010, pp. 1515 LP – 1520, Dec. 2010, doi: 10.1126/science.1195628.

- [106] S. Lee *et al.*, “Phase transitions in a LiMn₂O₄ nanowire battery observed by operando electron microscopy,” *ACS Nano*, vol. 9, no. 1, pp. 626–632, Jan. 2015, doi: 10.1021/nn505952k.
- [107] H. Wang and F. Wang, “In situ, operando measurements of rechargeable batteries,” *Curr. Opin. Chem. Eng.*, vol. 13, pp. 170–178, 2016, doi: 10.1016/j.coche.2016.09.002.
- [108] M. J. Williamson, R. M. Tromp, P. M. Vereecken, R. Hull, and F. M. Ross, “Dynamic microscopy of nanoscale cluster growth at the solid-liquid interface,” *Nat. Mater.*, vol. 2, no. 8, pp. 532–536, 2003, doi: 10.1038/nmat944.
- [109] M. E. Holtz *et al.*, “Nanoscale imaging of lithium ion distribution during in situ operation of battery electrode and electrolyte,” *Nano Lett.*, vol. 14, no. 3, pp. 1453–1459, 2014, doi: 10.1021/nl404577c.
- [110] O. M. Karakulina, A. Demortière, W. Dachraoui, A. M. Abakumov, and J. Hadermann, “In Situ Electron Diffraction Tomography Using a Liquid-Electrochemical Transmission Electron Microscopy Cell for Crystal Structure Determination of Cathode Materials for Li-Ion batteries,” *Nano Lett.*, vol. 18, no. 10, pp. 6286–6291, 2018, doi: 10.1021/acs.nanolett.8b02436.
- [111] L. Lutz *et al.*, “Operando Monitoring of the Solution-Mediated Discharge and Charge Processes in a Na-O₂ Battery Using Liquid-Electrochemical Transmission Electron Microscopy,” *Nano Lett.*, vol. 18, no. 2, pp. 1280–1289, 2018, doi: 10.1021/acs.nanolett.7b04937.
- [112] Z. Zeng, W. I. Liang, H. G. Liao, H. L. Xin, Y. H. Chu, and H. Zheng, “Visualization of electrode-electrolyte interfaces in LiPF₆/EC/DEC electrolyte for lithium ion batteries via in situ TEM,” *Nano Lett.*, vol. 14, no. 4, pp. 1745–1750, 2014, doi: 10.1021/nl403922u.
- [113] A. J. Leenheer, K. L. Jungjohann, K. R. Zavadil, and C. T. Harris, “Phase Boundary Propagation in Li-Alloying Battery Electrodes Revealed by Liquid-Cell Transmission Electron Microscopy,” *ACS Nano*, vol. 10, no. 6, pp. 5670–5678, 2016, doi: 10.1021/acsnano.6b02200.
- [114] R. R. Unocic *et al.*, “Direct visualization of solid electrolyte interphase formation in lithium-ion batteries with in situ electrochemical transmission electron microscopy,” *Microsc. Microanal.*, vol. 20, no. 4, pp. 1029–1037, 2014, doi: 10.1017/S1431927614012744.

- [115] I. M. Abrams and J. W. McBain, "A closed cell for electron microscopy," *J. Appl. Phys.*, vol. 15, no. 8, pp. 607–609, Aug. 1944, doi: 10.1063/1.1707475.
- [116] N. De Jonge and F. M. Ross, "Electron microscopy of specimens in liquid," *Nat. Nanotechnol.*, vol. 6, no. 11, pp. 695–704, 2011, doi: 10.1038/nnano.2011.161.
- [117] F. Wu and N. Yao, "Advances in sealed liquid cells for in-situ TEM electrochemical investigation of lithium-ion battery," *Nano Energy*, vol. 11, pp. 196–210, 2015, doi: 10.1016/j.nanoen.2014.11.004.
- [118] A. J. Leenheer, J. P. Sullivan, M. J. Shaw, and C. T. Harris, "A Sealed Liquid Cell for in Situ Transmission Electron Microscopy of Controlled Electrochemical Processes," *J. Microelectromechanical Syst.*, vol. 24, no. 4, pp. 1061–1068, 2015, doi: 10.1109/JMEMS.2014.2380771.
- [119] Z. Chen, Y. Qin, K. Amine, and Y. K. Sun, "Role of surface coating on cathode materials for lithium-ion batteries," *J. Mater. Chem.*, vol. 20, no. 36, pp. 7606–7612, 2010, doi: 10.1039/c0jm00154f.
- [120] R. Raccichini, M. Amores, and G. Hinds, "Critical Review of the Use of Reference Electrodes in Li-Ion Batteries: A Diagnostic Perspective," *Batteries*, vol. 5, no. 1, p. 12, Jan. 2019, doi: 10.3390/batteries5010012.
- [121] R. D. Minter, D. Juarez-Robles, C. Fear, Y. Barsukov, and P. P. Mukherjee, "Three-electrode coin cell preparation and electrodeposition analytics for Lithium-ion batteries," *J. Vis. Exp.*, vol. 2018, no. 135, p. 57735, 2018, doi: 10.3791/57735.
- [122] J. Asenbauer, T. Eisenmann, M. Kuenzel, A. Kazzazi, Z. Chen, and D. Bresser, "The success story of graphite as a lithium-ion anode material – fundamentals, remaining challenges, and recent developments including silicon (oxide) composites," *Sustain. Energy Fuels*, 2020, doi: 10.1039/d0se00175a.
- [123] C. M. Park, J. H. Kim, H. Kim, and H. J. Sohn, "Li-alloy based anode materials for Li secondary batteries," *Chem. Soc. Rev.*, vol. 39, no. 8, pp. 3115–3141, 2010, doi: 10.1039/b919877f.

- [124] M. Ashuri, Q. He, and L. L. Shaw, “Silicon as a potential anode material for Li-ion batteries: Where size, geometry and structure matter,” *Nanoscale*, vol. 8, no. 1, pp. 74–103, 2016, doi: 10.1039/c5nr05116a.
- [125] D. Son, E. Kim, T. G. Kim, M. G. Kim, J. Cho, and B. Park, “Nanoparticle iron-phosphate anode material for Li-ion battery,” *Appl. Phys. Lett.*, vol. 85, no. 24, pp. 5875–5877, 2004, doi: 10.1063/1.1835995.
- [126] F. Lin, I. M. Markus, M. M. Doeff, and H. L. Xin, “Chemical and structural stability of lithium-ion battery electrode materials under electron beam,” *Sci. Rep.*, vol. 4, no. 1, pp. 1–6, Jul. 2014, doi: 10.1038/srep05694.
- [127] N. Jiang and J. C. H. Spence, “On the dose-rate threshold of beam damage in TEM,” *Ultramicroscopy*, vol. 113, pp. 77–82, Feb. 2012, doi: 10.1016/j.ultramic.2011.11.016.
- [128] J. H. Shim, H. Kang, S. Lee, and Y. M. Kim, “Utilization of electron-beam irradiation under atomic-scale chemical mapping for evaluating the cycling performance of lithium transition metal oxide cathodes,” *J. Mater. Chem. A*, vol. 9, no. 4, pp. 2429–2437, Jan. 2021, doi: 10.1039/d0ta10415a.
- [129] J. H. Shim, H. Kang, Y. M. Kim, and S. Lee, “In Situ Observation of the Effect of Accelerating Voltage on Electron Beam Damage of Layered Cathode Materials for Lithium-Ion Batteries,” *ACS Appl. Mater. Interfaces*, vol. 11, no. 47, pp. 44293–44299, 2019, doi: 10.1021/acsami.9b15608.
- [130] P. Lu, P. Yan, E. Romero, E. D. Spörke, J. G. Zhang, and C. M. Wang, “Observation of electron-beam-induced phase evolution mimicking the effect of the charge-discharge cycle in Li-rich layered cathode materials used for Li ion batteries,” *Chem. Mater.*, vol. 27, no. 4, pp. 1375–1380, 2015, doi: 10.1021/cm5045573.
- [131] N. R. Lugg, G. Kothleitner, N. Shibata, and Y. Ikuhara, “On the quantitateness of EDS STEM,” *Ultramicroscopy*, vol. 151, pp. 150–159, Apr. 2015, doi: 10.1016/j.ultramic.2014.11.029.
- [132] D. B. Williams and C. B. Carter, *Transmission electron microscopy: A textbook for materials*

- science*. Springer US, 2009.
- [133] N. J. Zaluzec, M. G. Burke, S. J. Haigh, and M. A. Kulzick, “X-ray energy-dispersive spectrometry during in situ liquid cell studies using an analytical electron microscope,” *Microsc. Microanal.*, vol. 20, no. 2, pp. 323–329, 2014, doi: 10.1017/S1431927614000154.
 - [134] D. J. Kelly *et al.*, “Liquid-Phase STEM-EDS in Graphene and Silicon Nitride Cells,” *Microsc. Microanal.*, vol. 25, no. S2, pp. 1500–1501, Aug. 2019, doi: 10.1017/s1431927619008237.
 - [135] J. Hou, R. Girod, N. Nianias, T. H. Shen, J. Fan, and V. Tileli, “Lithium-Gold Reference Electrode for Potential Stability during in Situ Electron Microscopy Studies of Lithium-Ion Batteries,” *J. Electrochem. Soc.*, vol. 167, no. 11, p. 110515, 2020, doi: 10.1149/1945-7111/ab9eea.
 - [136] J. Zhou and P. H. L. Notten, “Development of Reliable Lithium Microreference Electrodes for Long-Term In Situ Studies of Lithium-Based Battery Systems,” *J. Electrochem. Soc.*, vol. 151, no. 12, p. A2173, 2004, doi: 10.1149/1.1813652.
 - [137] S. Solchenbach, D. Pritzl, E. J. Y. Kong, J. Landesfeind, and H. A. Gasteiger, “A Gold Micro-Reference Electrode for Impedance and Potential Measurements in Lithium Ion Batteries,” *J. Electrochem. Soc.*, vol. 163, no. 10, pp. A2265–A2272, Aug. 2016, doi: 10.1149/2.0581610jes.
 - [138] P. Bach, M. Stratmann, I. Valencia-Jaime, A. H. Romero, and F. U. Renner, “Lithiation and delithiation mechanisms of gold thin film model anodes for lithium ion batteries: Electrochemical characterization,” *Electrochim. Acta*, vol. 164, pp. 81–89, 2015, doi: 10.1016/j.electacta.2015.02.184.
 - [139] Z. Zeng, W. I. Liang, Y. H. Chu, and H. Zheng, “In situ TEM study of the Li-Au reaction in an electrochemical liquid cell,” *Faraday Discuss.*, vol. 176, pp. 95–107, 2014, doi: 10.1039/c4fd00145a.
 - [140] E. Fahrenkrug, D. H. Alsem, N. Salmon, and S. Maldonado, “Electrochemical Measurements in In Situ TEM Experiments,” *J. Electrochem. Soc.*, vol. 164, no. 6, pp. H358–H364, Apr. 2017, doi: 10.1149/2.1041706jes.

- [141] R. Girod, N. Nianias, and V. Tileli, “Electrochemical Behavior of Carbon Electrodes for in Situ Redox Studies in a Transmission Electron Microscope,” *Microsc. Microanal.*, vol. 25, no. 2019, pp. 1304–1310, 2019, doi: 10.1017/S1431927619015034.
- [142] P. Bach, I. Valencia-Jaime, U. Rütt, O. Gutowski, A. H. Romero, and F. U. Renner, “Electrochemical Lithiation Cycles of Gold Anodes Observed by in Situ High-Energy X-ray Diffraction,” *Chem. Mater.*, vol. 28, no. 9, pp. 2941–2948, 2016, doi: 10.1021/acs.chemmater.5b04719.
- [143] K. Yan *et al.*, “Selective deposition and stable encapsulation of lithium through heterogeneous seeded growth,” *Nat. Energy*, vol. 1, no. 3, 2016, doi: 10.1038/NENERGY.2016.10.
- [144] M. N. Obrovac and L. Christensen, “Structural changes in silicon anodes during lithium insertion/extraction,” *Electrochem. Solid-State Lett.*, vol. 7, no. 5, 2004, doi: 10.1149/1.1652421.
- [145] H.-C. Liu, W.-H. Ho, C.-F. Li, and S.-K. Yen, “Electrochemical Synthesis of FePO₄ for Anodes in Rechargeable Lithium Batteries,” *J. Electrochem. Soc.*, vol. 155, no. 12, p. E178, 2008, doi: 10.1149/1.2988061.
- [146] Y. Huang, H. Liu, L. Gong, Y. Hou, and Q. Li, “A simple route to improve rate performance of LiFePO₄/reduced graphene oxide composite cathode by adding Mg²⁺ via mechanical mixing,” *J. Power Sources*, vol. 347, pp. 29–36, 2017, doi: 10.1016/j.jpowsour.2017.02.043.
- [147] P. Bai, J. Li, F. R. Brushett, and M. Z. Bazant, “Transition of lithium growth mechanisms in liquid electrolytes,” *Energy Environ. Sci.*, vol. 9, no. 10, pp. 3221–3229, 2016, doi: 10.1039/c6ee01674j.
- [148] K. Nishio, M. Yoshida, and H. Masuda, “Fabrication of Nanoporous Pt by Electrochemical Alloying and Dealloying with Li,” *ECS Electrochem. Lett.*, vol. 2, no. 11, pp. C43–C45, Aug. 2013, doi: 10.1149/2.007311eel.
- [149] Z. Zeng, W.-I. Liang, Y.-H. Chu, and H. Zheng, “In situ TEM study of the Li–Au reaction in an electrochemical liquid cell,” *Faraday Discuss.*, vol. 176, pp. 95–107, 2014, doi: 10.1039/C4FD00145A.

- [150] D. Y. W. Yu *et al.*, “Study of LiFePO₄ by Cyclic Voltammetry,” *J. Electrochem. Soc.*, vol. 154, no. 4, p. A253, Feb. 2007, doi: 10.1149/1.2434687.
- [151] Y. Orikasa *et al.*, “Transient phase change in two phase reaction between LiFePO₄ and FePO₄ under battery operation,” *Chem. Mater.*, vol. 25, no. 7, pp. 1032–1039, 2013, doi: 10.1021/cm303411t.
- [152] R. R. Unocic *et al.*, “Quantitative electrochemical measurements using in situ ec-S/TEM devices,” *Microsc. Microanal.*, vol. 20, no. 2, pp. 452–461, 2014, doi: 10.1017/S1431927614000166.
- [153] P. Abellan *et al.*, “Factors influencing quantitative liquid (scanning) transmission electron microscopy,” *Chem. Commun.*, vol. 50, no. 38, pp. 4873–4880, Apr. 2014, doi: 10.1039/C3CC48479C.
- [154] R. Younesi, G. M. Veith, P. Johansson, K. Edström, and T. Vegge, “Lithium salts for advanced lithium batteries: Li–metal, Li–O₂, and Li–S,” *Energy and Environmental Science*, vol. 8, no. 7. Royal Society of Chemistry, pp. 1905–1922, 01-Jul-2015, doi: 10.1039/c5ee01215e.
- [155] E. Markevich *et al.*, “Reasons for capacity fading of LiCoPO₄ cathodes in LiPF₆ containing electrolyte solutions,” *Electrochem. commun.*, vol. 15, no. 1, pp. 22–25, Feb. 2012, doi: 10.1016/j.elecom.2011.11.014.
- [156] M. Stich, M. Göttliger, M. Kurniawan, U. Schmidt, and A. Bund, “Hydrolysis of LiPF₆ in Carbonate-Based Electrolytes for Lithium-Ion Batteries and in Aqueous Media,” *J. Phys. Chem. C*, vol. 122, no. 16, pp. 8836–8842, Apr. 2018, doi: 10.1021/acs.jpcc.8b02080.
- [157] R. Wagner *et al.*, “Impact of Selected LiPF₆ Hydrolysis Products on the High Voltage Stability of Lithium-Ion Battery Cells,” *ACS Appl. Mater. Interfaces*, vol. 8, no. 45, pp. 30871–30878, 2016, doi: 10.1021/acsami.6b09164.
- [158] J. Hou *et al.*, “Charge/discharge cycling of Li_{1+x} (Ni_{0.6} Co_{0.2} Mn_{0.2})_{1-x} O₂ primary particles performed in a liquid microcell for transmission electron microscopy studies,” *J. Phys. Energy*, vol. 2, no. 3, p. 034007, Jul. 2020, doi: 10.1088/2515-7655/ab979c.

- [159] R. Jung, M. Metzger, F. Maglia, C. Stinner, and H. A. Gasteiger, “Oxygen Release and Its Effect on the Cycling Stability of $\text{LiNi}_x\text{Mn}_y\text{Co}_z\text{O}_2$ (NMC) Cathode Materials for Li-Ion Batteries,” *J. Electrochem. Soc.*, vol. 164, no. 7, pp. A1361–A1377, 2017, doi: 10.1149/2.0021707jes.
- [160] E. Redondo-Iglesias, P. Venet, and S. Pelissier, “Global model for self-discharge and capacity fade in lithium-ion batteries based on the generalized eyring relationship,” *IEEE Trans. Veh. Technol.*, vol. 67, no. 1, pp. 104–113, 2018, doi: 10.1109/TVT.2017.2751218.
- [161] H. Liu *et al.*, “Capturing metastable structures during high-rate cycling of LiFePO_4 nanoparticle electrodes,” *Science* (80-.), vol. 344, no. 6191, 2014, doi: 10.1126/science.1252817.
- [162] B. Lung-Hao Hu, F. Y. Wu, C. Te Lin, A. N. Khlobystov, and L. J. Li, “Graphene-modified LiFePO_4 cathode for lithium ion battery beyond theoretical capacity,” *Nat. Commun.*, vol. 4, p. 1687, 2013, doi: 10.1038/ncomms2705.
- [163] F. Lin *et al.*, “Surface reconstruction and chemical evolution of stoichiometric layered cathode materials for lithium-ion batteries,” *Nat. Commun.*, vol. 5, 2014, doi: 10.1038/ncomms4529.
- [164] R. R. Unocic *et al.*, “Probing battery chemistry with liquid cell electron energy loss spectroscopy,” *Chem. Commun.*, vol. 51, no. 91, pp. 16377–16380, 2015, doi: 10.1039/c5cc07180a.
- [165] X. Lu, N. Zhang, M. Jahn, and W. Pfleging, “Improved Capacity Retention of SiO_2 -Coated $\text{LiNi}_{0.6}\text{Mn}_{0.2}\text{Co}_{0.2}\text{O}_2$ Cathode Material for Lithium-Ion Batteries,” *Appl. Sci.*, vol. 9, p. 3671, 2019.
- [166] P. C. Tsai *et al.*, “Single-particle measurements of electrochemical kinetics in NMC and NCA cathodes for Li-ion batteries,” *Energy Environ. Sci.*, vol. 11, no. 4, pp. 860–871, 2018, doi: 10.1039/c8ee00001h.
- [167] C. Zhan, T. Wu, J. Lu, and K. Amine, “Dissolution, migration, and deposition of transition metal ions in Li-ion batteries exemplified by Mn-based cathodes-A critical review,” *Energy Environ. Sci.*, vol. 11, no. 2, pp. 243–257, 2018, doi: 10.1039/c7ee03122j.

- [168] A. Barai, G. H. Chouchelamane, Y. Guo, A. McGordon, and P. Jennings, “A study on the impact of lithium-ion cell relaxation on electrochemical impedance spectroscopy,” *J. Power Sources*, vol. 280, pp. 74–80, 2015, doi: 10.1016/j.jpowsour.2015.01.097.
- [169] J. Wandt, A. T. S. Freiberg, A. Ogrodnik, and H. A. Gasteiger, “Singlet oxygen evolution from layered transition metal oxide cathode materials and its implications for lithium-ion batteries,” *Mater. Today*, vol. 21, no. 8, pp. 825–833, 2018, doi: 10.1016/j.mattod.2018.03.037.
- [170] Y. Wei *et al.*, “Kinetics Tuning of Li-Ion Diffusion in Layered Li(NixMnyCoz)O₂,” *J. Am. Chem. Soc.*, vol. 137, no. 26, pp. 8364–8367, 2015, doi: 10.1021/jacs.5b04040.
- [171] R. Jung *et al.*, “Nickel, Manganese, and Cobalt Dissolution from Ni-Rich NMC and Their Effects on NMC622-Graphite Cells,” *J. Electrochem. Soc.*, vol. 166, no. 2, pp. A378–A389, 2019, doi: 10.1149/2.1151902jes.
- [172] McKinsey&Company, “Lithium and cobalt – a tale of two commodities,” 2018.
- [173] S. Lee *et al.*, “Phase transitions in a LiMn₂O₄ nanowire battery observed by operando electron microscopy,” *ACS Nano*, vol. 9, no. 1, pp. 626–632, Jan. 2015, doi: 10.1021/nn505952k.
- [174] R. Dugas, J. D. Forero-Saboya, and A. Ponrouch, “Methods and Protocols for Reliable Electrochemical Testing in Post-Li Batteries (Na, K, Mg, and Ca),” *Chem. Mater.*, no. Cv, 2019, doi: 10.1021/acs.chemmater.9b02776.
- [175] E. M. Stuve, H. J. Gores, and H. Schweiger, “Overpotentials in Electrochemical Cells,” in *Encyclopedia of Applied Electrochemistry*, G. Kreysa, K. Ota, and R. F. Savinell, Eds. New York, NY: Springer New York, 2014, pp. 1445–1453.
- [176] B. Wu *et al.*, “Role of current density in the degradation of LiNi_{0.6}Co_{0.2}Mn_{0.2}O₂ cathode material,” *Electrochim. Acta*, vol. 298, pp. 609–615, Mar. 2019, doi: 10.1016/j.electacta.2018.12.127.
- [177] J. Hou, A. Freiberg, T. Shen, R. Girod, J. Gonthier, and S. Kim, “Charge/discharge cycling of Li_{1+x}(Ni_{0.6}Co_{0.2}Mn_{0.2})_{1-x}O₂ primary particles performed in a liquid microcell for

- transmission electron microscopy studies,” *J. Phys. Energy*, 2020.
- [178] P. Rozier and J. M. Tarascon, “Review—Li-Rich Layered Oxide Cathodes for Next-Generation Li-Ion Batteries: Chances and Challenges,” *J. Electrochem. Soc.*, vol. 162, no. 14, pp. A2490–A2499, 2015, doi: 10.1149/2.0111514jes.
- [179] W. Liu *et al.*, “Nickel-Rich Layered Lithium Transition-Metal Oxide for High-Energy Lithium-Ion Batteries,” *Angew. Chemie - Int. Ed.*, vol. 54, no. 15, pp. 4440–4457, 2015, doi: 10.1002/anie.201409262.
- [180] S. Sharifi-Asl, J. Lu, K. Amine, and R. Shahbazian-Yassar, “Oxygen Release Degradation in Li-Ion Battery Cathode Materials: Mechanisms and Mitigating Approaches,” *Adv. Energy Mater.*, vol. 9, no. 22, pp. 1–19, 2019, doi: 10.1002/aenm.201900551.
- [181] F. Yang, D. Wang, Y. Zhao, K. L. Tsui, and S. J. Bae, “A study of the relationship between coulombic efficiency and capacity degradation of commercial lithium-ion batteries,” *Energy*, vol. 145, pp. 486–495, Feb. 2018, doi: 10.1016/j.energy.2017.12.144.
- [182] J. Xiao *et al.*, “Understanding and applying coulombic efficiency in lithium metal batteries,” *Nat. Energy*, vol. 5, no. 8, pp. 561–568, Aug. 2020, doi: 10.1038/s41560-020-0648-z.
- [183] C. Y. Li *et al.*, “Surface Changes of $\text{LiNi}_x\text{Mn}_y\text{Co}_{1-x-y}\text{O}_2$ in Li-Ion Batteries Using in Situ Surface-Enhanced Raman Spectroscopy,” *J. Phys. Chem. C*, vol. 124, no. 7, pp. 4024–4031, 2020, doi: 10.1021/acs.jpcc.9b11677.
- [184] Y. Yu *et al.*, “Coupled LiPF_6 Decomposition and Carbonate Dehydrogenation Enhanced by Highly Covalent Metal Oxides in High-Energy Li-Ion Batteries,” *J. Phys. Chem. C*, vol. 122, no. 48, pp. 27368–27382, 2018, doi: 10.1021/acs.jpcc.8b07848.
- [185] A. M. Tripathi, W. N. Su, and B. J. Hwang, “In situ analytical techniques for battery interface analysis,” *Chem. Soc. Rev.*, vol. 47, no. 3, pp. 736–751, 2018, doi: 10.1039/c7cs00180k.

Curriculum vitae

Jing Hou

École polytechnique fédérale de Lausanne, MXD 220 (Bâtiment MXD) Station 12, Lausanne, 1015, Switzerland

+41 78 666 79 21, jing.hou@epfl.ch

EDUCATION

Aug 2013 — Jun 2016	Ph.D in Material Science and Engineering École polytechnique fédérale de Lausanne PhD thesis: Towards reproducible lithium-ion battery cycling using liquid-phase transmission electron microscopy.	Switzerland
Aug 2013 — Jun 2016	MSc in Material Science and Engineering École polytechnique fédérale de Lausanne Master thesis: Self-assembly behavior of grafted Au nanoparticles with different mixed ligand: synthesis and characterization of self-assembled Janus nanoparticles. Minor in Energy.	Switzerland
Sep 2008 — Jun 2012	BSc in Material Science and Engineering Tianjin University of Technology	China

RESEARCH EXPERIENCE

Oct 2016 — Present	Doctoral assistant on <i>in situ</i> liquid cell TEM study on Ni-rich NCM degradation, EPFL-INE The project aims at NCM degradation evaluation by correlating the electrochemical performance with its structural and elemental evolution during cycling using <i>in situ</i> transmission electron microscope based on microfluidics cell setup with liquid electrolyte. <ul style="list-style-type: none">▪ Material processing▪ Electrochemical chip and experimental condition optimization▪ Potentiostat and electron microscope operation▪ Electrochemical and microscopy results analysis	Switzerland
May 2018 — Sep 2018	Research stay, Technische Universität München 4 months exchange in the Chair of Technical Electrochemistry at TUM for the NCM study by bulk cell testing.	Germany
Jan 2016 — Sep 2016	Internship on morphology evolution analysis of ligand exchange reactions on gold nanoparticle, EPFL-SUNMIL The project focused on tracking the morphology evolution of the ligand shell on gold nanoparticles during the exchange reactions by using Matrix-assisted laser desorption/ionization Time-of-Flight (MALDI-TOF).	Switzerland

Jan 2015 — Jul 2015	Internship for the development of contact materials for power switching devices, ABB	Switzerland
	The project aimed at the development of processing routes for metal matrix composites based on powder metallurgy methods. I investigated the relevant relationships between process parameters, microstructures, and materials properties.	
Mar 2011 — Jan 2012	Research assistant, Zhejiang University	China
	The work focused on improving toluene decomposition efficiency without introducing secondary pollution by combining Mn-based catalyst with two-stage dielectric barrier discharge (DBD) non-thermal plasma (NTP) catalyst reactor	

SKILLS

Material evaluation: TGA/DSC/MALDI-TOF/NMR/UV-vis/DLS/SAXS

Electrochemical test and analysis: CV/GCD/EIS

Electron microscopy: liquid cell TEM/SEM/STEM-EDS

SCHOLARSHIPS AND REWARDS

Doctoral exchange grant from Zeno Karl Schindler (ZKS) Foundation	2018
Outstanding Undergraduate Thesis Award	2012

PUBLICATIONS

- J. Hou, R. Girod, N. Nianias, T. Shen, J. Fan, V. Tileli, “Lithium-Gold Reference Electrode for Potential Stability during *in situ* Electron Microscopy Studies of Lithium-Ion Batteries”, *J. Electrochem. Soc.* **167** 110515 (2020)
- J. Hou, A. Freiberg, T. Shen, R. Girod, J. Gonthier, S. Kim, “Charge/Discharge Cycling of $\text{Li}_{1+x}(\text{Ni}_{0.6}\text{Co}_{0.2}\text{Mn}_{0.2})_1\text{-XO}_2$ Primary Particles Performed in a Liquid Microcell for Transmission Electron Microscopy Studies”, *J. Phys. Energy* **2** 034007 (2020)
- M. Wetjen, S. Solchenbach, D. Pritzl, J. Hou, V. Tileli, H. Gasteiger, “Morphological Changes of Silicon Nanoparticles and the Influence of Cutoff Potentials in Silicon-Graphite Electrodes”, *J. Electrochem. Soc.* **165** 1503–1514 (2018).
- Z. Luo, Y. Zhao, T. Darwish, Y. Wang, J. Hou, F. Stellacci. "Mass spectrometry and Monte Carlo method mapping of nanoparticle ligand shell morphology. " *Nat. Commun.* **9**, (2018) 4478
- Z. Luo, J. Hou, L. Menin, QK Ong, and F. Stellacci. "Evolution of the Ligand Shell Morphology during Ligand Exchange Reactions on Gold Nanoparticles." *Angew. Chemie - Int. Ed.* **56**, 13521–13525 (2017)

CONFERENCES AND PRESENTATIONS

2020	EMPA-Materials for Energy Conversion Seminar	Switzerland
	Presentation on transmission electron microscopy for battery research.	
2019	Microscopy Conference, Berlin	Germany
	Poster on "Lithiation of micro reference electrode for reproducible cycling of lithium-ion battery systems in liquid TEM".	